Advanced Protection Technologies for Power Grids with Power Electronic Converter-interfaced Sources

Yang, Zhe

DOI (link to publication from Publisher):
10.54337/aau539432470

Publication date:
2023

Document Version
Publisher's PDF, also known as Version of record

ADVANCED PROTECTION TECHNOLOGIES FOR POWER GRIDS WITH POWER ELECTRONIC CONVERTER-INTERFACED SOURCES

BY
ZHE YANG

DISSERTATION SUBMITTED 2023

AALBORG UNIVERSITY
DENMARK

ADVANCED PROTECTION TECHNOLOGIES FOR POWER GRIDS WITH POWER ELECTRONIC CONVERTER-INTERFACED SOURCES

by

Zhe Yang

AALBORG UNIVERSITY
DENMARK

Dissertation submitted

.

Dissertation submitted: 4, April, 2023

PhD supervisor: Prof. Zhe Chen,
Aalborg University

Assistant PhD supervisor: Prof. Claus Leth Bak,
Aalborg University

PhD committee: Associate Professor Zhenyu Yang (Chairman)
Aalborg University, Denmark

Associate Professor Nathaniel Taylor
KTH Royal Institute of Technology, Sweden

Associate Professor Erik Cornelis Wytze de Jong
Technical University of Eindhoven, The Netherlands

PhD Series: Faculty of Engineering and Science, Aalborg University

Department: AAU Energy

ISSN (online): 2446-1636
ISBN (online): 978-87-7573-721-5

Published by:
Aalborg University Press
Kroghstræde 3
DK – 9220 Aalborg Ø
Phone: +45 99407140
aauf@forlag.aau.dk
forlag.aau.dk

Printed in Denmark by Stibo Complete, 2023

CV

Zhe Yang was born in Chaoyang, Liaoning Province, China in 1994. He obtained his bachelor's degree in Electrical Power Engineering from Northeast Electric Power University, Jilin, China, in 2017, and a master's degree in Power Systems and Automation from North China Electric Power University, Beijing, China, in 2020. He is currently a Ph.D. student at AAU Energy, Aalborg University, Alborg, Denmark. His research interests are power system modeling, fault analysis, the control and protection technologies for renewable energy sources.

ENGLISH SUMMARY

Numerous renewable energy sources (RESs) have been coupled with the modern power grid for environmental protection, so the grid is gradually changing from synchronous generator (SGs) dominated to power electronics dominated. The RES power plant is an important way to utilize renewable energy, especially for wind-rich or solar-rich areas, and the generated electricity is often transmitted to a far end by sub-transmission or transmission lines. These transitions will bring new challenges for transmission network protection because of their very different fault signatures such as the limited current, frequency offset, and variable sequence impedance angles.

The transmission network mainly installs directional elements, distance relays, differential relays, and auto reclosers. The most commonly used in the transmission line are fault component-based directional elements including positive-sequence fault component-based directional elements, negative-sequence directional elements, and zero-sequence directional elements. Since the sequence equivalent impedance angles of converter-interfaced renewable energy sources (CIRESs) depend on the executed fault ride-through (FRT) strategy and the fault conditions, and they may present a capacitive feature in some cases, directional elements may fail to operate. To manage this problem, a novel fault coordinative control scheme has been developed to guarantee the compatibility of CIRESs with line directional elements while the current limiting condition of CIRESs is satisfied.

Distance relays on the RES side also face severe challenges due to the remote infeed for the line integrated with CIRESs. The remote infeed current can amplify the influence of fault resistance and make the apparent impedance out of the protected range. Inspired by this challenge, two new methods based on active control are advised. One is to design a novel fault control strategy to adjust the fundamental frequency current from CIRESs for CIRESs compatible with traditional distance relays. The other one is to inject a second harmonic from the inverter of CIRESs and detect the apparent harmonic impedance to determine inside or outside-of-zone faults.

Moreover, the regulated current angle of CIRESs may result in a big current angle disparity between two terminals of the line under the traditional FRT, which will result in the sensitivity decline and even misoperation of differential protection, so three schemes are suggested to manage this issue. For the first method, a novel fault control strategy is suggested to regulate the phase angle difference of less than 60°, so the operations of differential protection could be enhanced. The latter two methods are based on the protection algorithm design. A pilot protection scheme based on the comprehensive current magnitude ratio is developed because the fault current from CIRESs is far lower than that of the grid. In addition, the improved Euclidean distance is applied to evaluate the similarity of fault currents between two terminals to detect internal faults.

Finally, a control-based scheme is suggested to detect the fault nature to reduce the secondary impact due to auto reclosing. For this method, CIRESs are controlled to be a voltage source, and the fault property could be distinguished by detecting the overcurrent after the current circuit breaker on the RES terminal is reclosed. Due to the low injected current and the short injection time, the secondary impact is reduced a lot for permanent faults. The suggested method behaves well for different fault types and remote high-resistive faults.

In this thesis, the protection adaptive problems and the corresponding solutions are verified by offline simulation in PSCAD. In addition, the real-time digital simulator (RTDS)-based experiment testing is also done to validate the suggested protection schemes.

DANSK RESUME

Talrige vedvarende energikilder (RES'er) er blevet koblet sammen med moderne strømsystemer på grund af kravet om miljøbeskyttelse, så nettet er gradvist ved at ændre sig fra synkrongenerator (SG'er) domineret til effektelektronik domineret. RES-kraftværket er en vigtig måde at udnytte vedvarende energi på, især til vind- eller solrige områder, og den producerede elektricitet overføres ofte til den fjerne ende af subtransmissions- eller transmissionsledninger. Disse overgange vil bringe nye udfordringer for transmissionsnetværksbeskyttelse på grund af deres eksotiske fejlsignaturer, såsom den begrænsede strøm, frekvensforskydning og den variable sekvensimpedansvinkel.

Transmissionsnetværket installerer hovedsageligt retningselementer, afstandsrelæer, differentialrelæer og autogenlukkere. Den mest almindeligt anvendte i transmissionslinjen er fejlkomponentbaserede retningselementer, herunder retningselementer baseret på positiv sekvens fejlkomponenter, retningsbestemte elementer med negativ sekvens og retningselementer med nulsekvens. Da de sekvensækvivalente impedansvinkler for konverter-interfacede vedvarende energikilder (CIRES'er) afhænger af den udførte fejlkørselsstrategi (FRT) og fejlforholdene og kan udgøre en kapacitiv egenskab i nogle tilfælde, kan retningsbestemte elementer muligvis ikke fungere. For at klare dette problem er der udviklet en ny fejlkoordinativ kontrolstrategi for at gøre CIRES'er kompatible med retningsbestemte elementer, mens den nuværende begrænsende betingelse for CIRES'er er opfyldt.

Afstandsrelæer på RES-siden står også over for alvorlige udfordringer på grund af fjerntilførslen til transmissionslinjen med CIRES'er. Fjerntilførselsstrømmen vil forstærke virkningen af fejlmodstanden og få den tilsyneladende impedans ud af det beskyttede område. Inspireret af denne udfordring anbefales to nye metoder baseret på aktiv kontrol. Den ene er at designe en ny fejlstyringsstrategi for at justere grundfrekvensstrømmen fra CIRES'er til CIRES'er, der er kompatible med traditionelle afstandsrelæer. Den anden er at injicere en anden harmonisk fra CIRES'er og detektere den harmoniske impedans for at bestemme interne og eksterne fejl.

Derudover vil den kontrollerede strømvinkel for CIRES'er føre til en stor strømvinkelforskel mellem begge terminaler, hvilket vil resultere i følsomhedsfald og endda differensbeskyttelsesfejl, så der foreslås tre ordninger til at håndtere dette problem. For den første metode foreslås en ny fejlkoordinatkontrolmetode for at reducere fasevinkelforskellen med mindre end 90°, således at ydeevnen af differentialbeskyttelse kan forbedres. De to sidstnævnte metoder er baseret på designet af beskyttelsesalgoritmen. En omfattende strømamplitudeforhold baseret pilotbeskyttelse er blevet udviklet, da fejlstrømmen fra CIRES'er er langt mindre end

nettets. Desuden bruges den forbedrede euklidiske afstand til at evaluere ligheden mellem to terminaler af fejlstrøm for at detektere interne fejl.

Endelig foreslås en kontrolbaseret ordning for at opdage fejlens natur for at reducere den sekundære påvirkning som følge af automatisk genlukning. Til denne metode styres CIRES'er til at være en spændingskilde, og fejlegenskaben kan skelnes ved at detektere fejlstrømmen, efter at afbryderen på RES-siden er genlukket. På grund af den lave indsprøjtede strøm og den korte indsprøjtningstid reduceres den sekundære påvirkning meget. Den foreslåede metode opfører sig godt til forskellige fejltyper og fjerntliggende højresistive fejl.

I dette speciale verificeres de beskyttelsesadaptive problemer og de tilsvarende løsninger ved offline simulering i PSCAD. Derudover udføres det real-time digital simulator (RTDS)-baserede eksperiment også for at validere de foreslåede beskyttelsesordninger.

ACKNOWLEDGEMENTS

This thesis summarizes the findings from the Ph.D. thesis entitled 'Advanced Protection Technologies for Power Grids with Power Electronic Converter-interfaced Sources'. The Ph.D. project is supported by AAU Energy, Aalborg University, Denmark and the Chinese scholarship Council (CSC). Moreover, I was also partly funded by Otto Mønsteds Fond, Denmark during my study abroad. I would like to extend my genuine appreciation to all of the aforementioned organizations.

The Ph.D. project is finished under the supervision of Prof. Zhe Chen, Prof. Claus Leth Bak, and Assistant prof. Zhou Liu. Good thanks for providing me with a previous opportunity and a good scientific environment for my Ph.D. study. I also want to express my sincere gratitude to them for their excellent guidance, insightful suggestions, and kind help with my Ph.D. project. Meanwhile, many thanks to Prof. Marjan Popov from Delft University of Technology (TU Delft) for giving me the chance to study abroad at TU Delft for about three months and providing me with helpful advice for my scientific work. In addition, good gratitude goes to Prof. Marjan and Prof. Jose de Jesus Chavez from the National Technological Institute of Mexico to teach me how to do the hardware in the loop experiment.

In addition, I would like to convey my immense gratitude to all of my colleagues at Aalborg University. The three-year Ph.D. period becomes interesting and fulfilling due to your company, trust, and help. Many thanks to Qi Zhang for helping me establish the simulation model and the hardware experiment platform. I also want to thank my friends Wenlong Liao, Hongyi Wang, Xinxin Chen, Yaqi Li, Jia Guo, Siyu Jin, Zhaoxin Wang, Hanchi Zhang, Zhijie Ma, and Zhili Shen for their help in daily life, research work and wonderful time together in Aalborg.

At last, I would like to appreciate my family members, especially my parents. Since the pandemic persists for three years, I never return to my hometown during the whole Ph.D. period. I am thankful to my parents for their understanding, encouragement, and support, and these are the source of my energy to help me finish my Ph.D. project.

Zhe Yang

Aalborg University, March 4, 2023

TABLE OF CONTENTS

LIST OF ACRONYMS

AC	Alternating current
ANN	Artificial-neutral network
CIRESs	Converter-interfaced renewable energy sources
CTs	Current transformers
DC	Direct current
DCC	Decoupled current control
DSC	Decoupled sequence control
DFIGs	Doubly-fed induction generators
FMPE	Fast matrix pencil extraction
FRT	Fault ride through
FFT	Fast Fourier transform
PV	Photovoltaics
PCC	Point of common coupling
PLL	Phase-locked loop
PMSGs	Permanent magnet synchronous generators
RESs	Renewable energy sources
SGs	Synchronous generators
AG	Line-A ground fault
BC	Line-B-to-line-C fault
BCG	Line-B-to-line-C ground fault
ABCG	Three-phase ground fault

TABLE OF FIGURES

Part I
Report

CHAPTER 1. INTRODUCTION

1.1. BACKGROUND

To protect the environment and save fossil energy, more renewable energy sources (RESs) are expected to be integrated into the power grid [1], [2]. The Danish government has an ambitious plan that all the energy consumption from different sectors will be from RESs by 2050 [3]. China plans to achieve carbon neutrality by 2060 [4]. Profited from the technology progress and cost decline, converter-interfaced RESs (CIRESs) such as permanent magnet synchronous generators (PMSGs) based wind turbines and photovoltaics (PV) become an attractive type to utilize renewable energy, and they have occupied a large share of the installed capacity in recent years [5], [6]. For the areas rich in wind and solar energy, many CIRESs will constitute a large-scale power plant that is often integrated into the far grid by a high-voltage transmission line [7], as displayed in Figure 1-1. Modern grid codes demand CIRESs to ride through a fault, hence their fault behaviors differ dramatically from those of typical synchronous generators (SGs) like the limited fault current, the controlled phase angle, and the variable sequence impedance angles [8], [9]. These new signatures will threaten the proper operation of existing protective relays on the transmission line [10]–[12].

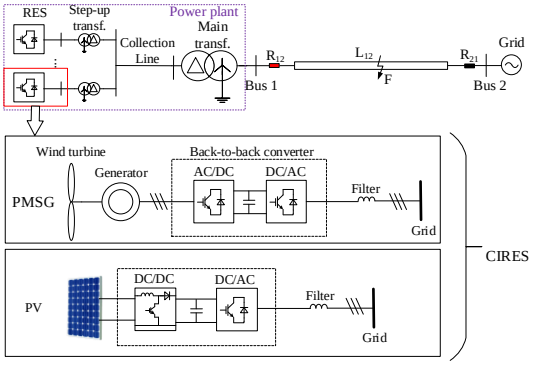

Figure 1-1 The transmission line with CIRESs.

The frequently used protective relays on the transmission line are directional elements, distance relays, differential protection, and auto recloser [13], [14]. Fault component-based directional relays are frequently used in the transmission network, and they detect the fault direction by measuring the impedance angle that reflects the impedance feature of the backside system [15]. For SGs, the sequence impedance angles should be close to 90°, so the measured impedance angle should tend toward -90° for forward faults due to the non-associated reference direction. Therefore, a positive direction is identified when the measured impedance angle is between -180°

to 0°considering a margin [16]. When CIRESs are connected, directional relays could exhibit minimal sensitivity or even fail to be triggered since the sequence impedance angles of CIRESs always vary with different fault scenarios [17]. Reference [18] analyzed the performance of directional elements when the Spanish grid code was performed. When the decoupled sequence control (DSC) is used, reference [19] tested the impedance angle feature under three control objectives: 1) suppressing the negative current, 2) suppressing active power oscillations, and 3) eliminating reactive power oscillations, and results showed that the impedance angle of CIRESs would be variable from -180° to 180°. Hardware-in-the-loop experimental testing was done to test the operation of negative-sequence directional relays in [20], and a comparable conclusion is reached. Moreover, a negative-sequence amplitude check is often executed for this directional element, so they may be not activated if the negative-sequence fault current is not provided by CIRESs [21]. Similarly, directional relays on the grid side can detect a forward fault for reverse faults, which will lead to the wrong operation of the current circuit breaker on the grid side and threaten the safe operation of the power system [22].

Distance protection is also a common protective relay in the transmission line because of the relatively fixed protection range [23]. The widely used distance relays have three types: 1) power-frequency distance relays, 2) fundamental-frequency fault component-based distance relays, and 3) time domain-based distance relays [24]. For power-frequency distance relays, the ratio of the measured voltage to the measured current is defined as the apparent impedance, and it is compared with the protection zone in the impedance plane to detect internal faults [25]. Its performance was considered independent of the source impedance behind the relay point in [24], but this result is obtained without considering the fault resistance. The apparent impedance expression for the line-to-line earth fault was derived in [26], and the analysis pointed out the remote infeed current will make the additional impedance become a large value, so the apparent impedance may be out of the protection range in the impedance plane. On this basis, the apparent impedance formula is analyzed for other fault types in [27], and the real-time digital simulator (RTDS) simulations were performed to confirm this conclusion. Fundamental frequency incremental-based distance relays detect an internal fault by comparing the operating voltage and the pre-fault voltage at the fault site, and its performance depends on the impedance feature of the backside source [24]. The variable sequence impedance angle of CIRESs will change the original voltage amplitude relationship, so this distance relay may fail to be activated [28]. Moreover, the sequence impedance amplitude of CIRESs is far larger than the line impedance, hence the protection sensitivity is very low even though the incremental impedance angle of CIRESs is close to 90° [15]. For time-domain distance relays, the least square approach is applied to evaluate the inductance parameter in the loop differential equation [24]. To only use the single terminal signals, the remote current is often substituted by the local positive-sequence superimposed current or zero-sequence current due to both similar current angles [29], [30]. However, the local positive-sequence superimposed current no longer has the

same phase angle as the remote current when CIRESs are connected, so the basic assumption for this time-domain distance relay is not satisfied. The local zero-sequence fault current can be still used, but it is only applicable to asymmetrical ground faults.

The transmission network usually installs pilot protective relays as the main protection because of their absolute selectivity and quick speed [31]. Pilot protection is classified as directional comparison pilot protection and current differential protection. Directional comparison pilot protection could be further divided into directional pilot protection and impedance pilot protection [32]. The performance of directional pilot protection relies on directional elements. If the directional element on the local side detects a positive directional fault, it will send a tripping signal to the remote side. When the remote directional element also detects a forward fault and receives the tripping signal from the other side, the current circuit breaker will be tripped [33]. The impedance pilot protection has a similar operation logic, but its core element is distance relays [34]. However, both operations will be affected adversely since directional elements and distance relays have adaptive problems when CIRESs are connected. The most frequently applied current differential protection is the proportional restraint differential protection [35]. For traditional power systems, the fault currents on both terminals have a similar phase for internal faults, so the operating current of this differential protection is far higher than the restraint current [36]. However, the current angle disparity between two terminals may be higher than 90° and even 120° in some cases, so the operating current would be smaller than the restraint current, which will lead to a poor sensitivity level or even failure if a large restraint coefficient is used [37].

In addition, the reclosing function is often installed to raise the resilience of the power grid, and three-phase reclosing is deployed for 110 kV (and below) lines [38]. Regarding the conventional reclosing scheme, the current circuit breaker on the remote side is reclosed firstly by detecting no voltage. After that, the circuit breaker on the local terminal will be reclosed by meeting the synchronization requirements [39]. Before the beginning of reclosing, a settled time delay is necessary to wait for the dielectric strength recovery. However, CIRESs might be disconnected from the power network since the active power from CIRESs is so difficult to match with the local load that the converter cannot work stably during this period [40], [41]. In this situation, there is no voltage on the CIRES side, so the condition for the voltage synchronization is not satisfied, which will result in the failure of reclosing. Moreover, if the circuit breaker on the grid side recloses with permanent faults, the electric devices will suffer a serious secondary impact [42]. Therefore, fault nature detection is significant to maintain the safety of the power system for three-phase reclosing.

In conclusion, directional elements, distance relays, differential protection, and auto recloser will be challenged when CIRESs are integrated. For these adaptive problems, the existing solutions will be summarized below.

1.1.1. DIRECTIONAL ELEMENTS

Some novel directional elements are put forward to detect the fault direction for the CIRES integration line. The sequence impedance amplitude of CIRESs is far larger than the impedance sum of the line and the connected grid, so a new directional relay relying on the impedance amplitude feature was suggested [43]. This method is effective for different fault types, different voltage levels, and even microgrids. Similarly, the ratio of the negative-sequence current to the positive-sequence current was applied to identify the direction of the fault [44]. However, this method is only effective when the negative-sequence current is not injected from CIRESs. In the latest grid code called VDE-AR-N 4120, the negative-sequence Q-axis current reference is settled according to negative-sequence voltage change during and before a fault, but the negative-sequence D-axis current command value is set to 0. Under this circumstance, the negative-sequence impedance of CIRESs will be equal to 90° like SGs, so the negative-sequence directional elements can work correctly [45]. However, the positive-sequence impedance angle of CIRESs is not regulated for this grid code. Similarly, a new controller was designed considering the filter capacitor, and suitable impedance parameters were calculated to make CIRESs present an inductive negative-sequence impedance [46]. Furthermore, the positive-sequence fault loop was designed as a voltage source with a fixed impedance during a fault [21], but the positive-sequence incremental impedance angle is not modified close to 90° due to the fact that it relates to electrical quantities prior to a fault. Therefore, more work for active control should be done to ensure the compatibility of CIRESs with directional components.

Moreover, some schemes are not only suitable for CIRESs but also doubly-fed induction generators (DFIGs). The least square method was applied to evaluate the loop resistance, and the resistance sign was different for forward and reverse faults [11], [47]. Furthermore, the correlation coefficient between the calculated voltage sag and the detected voltage sag was utilized as an additional criterion to avoid the dead zone when a near-end fault arises [48]. However, the current waveform during the first cycle was easily distorted when the hard current limiter was used, so the time-domain relays will be influenced [49]. In addition, the high-frequency impedance for DFIGs and CIRESs was established in [19], and then a high-frequency variation-based directional element was advised. The traveling wave-based protection in [50], [51] was also effective for RESs, but these methods have a high requirement for the sampling frequency.

1.1.2. DISTANCE RELAYS

To enhance the operation of distance relays, researchers come up with many new protection schemes. They can be separated into two aspects. On the one hand, novel protection algorithms are designed to adapt to RES integration. A new apparent impedance formula was built to indicate the fault distance between the relay point and

the fault point, but this is only effective for ground faults because the zero-sequence current feature is used [52]. In addition, reference [12] improved the operation of the local distance relay by allowing the remote distance relays to operate first, but the controller of CIRESs may not work stably because of losing the voltage support from the grid. A distance protection method was put forth using high-frequency fault components, but the reasonable frequency range may be difficult to be discovered in some cases [28]. Authors in [53] pointed out that the time-domain distance relay can detect the fault distance accurately when the voltage and current data on both terminals are used, but this method needs a high sampling rate. In addition, traveling wave-based protection strategies are also effective to identify the fault distance including the single terminal information-based methods and two terminal information-based methods [54], [55]. However, it is still difficult to detect the initial wave accurately. In addition, some adaptive distance relays in [56], [57] adjusted the protection zone in the impedance plane to enhance the protection performance according to the detected system state, but most of them need remote communication.

Since CIRESs can achieve flexible control objectives, some scholars want to solve protection problems by developing new control strategies. The salient advantage of this method is that traditional protective relays can work well with no or few revisions, so a large amount of investment can be saved. In [58], CIRESs are required not to inject any fault current to avoid the impact of the RES integration. However, modern grid codes request that CIRESs must maintain the grid-connected state within a certain time. To enhance the operation of distance relays, the positive-sequence current angle of SGs is imitated in [59] by computing suitable current command values such that the additional impedance is a purely resistive element, thus the reactance component in the apparent impedance can indicate the distance of a fault. Similarly, the impedance characteristic of SGs was simulated using the virtual impedance method in [21], which caused the fault currents between both terminals to have comparable phase angles. However, for these two methods, the injected reactive current might not comply with the fault ride-through (FRT) rules. In addition, the resistive reach of distance relays must be enlarged to cover the amplified resistive component. The reactive current injection requirement was satisfied in [60], but some errors will be present between the apparent reactance and the line fault reactance for near-end faults. Moreover, for island microgrids, a further distance relay relying on the ninth harmonic was suggested in [61], but the effect of the line capacitance on long transmission lines cannot be disregarded because the chosen frequency is so high. Therefore, it is an important topic to measure the fault distance correctly with FRT requirements satisfied.

1.1.3. DIFFERENTIAL PROTECTION

Many novel pilot protection technologies are suggested to improve the operation of the original differential protection. In [62], the differential impedance was calculated by the differential voltage dividing into the differential current, and its magnitude was

very large for out-of-zone faults, but it was small for internal faults, so internal and external faults could be detected by setting a reasonable threshold value. In addition, the fault current from CIRESs is restraint with 1.2 to 1.5 times the nominal current in order to safeguard the power electronics, but the grid fault current can be ten times the nominal current, so the phase current magnitude comparison-based pilot protection was put forward in [63], [64], but it can only resist a small fault resistance for interphase faults. To improve this ability, the sequence current magnitude ratio was developed to construct a new pilot protection scheme, but the faulty phases cannot be identified effectively anymore [65].

In addition to pure protection algorithm design based on power frequency components, a time-domain differential protection scheme was suggested in [66]. The linear relationship should be satisfied between the differential current and the first derivation of the differential voltage for internal faults, so the correlation coefficient is used to measure this linear relationship, but this method can only withstand a small noise. Some researchers discovered that the fault current from RESs always had some differences from that of the grid, so current waveform similarity-based pilot protection methods were proposed. Pearson correlation coefficient and Cosine similarity in [36], [67], [68] are two effective mathematical algorithms to measure this feature, they were computed using 10 ms or 20 ms of current sampling data from two terminals, and they are close to -1 for external faults since the current waveforms are the opposite, but they will be far from -1 for internal fault because of the current disparity between both terminals. However, these two methods will not have a clear result when the CIRES power plant has a blackout due to 0/0 problem. To deal with this issue, Spearman's rank correlation coefficient-based pilot protection was proposed, but different rank calculation methods need to be adopted for different current amplitudes, so a complementary criterion was necessary [69]. Therefore, it is better if a unified criterion can be proposed. In addition, it is not reported that a fault control method is suggested to enhance the sensitivity of differential relays while FRT requirements are satisfied.

1.1.4. AUTO RECLOSER

To address this issue, many academics have created a variety of adaptive reclosing techniques, which can be grouped into four categories: arc feature-based techniques, terminal voltage-based techniques, shunt reactor-based techniques, and active control-based techniques. The current and voltage produced by the arc will have lots of high-frequency components. In order to determine the fault property, references [70]–[72] assessed the difference between the detected harmonic voltage amplitude and the calculated value using the least square method. Voltage's high-frequency energy was utilized in [73] to determine the fault nature. Similar to this, the voltage signal's total harmonic distortion factor was computed in [74]. The artificial-neutral network (ANN) was employed to identify the permanent fault using the frequency feature of the residual voltage [75], [76]. Additionally, the high-frequency components were

used to measure the arc resistance to find the transient fault [77]. Additionally, references [78], [79] noted that the arc resistance would also influence the power-frequency voltage, and this feature was utilized to constitute a new criterion. However, these techniques heavily rely on the arc model's correctness. For the second approach, a criterion based on the voltage amplitude feature for the single-phase reclosing after the arc is extinguished was established in [80]. The measured voltage will adhere to this criterion for transient faults since the voltage amplitude and its angle were predicted in [81]. However, due to the elimination of the mutual inductance between the non-faulty and faulty phases, these techniques are not suitable for three-phase reclosing.

Shunt reactors are frequently deployed on high-voltage transmission lines to make up for the line capacitance, and the stored energy can provide distinctive voltage and current characteristics for permanent and temporary faults. To determine the permanent fault, the integral value of the recovery voltage for the defective phase was computed in [82]. Along with the fundamental-frequency components, the resonant component in the measured voltage for transient faults was also found [83]. Accordingly, there was also a clear difference in the frequency spectrum of the shunt reactor current on the faulty phase for two fault properties [84], [85]. The notion of parameter recognition was brought into this subject in [86], [87], and for permanent faults, the computed reactance value differed from the actual value. In addition, the temporary fault model was established to compute the shunt reactor current for temporary faults, so the difference between the measured value and the computed value could be utilized to form a new detection method [14]. Additionally, the impedance angle measured at the relay point was also different for permanent and temporary faults [88]. However, the above schemes are established only when the shunt rector is installed to generate the special transient process, but it may not be deployed on the 110 kV transmission line. Some active control-based approaches have also been put forth in recent years because power electronics can achieve the flexible control goals. In medium distribution networks, the load capacitor and inductor values are computed using the transient component injected from inverter, and the measured values were different when different frequency components are used for permanent failures, but there might not be any local load for large-scale wind parks [89]. Furthermore, the DC capacitor discharging is utilized to inject a low fault current into the faulty line by controlling the switching state of the power electronics of STATCOM [38], but a second injection is necessary to identify the fault type. Consequently, more active control-based methods need to be studied.

1.2. RESEARCH MOTIVATION

1.2.1. RESEARCH QUESTIONS

As reported above, though many new protection principles are designed to adaptive to the CIRES integration, the application of these methods needs to update the

protection devices, and some methods even request a high sampling rate, so a substantial investment is required. Therefore, more advanced protection schemes should be proposed especially solutions based on active control. In this Ph.D. project, a series of control schemes are suggested to enhance the operations of directional elements, distance relays, and differential relays and detect the fault property for reclosing. The overall research goal is that the protective relays make the smallest possible changes (or no changes), and the correct operation of protection is achieved by designing reasonable control strategies for CIRESs. In addition, two new pilot protection methods are also mentioned.

To main grid security and protect power electronic devices, the following problems are studied:

- **Q1:** How to design a new control method for CIRESs to make fault component-based directional elements operate correctly?

- **Q2:** How to make distance relays work properly by designing novel fault control schemes while the FRT conditions can be achieved including the fault current restraint and the reactive current injection?

- **Q3:** How to reduce the resistive part contained in the apparent impedance for distance relays when active control-based methods are used?

- **Q4:** How to improve the sensitivity of differential protection by an active control-based method or other schemes?

- **Q5:** How to detect the fault property using the converter to avoid reclosing with a permanent fault?

1.2.1. RESEARCH OBJECTIVES

To deal with these problems, the objectives of the overall Ph.D. project are summarized as follows:

- **O1:** Design a control strategy to ensure the compatibility of converter-interfaced sources with line directional elements.
  To handle Q1, the suitable positive- and negative-sequence fault currents of converter-interfaced sources are calculated according to the measured impedance angle of fault component-based directional elements. After that, these sequence currents are generated by setting the corresponding current references. During this process, the fault current limiting is also considered to protect the grid-side converter.

- **O2:** Propose a new fault coordination control method to make distance relays work properly.
  To answer Q2, for different fault types, the apparent impedance expressions are analyzed to obtain the suitable fault current from CIRESs to make distance relays work properly. To generate this fault current, the corresponding current command values are calculated considering the fault current limiting and reactive current injection.

- **O3:** Develop a harmonic injection-based distance relay to reduce the resistive part in the apparent impedance.
  To address Q3, the second and fourth harmonics are injected into the power grid from the grid-side converter of CIRESs. Following that, the harmonic impedance is computed to reflect the fault distance because this harmonic current is not present on the grid side during the steady state. Therefore, the problem of the remote infeed can be solved.

- **O4:** Propose effective methods to enhance the sensitivity of differential protection by active control and new protection algorithm design.
  To answer Q4, by analyzing the current phase angles on both ends, the suitable current angle of CIRESs is obtained to adjust the angle difference on both terminals for the faulty phase less than 60°, so the operation of original differential protection is improved. Moreover, two new pilot protection methods based on the improved Euclidean distance and amplitude ratio are also proposed.

- **O5:** Design a fault nature identification method using the voltage control of the grid-side converter.
  To handle Q5, after three-phase circuit breaker trips, the line will not have any voltage and current signals. To determine the fault property, the grid-side converter is regulated as a three-phase voltage source, and the small voltage amplitude will produce a small fault current for a permanent fault after the circuit breaker on the CIRES side is reclosed. In this way, the fault nature can be detected while the big secondary impact can be avoided.

1.3. PROJECT LIMITATIONS

Several project limitations are still present, and they are illustrated as follows:

- **L1:** This Ph.D. project solves the protection problems by designing suitable control strategies, therefore, the strict reactive current requirement sometimes needs a tradeoff with the protection objectives.

- **L2:** In this project, the proposed method based on active control is only applicable to the RES power plant that is only composed of CIRESs.

However, a power plant may include both CIRESs and DFIGs, but the proposed method cannot work properly for this case.

- **L3:** The full hardware-in-the-loop experiment has not been completed. It will be future work to detect the protection performance thoroughly.

1.4. THESIS OUTLINE

The dissertation is composed of two parts: Report and Selected Publications. The report summarizes the outcomes of the Ph.D. project based on the publications made during the Ph.D. period, as shown in Figure 1-2 (Journals - J, Conferences - C). This Report includes six chapters, and the specific content is shown as follows:

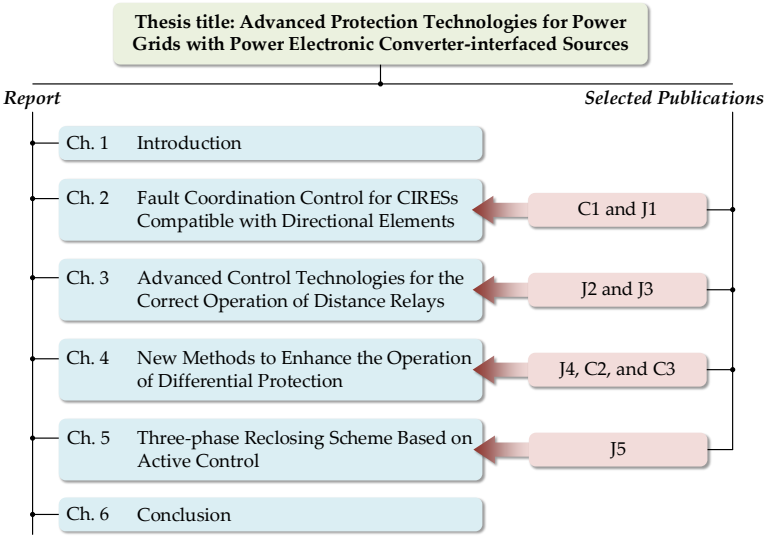

Figure 1-2 The chapters and the corresponding publications of this thesis.

- **Chapter 1 – Introduction**
  In this chapter, the background and the research hotspot are pointed out. After that, the research problems and research objectives are discussed for the outgoing transmission line connected with CIRESs. Finally, the project limitations are also mentioned.

- **Chapter 2 – Fault coordination control for CIRESs compatible with directional elements**
  In this chapter, a novel fault control scheme is suggested to adjust the phase angle of sequence superimposed impedances such that fault component-based directional elements could work properly. Meanwhile, the maximum permitted fault current is achieved to fully use the short-circuit capacity of

CIRESs. This method is verified in various fault cases like diverse fault types, diverse fault points, and diverse fault resistances. In addition, the RTDS experiment is also performed.

- **Chapter 3 – Advanced control technologies for the correct operation of distance relays**
  In this chapter, two control schemes are put forward to enhance the performance of distance relays. For the first method, the additional impedance will become purely resistive by generating the suitable fundamental frequency current, so the apparent reactance can reflect the fault distance. For the second method, a second harmonic is provided from CIRESs into the grid, and the measured harmonic impedance is effective to reduce the impact of the fault resistance. These two methods are verified by the PSCAD simulation and RTDS experiment.

- **Chapter 4 – New methods to enhance the operation of differential protection**
  In this chapter, three schemes are proposed to raise the sensitivity of differential relays. The first method is a control-based scheme that can make the phase angle difference between both terminals less than 60°. The other two methods are based on the new protection algorithm design. The improved Euclidean distance is used to evaluate the disparity between the current waveforms on both terminals. Moreover, the current amplitude ratio is utilized to construct another pilot protection method.

- **Chapter 5 – Three-phase reclosing scheme based on active control**
  In this chapter, an active control-based method is suggested to detect the fault property. After the circuit breakers on both sides trip at the function of protective relays, the grid-side inverter of CIRESs is regulated as a voltage source with a small amplitude. There will be a fault current for permanent faults when the circuit breaker on the CIRES side is reclosed. Therefore, the fault nature can be detected. PSCAD simulation and RTDS experiment jointly validate the effectiveness of this method.

- **Chapter 6 – Conclusion**
  In this chapter, the main contents and conclusions of this Ph.D. thesis could be summarized, and future perspectives are also given.

1.5. LIST OF PUBLICATION

The achievements during my Ph.D. period have been accepted or submitted in journals and conference proceedings including 5 journal papers (J1-J5) and 3 conference papers (C1-C3).

Journal papers:

J1. Z. Yang, Z. Liu, Q. Zhang, Z. Chen, J. d. J. Chavez and M. Popov, "A Control Method for Converter-interfaced Sources to Improve Operation of Directional Protection Elements," in *IEEE Trans. Power Del.*, accepted.

J2. Z. Yang, W. Liao, Q. Zhang, C. L. Bak and Z. Chen, "Fault Coordination Control for Converter-interfaced Sources Compatible with Distance Protection during Asymmetrical Faults," in *IEEE Trans. Ind. Electron.*, accepted.

J3. Z. Yang, Q. Zhang, W. Liao, C. L. Bak and Z. Chen, "Harmonic Injection Based Distance Protection for Line with Converter-interfaced Sources," in *IEEE Trans. Ind. Electron.*, accepted.

J4. Z. Yang, W. Liao, H. Wang, C. L. Bak and Z. Chen, "Improved Euclidean Distance Based Pilot Protection for Lines with Renewable Energy Sources," in *IEEE Trans. Ind. Informat.*, accepted.

J5. Z. Yang, W. Liao, C. L. Bak and Z. Chen, "Active control Based Three-phase Reclosing Scheme for Single Transmission Line with PMSGs," in *IEEE Trans. Ind. Electron.*, prepared.

Conference papers:

C1. Z. Yang, Q. Zhang, Z. Liu and Z. Chen, "Fault Current Calculation for Inverter-interfaced Power Sources Considering Saturation Element,"*2021 IEEE 4th International Electrical and Energy Conference (CIEEC)*, Wuhan, China, 2021.

C2. Z. Yang, W. Liao, C. L. Bak and Z. Chen, "Fault coordination control for converter-interfaced sources compatible with differential protection during asymmetrical faults," *The 5th International Conference on Electrical Engineering and Green Energy (CEEGE)*, Berlin, Germany, 2022.

C3. Z. Yang, W. Liao, C. L. Bak and Z. Chen, "Comprehensive current amplitude ratio based pilot protection for line with converter-interfaced sources," *2022 The 4th International Conference on Clean Energy and Electrical Systems (CEES 2022)*, Tokyo, Japan, 2022.

CHAPTER 2. FAULT COORDINATION CONTROL FOR CIRESS COMPATIBLE WITH DIRECTIONAL ELEMENTS

In this chapter, fault current features of CIRESs are analyzed during the transient state and steady state. After that, the operation of fault component-based directional elements is analyzed under traditional FRT strategies. Finally, a novel control approach is suggested to regulate the sequence superimposed impedance angle of CIRESs such that directional elements can behave properly.

2.1. THE FAULT CURRENT ANALYSIS

2.1.1. TRANSIENT CURRENT

Figure 2-1 depicts the conventional circuit topology of the grid-side inverter, and it can be utilized to establish the controller equations.

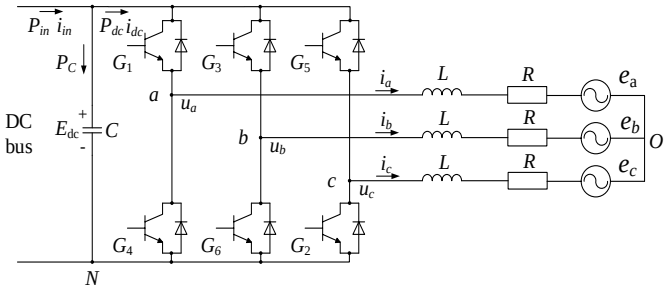

Figure 2-1 The circuit topology of the grid-side inverter. Source: C1 [90].

The circuit equation in the ABC frame can be simply listed with reference to the topology in Figure 2-1 [90]:

$$u_{\varphi} = e_{\varphi} + L\frac{d}{dt}i_{\varphi} + R \cdot i_{\varphi} \tag{2.1}$$

where subscript φ represents three phases, that is, a, b, and c.

The coordination transform can be used to derive the circuit equations in the DQ frame, as demonstrated in (2.2):

$$\begin{cases} (sL+R)i_{\mathrm{d}} = u_{\mathrm{d}} - e_{\mathrm{d}} + \omega_{\mathrm{PLL}} L i_{\mathrm{q}} \\ (sL+R)i_{\mathrm{q}} = u_{\mathrm{q}} - e_{\mathrm{q}} - \omega_{\mathrm{PLL}} L i_{\mathrm{d}} \end{cases} \tag{2.2}$$

where subscripts q and d denote the electrical component in the DQ coordinate system. ω_{PLL} is the angular velocity detected by PLL.

In the controller design, feedforward decoupling is typically employed to remove the coupling term in (2.2) [21]. The controller's mathematical model is displayed in (2.3):

$$\begin{cases} u_{\mathrm{d}} = \left(k_{ip} + \dfrac{k_{ii}}{s}\right)(i_{\mathrm{dref}} - i_{\mathrm{d}}) - \omega_0 L i_{\mathrm{q}} + e_{\mathrm{d}} \\ u_{\mathrm{q}} = \left(k_{ip} + \dfrac{k_{ii}}{s}\right)(i_{\mathrm{qref}} - i_{\mathrm{q}}) + \omega_0 L i_{\mathrm{d}} + e_{\mathrm{q}} \end{cases} \tag{2.3}$$

where i_{dref} and i_{qref} represent DQ-axis current references, k_{ip} and k_{ii} denote proportional constants and integral constants, and ω_0 denotes the synchronous angular velocity.

The coupling term can be removed by substituting (2.3) into (2.2) since ω_{PLL} is assumed to be equal to ω_0, yielding (2.4) [90]:

$$\begin{cases} (sL+R)i_{\mathrm{d}} = \left(k_{ip} + \dfrac{k_{ii}}{s}\right)(i_{\mathrm{dref}} - i_{\mathrm{d}}) \\ (sL+R)i_{\mathrm{q}} = \left(k_{ip} + \dfrac{k_{ii}}{s}\right)(i_{\mathrm{qref}} - i_{\mathrm{q}}) \end{cases} \tag{2.4}$$

Only the Q-axis control diagram is provided in Figure 2-2 because the D-axis is the same, and this control block diagram is easily generated through (2.4).

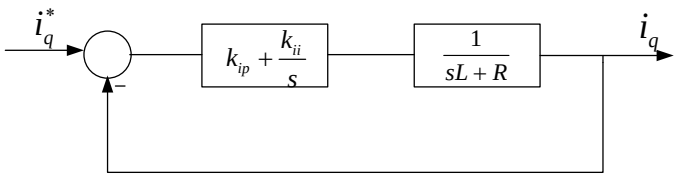

Figure 2-2 The control block diagram of the Q axis. Source: C1 [90].

It is a second-order system, but it could be converted to a first-order system by zero-pole cancellation to prevent transient current surges. At this point, (2.5) should be established:

$$\left(k_{ip}+\frac{k_{ii}}{s}\right)\frac{1}{sL+R}=\frac{\omega_{\mathrm{c}}}{s} \tag{2.5}$$

where ω_{c} is the first-order system's open loop crossover frequency.

The following conditions for proportional-integral (PI) parameters should be met by the corresponding coefficient method [91]:

$$\begin{cases} k_{ip}=\omega_{\mathrm{c}}L \\ k_{ii}=\omega_{\mathrm{c}}R \end{cases} \tag{2.6}$$

The closed-loop transfer function is expressed below when the control system's PI parameters are settled by equation (2.6):

$$G_0(s)=\frac{\omega_{\mathrm{c}}}{s+\omega_{\mathrm{c}}} \tag{2.7}$$

The Q-axis current reference change during a fault can be simplified as a step response. At this time, inverse Laplace transformation is applied to get the Q-axis current expression:

$$i_{\mathrm{qw}}(t)=i_{\mathrm{qref}}-\left(i_{\mathrm{qref}}-i_{\mathrm{q(0)}}\right)e^{-\omega_{\mathrm{c}}t} \tag{2.8}$$

where $i_{\mathrm{q(0)}}$ denotes the Q-axis current before a fault, which is typically equal to 0. In addition, the D-axis current expression is the same.

When the Chinese FRT strategy in (2.9) is performed (k is the current restraint value), and ω_{c} is set to 200π. i_{dref} is settled at 0.663 p.u., and i_{qref} is set to 1 p.u. when the voltage drops to 40%. Figure 2-3 displays the computed values and simulated values of the DQ fault currents [90].

$$\begin{cases} i_{\mathrm{qref}}=\min\left\{2\left(0.9-u_{\mathrm{1d}}\right),1\right\} \\ i_{\mathrm{dref}}=\sqrt{k^2-{i_{\mathrm{qref}}}^2} \end{cases} \tag{2.9}$$

As can be observed from Figure 2-3, the current on the DQ axis changes exponentially when new command values are applied during a fault, demonstrating that a second-order system is converted to a first-order system when suitable PI parameters are settled according to (2.6). In addition, the DQ-axis fault current computed by (2.8) completely matches the simulation results, which confirms the correctness of this suggested method.

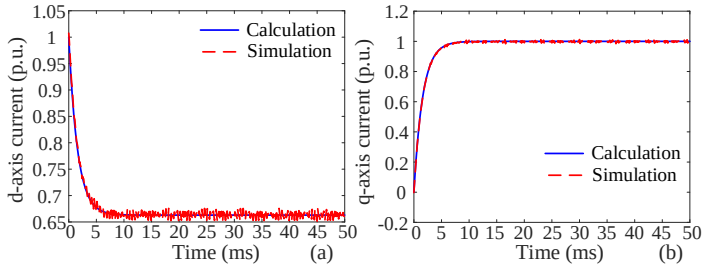

Figure 2-3 The computed and simulation values of DQ-axis fault currents. (a) D-axis, (b) Q-axis. Source: C1 [90].

2.1.2. STEADY-STATE CURRENT

Based on the controller's equation in (2.3), the controller topology can be drawn in Figure 2-4, which is also called decoupled current control (DCC) [92]. When the system operates in normal operation, the outer loop uses the constant DC voltage control. Once a fault happened, the outer loop is shunted down, and the current command values will be given directly regarding FRT strategies.

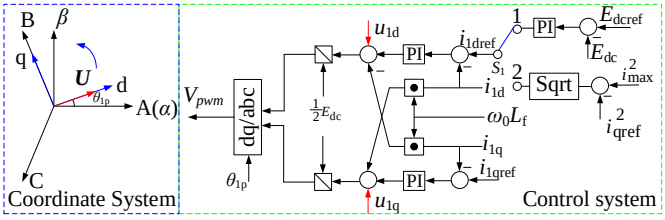

Figure 2-4 The DCC control.

After the positive- and negative-sequence electrical components are separated, a new decoupled sequence control (DSC) is developed to achieve more flexible control objectives [93], as shown in Figure 2-5.

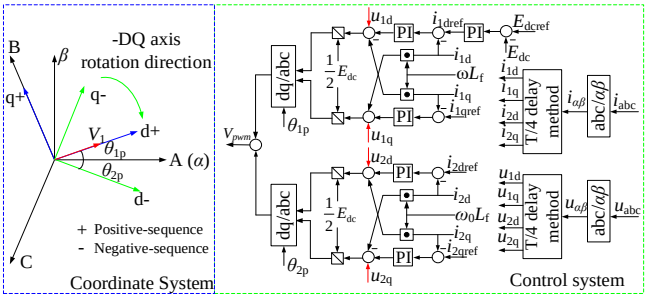

Figure 2-5 The DSC control.

When DCC is used, the fault current is only composed of the positive-sequence component, and its expression during the steady state is (2.10) [94], which can easily be obtained from the coordinate system in Figure 2-4.

$$i_{a1}=\sqrt{i_{1dref}^2+i_{1qref}^2}\sin\left(\omega_0 t+\theta_{1p}+\arctan\left(\frac{i_{1qref}}{i_{1dref}}\right)+90^\circ\right) \tag{2.10}$$

where i_{1dref} and i_{1qref} denote positive-sequence current command values in the DQ frame, θ_{1p} means the phase-locked angle, and t represents the fault time.

As displayed in (2.10), the magnitude and angle of this fault current are controlled by i_{1dref} and i_{1qref}. When the DSC is used, the positive-sequence fault current expression is the same, but the negative-sequence fault current is also generated in (2.11), and its amplitude and angle are controlled by i_{2dref} and i_{2qref} [95].

$$i_{a2}=\sqrt{i_{2dref}^2+i_{2qref}^2}\sin\left(\omega_0 t-\theta_{2p}-\arctan\left(\frac{i_{2qref}}{i_{2dref}}\right)+90^\circ\right) \tag{2.11}$$

where i_{2dref} and i_{2qref} denote negative-sequence current command values in the DQ frame, and θ_{2p} is the opposite number of θ_{1p}.

2.2. ADAPTIVE ANALYSIS

2.2.1. POSITIVE- AND NEGATIVE-SEQUENCE DIRECTIONAL ELEMENT

The performance of positive-sequence fault component-based directional elements (simplified as positive-sequence directional elements) and negative-sequence directional elements can be examined after the regulated characteristic of the CIRES fault current has been identified. By calculating the apparent impedances, Z_1 and Z_2, these two directional elements can determine the fault direction [15], [19]:

$$Z_1=\frac{\Delta U_1}{\Delta I_1}=\frac{U_1-U_b}{I_1-I_b} \tag{2.12}$$

$$Z_2=\frac{\Delta U_2}{\Delta I_2}=\frac{U_2}{I_2} \tag{2.13}$$

where Δ represents the incremental components before and during a fault, and U and I denote the voltage phasors and current phasors detected by the directional relay. Subscript b represents the pre-fault electrical components, and 1 and 2 mean the positive- and negative-sequence electrical quantities.

Since there is usually no negative current before a fault [60], ΔU_2 is considered equal to U_2. In the protection field, the current positive direction is from the busbar to the transmission line, so directional relays ought to identify an impedance angle that is near -90° for in-of-zone faults. [15]. Because of this, the criteria are typically described as (2.14) for forward faults:

$$-180^\circ < \angle Z_\phi < 0^\circ \tag{2.14}$$

where subscript ϕ stands for the sequence number, and $\angle$ means the impedance angle.

The sequence fault additional network is displayed in Figure 2-6. In this figure, Z_R denotes the sequence impedance of the CIRES power park, Z_S, Z_L, and Z_T respectively denote the impedances of the grid, the overhead line, and the main transformer, and R_g represents the fault resistance. Moreover, λ represents the ratio of the line impedance between the relay point and the fault location to the entire line impedance, and ΔU_f is the superimposed voltage source at the fault site. Additionally, the line capacitance is ignored since the 220 kV outgoing line is often shorter than 100 km [36].

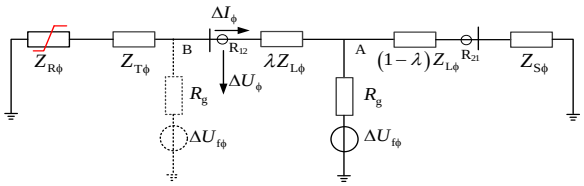

Figure 2-6 Sequence fault additional networks. Source: J1 [95].

The apparent impedance Z_ϕ measured at R_{12} can be expressed as (2.15) when a fault arises at A [95].

$$Z_\phi = -\left(Z_{R\phi} + Z_{T\phi}\right) \tag{2.15}$$

The angle of Z_ϕ is dependent on the angle of $Z_{R\phi}$ since $Z_{R\phi}$ is significantly greater than $Z_{T\phi}$. However, $Z_{R\phi}$ is always changed with current command values because I_1 and I_2 in (2.12) and (2.13) are determined by these references, but the sequence impedance angles of SGs are stable at about 90°. i_{1qref} is typically generated in response to voltage sags during a fault to enhance the transient voltage of the grid, and the left room is used to produce i_{1dref}. Additionally, i_{2dref} and i_{2qref} are typically set to 0 [96]. At this time, positive-sequence incremental-based directional elements may incorrectly determine the fault direction since these conventional FRT strategies do not take into account the impedance angle regulation of CIRESs.

Z_ϕ measured at R_{12} is expressed as (2.16) when the fault site is at B in Figure 2-6:

$$Z_{\phi} = Z_{L\phi} + Z_{S\phi} \tag{2.16}$$

Currently, directional elements can accurately identify a reverse direction because the angle of Z_{ϕ} is dependant on the impedance angle of the grid and the transmission line, which is close to 90°.

However, as the apparent impedance of positive- and negative-sequence directional elements at R_{21} is equal to $Z_{R\phi}+Z_{T\phi}+Z_{L\phi}$ for a reverse fault located at F5 (Figure 2-8), a positive direction fault may be reported, which will jeopardize the grid's security.

2.2.2. ZERO-SEQUENCE DIRECTIONAL ELEMENTS

The apparent impedance Z_0 is described similarly as [44]:

$$Z_0 = \frac{U_0}{I_0} \tag{2.17}$$

where subscript 0 stands for zero-sequence components during a fault.

Since the main transformer adopts the YND wiring, Z_0 is always equal to $-Z_{T0}$ for an asymmetrical earth fault at the line, and the equivalent impedance of CIRESs is not contained in the zero-sequence fault loop, the operations of zero-sequence directional elements are not undermined by CIRESs. However, zero-sequence directional elements are only applicable to unbalanced grounding faults, so the operation of positive- and negative-sequence directional elements must be improved to identify the direction of a fault under three-phase faults and line-to-line faults.

2.2.3. SIMULATION ANALYSIS

Directional elements are assessed when the FRT strategy in Denmark in Figure 2-7(a) is performed. For this strategy, i_{1qref} is calculated with reference to the voltage drop, and the left capacity is used to produce i_{1dref} [97]. In addition, i_{2dref} and i_{2qref} are settled at 0. In area A, CIRESs should operate in normal situations. They can maintain the grid-connected state for a certain time in area B, as illustrated in Figure 2-7(b). In addition, they can be disconnected from the main grid when they operate in area C.

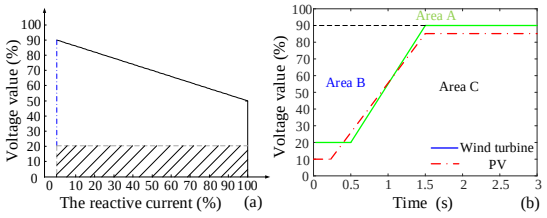

Figure 2-7 The Danish FRT strategy. (a) Reactive current, (b) the time-voltage curve.

The typical transmission line with 100 MW of the CIRES power park is built in PSCAD, as shown in Figure 2-8. Fault F1 is oriented at the backside of R_{12}, and fault locations F2, F3, and F4 are internal faults and at 0%, 50%, and 100% of the overhead line, respectively. Finally, F5 is at the output of the next-level line.

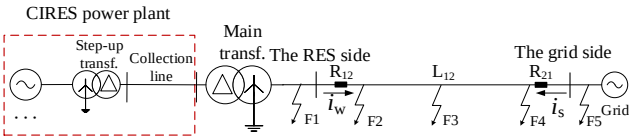

Figure 2-8 The topology of the simulation model. Source: J1 [95].

When a metallic phase-A grounding fault arises at F2, the associated measured quantities of directional elements are displayed in Figure 2-9.

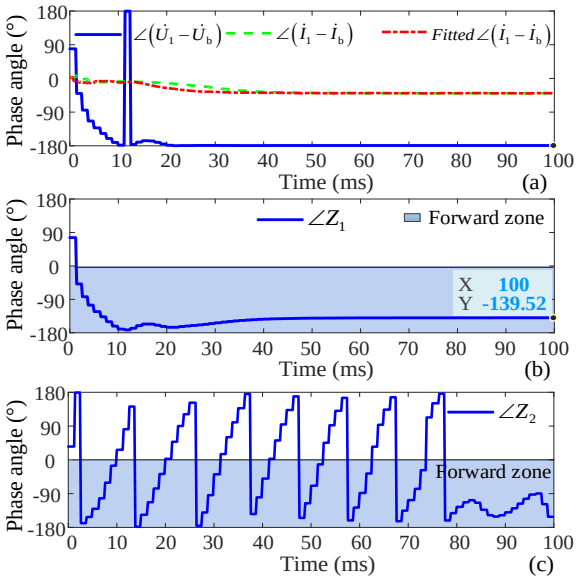

Figure 2-9 The associated phasors detected by directional elements under the Danish FRT. (a) Measured voltage and current, (b) ∠Z_1, (c) ∠Z_2. Source: J1 [95].

Figure 2-9(a) shows that the positive-sequence fault current is effectively regulated by positive-sequence current command values during the steady state. The disparity that occurs during the transient process arises from the inaccuracy of the phase-locked loop. In this case, positive-sequence directional elements in Figure 2-9(b) detect an impedance angle steady at -139.52°, which deviates significantly from -90° at 0.5 s. so this directional element will have a low sensitivity level. Moreover, according to (2.11), the negative-sequence current angle is uncertain when i_{2dref} and i_{2qref} are settled

to 0, resulting in incorrect direction identification. As a result, the angle of Z_2 in Figure 2-9(c) will fluctuate across a wide range. Overcurrent detection is a function that is incorporated into some commercial directional elements. In this sense, assuming that negative-sequence current is not output from CIRESs, negative-sequence directional elements are not triggered to identify the direction of the fault [22].

2.3. ACTIVE CONTROL-BASED SOLUTION

Appropriate current references are determined by taking into account the requirements of FRT and line protection to change sequence impedance angles of CIRESs in order to ensure directional relays behave well.

2.3.1. CURRENT REFERENCE CALCULATION

A. Positive-sequence current command values

To compute appropriate current command values for the proper operation of positive-sequence directional elements, the required positive-sequence current must be acquired by analyzing the associated protection criterion. For this aim, the measured phasors at the relay site are written as follows [95]:

$$\begin{cases} U_1 = |U_1| \angle \varphi_1 \\ U_b = |U_b| \angle \varphi_b \end{cases}, \begin{cases} I_1 = |I_1| \angle \alpha_1 \\ I_b = |I_b| \angle \alpha_b \end{cases} \tag{2.18}$$

where α is the current angle, and φ denotes the voltage angle.

After (2.18) is substituted into (2.12), the measured impedance Z_1 of directional elements can be expressed as:

$$Z_1 = \frac{|U_1|\cos\varphi_1 - |U_b|\cos\varphi_b + \mathrm{j}\left(|U_1|\sin\varphi_1 - |U_b|\sin\varphi_b\right)}{|I_1|\cos\alpha_1 - |I_b|\cos\alpha_b + \mathrm{j}\left(|I_1|\sin\alpha_1 - |I_b|\sin\alpha_b\right)} \tag{2.19}$$

Take the magnitude and the angle of Z_1, and they are expressed as:

$$|Z_1| = \frac{\sqrt{\left(|U_1|\cos\varphi_1 - |U_b|\cos\varphi_b\right)^2 + \left(|U_1|\sin\varphi_1 - |U_b|\sin\varphi_b\right)^2}}{\sqrt{\left(|I_1|\cos\alpha_1 - |I_b|\cos\alpha_b\right)^2 + \left(|I_1|\sin\alpha_1 - |I_b|\sin\alpha_b\right)^2}} = \sqrt{\frac{A_1^2 + B_1^2}{A_2^2 + B_2^2}} \tag{2.20}$$

$$\angle Z_1 = \arctan\frac{B_1}{A_1} - \arctan\frac{B_2}{A_2} \tag{2.21}$$

where $|\cdot|$ represents a phasor's magnitude, and arctan $(\cdot)$ is designated as the angle between -180° and 180°. Moreover, $A_1=|U_1|\cos\varphi_1-|U_b|\cos\varphi_b$, $B_1=|U_1|\sin\varphi_1-|U_b|\sin\varphi_b$, $A_2=|I_1|\cos\alpha_1-|I_b|\cos\alpha_b$, and $B_2=|I_1|\sin\alpha_1-|I_b|\sin\alpha_b$.

To guarantee the directional element operates properly, set (2.21) equal to -90° so that the necessary phase angle of I_1 is calculated:

$$\alpha_1=\arcsin\frac{F}{\sqrt{1+\left(\tan E\right)^2}}+E \tag{2.22}$$

where E and F satisfy the following relationship:

$$E=\arctan\frac{B_1}{A_1}+90^\circ \tag{2.23}$$

$$F=\frac{|I_b|}{|I_1|}\sin\alpha_b-\frac{|I_b|}{|I_1|}\tan E\cdot\cos\alpha_b \tag{2.24}$$

For the amplitude of I_1, it is calculated in Section 2.3.2 when the current limiting of the grid-side inverter is considered. To generate the required angle in (2.22), the first condition for i_{1dref} and i_{1qref} must be satisfied:

$$k_1=\frac{i_{1qref}}{i_{1dref}}=\tan\left(\alpha_1-90^\circ-\theta_{1p}\right) \tag{2.25}$$

Additionally, the peak value of the positive-sequence current, I_{1m}, is expressed as $\sqrt{i_{1dref}^2+i_{1qref}^2}$ in (2.10) as the second constraint, so two suitable current command values can be obtained:

$$\begin{cases} i_{1dref}=\sqrt{\dfrac{1}{1+k_1^2}}I_{1m} \\ i_{1qref}=k_1 i_{1dref} \end{cases} \tag{2.26}$$

Directional elements can work properly for forward faults when current references are settled by (2.26) since the measured impedance angle is adjusted to -90°.

B. Negative-sequence current command values

By computing appropriate negative-sequence current command parameters, the impedance angle measured by negative-sequence directional relays could be also

regulated to -90°. Firstly, negative-sequence current and voltage phasors detected at the relay site are written as [95]:

$$\begin{cases} I_2 = |I_2| \angle \alpha_2 \\ U_2 = |U_2| \angle \varphi_2 \end{cases} \tag{2.27}$$

When (2.27) is substituted into (2.13), the measured impedance Z_2 yields:

$$Z_2 = \frac{|U_2|}{|I_2|} \angle (\varphi_2 - \alpha_2) \tag{2.28}$$

It can be shown in (2.28) that the measured impedance angle only depends on the angle difference between the negative-sequence voltage and the negative-sequence current, so the necessary negative-current angle could be easily computed by taking the impedance angle in (2.28) equal to -90°:

$$\alpha_2 = \varphi_2 + 90^\circ \tag{2.29}$$

To generate this phase angle, the first condition must be satisfied with reference to (2.11):

$$k_2 = \frac{i_{2\text{qref}}}{i_{2\text{dref}}} = -\tan(\varphi_2 + \theta_{2\text{p}}) \tag{2.30}$$

Additionally, the peak value of the negative-sequence fault current, $I_{2\text{m}}$, is $\sqrt{i_{2\text{dref}}^2 + i_{2\text{qref}}^2}$ according to (2.11), so two suitable current command values are computed as follows:

$$\begin{cases} i_{2\text{dref}} = \sqrt{\dfrac{1}{1+k_2^2}} I_{2\text{m}} \\ i_{2\text{qref}} = k_2 i_{2\text{dref}} \end{cases} \tag{2.31}$$

2.3.2. INITIAL VALUES OF SEQUENCE CURRENTS

To calculate current command values in (2.26) and (2.31), appropriate initial values for $I_{1\text{m}}$ and $I_{2\text{m}}$ need to be given considering the restrained short-circuit capacity of CIRESs. The maximum fault current, abbreviated as γI_{N} (γ denotes the overcurrent multiple, and I_{N} denotes the nominal current), is typically restricted to 1.2 to 1.5 times the nominal current [94], [98]. If $|I_2|$ is equal to β times $|I_1|$, the initial values can be calculated by (2.32) [95]:

$$|I_1|+|I_2|=(1+\beta)|I_1|=\gamma I_N \tag{2.32}$$

At this time, three-phase currents must be lower than γI_N since $|I_1+I_2|$ must be less than $|I_1|+|I_2|$ due to the sequence current angles. To fully utilize the short-circuit capacity of the inverter, the technique to maximize the fault current is reported in Section 2.3.3.

Additionally, the following will be explored regarding the range of β. Numerous protection problems will arise if β is higher than 1 since the phase relationship will be reversed from ABC to ACB. Meanwhile, $|I_2|$ must have a certain amplitude to trigger negative-sequence directional elements. Considering these two factors, β should range from 0.2 to 1 [21].

2.3.3. MAXIMIZE THE FAULT CURRENT

An effective way to find the maximum permitted fault currents is covered in this part. First, three-phase fault currents are calculated using the Cosine theorem [95]:

$$\begin{cases} |I_a|=\sqrt{|I_1|^2+|I_2|^2+2|I_1||I_2|\cos\Delta\alpha} \\ |I_b|=\sqrt{|I_1|^2+|I_2|^2-2|I_1||I_2|\cos(\Delta\alpha-60^\circ)} \\ |I_c|=\sqrt{|I_1|^2+|I_2|^2-2|I_1||I_2|\cos(\Delta\alpha+60^\circ)} \end{cases} \tag{2.33}$$

where $\Delta\alpha$ denotes the angular disparity between positive-sequence and negative-sequence fault currents, and it fulfills the equation below:

$$\Delta\alpha=\left|\arctan\frac{i_{1qref}}{i_{1dref}}+\arctan\frac{i_{2qref}}{i_{2dref}}\right| \tag{2.34}$$

The following iterative method is used to acquire maximum current command values:

1) The associated peak values I_{1m} and I_{2m} can be derived when the initial values of $|I_1|$ and $|I_2|$ are defined by (2.32).

2) After sequence current command values have been computed by (2.26) and (2.31), three-phase fault currents are estimated by (2.33) and (2.34).

3) If the maximum value among three-phase currents is smaller than γI_N, $|I_1|$ will be updated by the original value plus λ in (2.35). Otherwise, $|I_1|$ will be decreased by λ. Repeat steps 2) and 3) until λ converges to the acceptable scope, ε.

$$\lambda = \left| \max\left\{ |I_a|, |I_b|, |I_c| \right\} - \gamma I_N \right| \tag{2.35}$$

By using this technique online, the output fault current can be increased to its maximum value when current references after iteration are given to the current control loop. The complete control diagram is depicted in Figure 2-10.

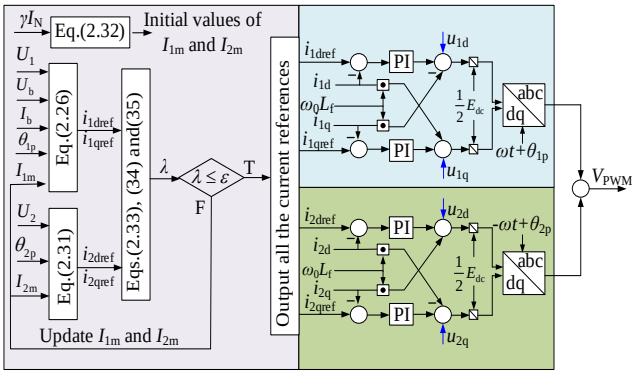

Figure 2-10 The overall control diagram. Source: J1 [95].

The corresponding protection flowchart is drawn in Figure 2-11. After a fault is identified, the negative-sequence current and voltage are checked whether they surpass their respective starting values. I_{2set} and U_{2set} are respectively settled to 10% of the nominal current and 2% of the nominal voltage [22], [96]. Finally, the measured impedance angle from directional elements is computed. If the impedance angle ranges from -180° to 0°, a positive direction is reported. Otherwise, a reverse direction can be determined.

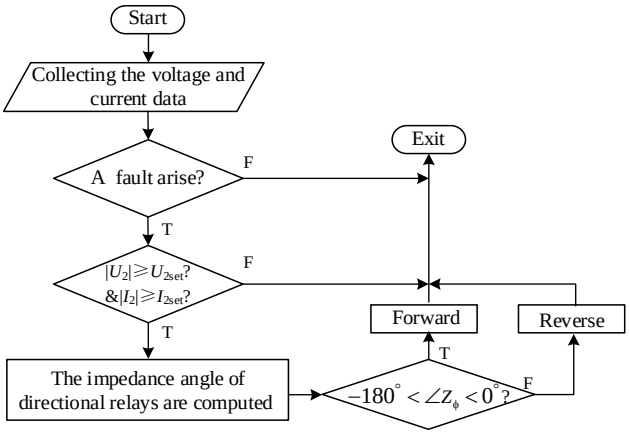

Figure 2-11 The protection flowchart of directional elements. Source: J1 [95].

2.3.4. SIMULATION ANALYSIS

A. The effectiveness of the suggested method

The associated measurements of directional elements at R_{12} are shown in Figure 2-12 after the suggested control scheme is used (the fault scenario is the same as that in Figure 2-9). In this case, γ is set to 1.5, and β is taken as 0.3.

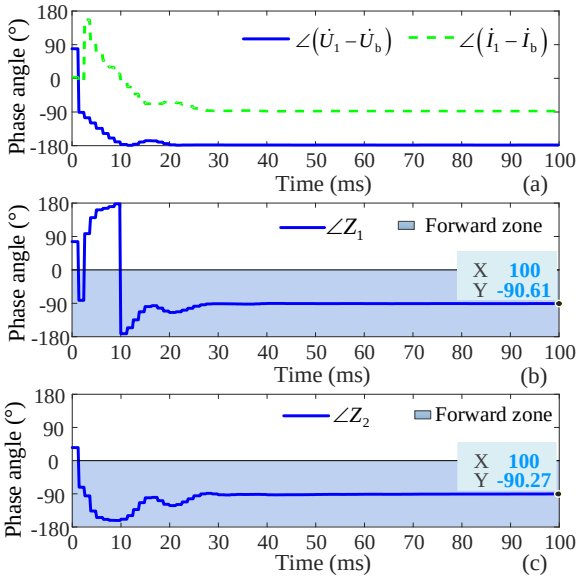

Figure 2-12 The associated phasors detected by directional elements for the proposed control scheme. (a) Angle of the incremental voltage and current, (b) $\angle Z_1$, (c) $\angle Z_2$. Source: J1 [95].

As seen in Figure 2-12(a), the measured positive-sequence current angle of positive-sequence directional elements will be regulated with reference to the detected voltage angle (both trends are similar). In this situation, the impedance angle computed by the positive-sequence incremental-based directional elements is -90.61° at 100 ms in Figure 2-12(b), which indicates that the sensitivity of this directional relay is substantially improved. However, the impedance angle fluctuates significantly during the first 20 ms because the controller takes one or two cycles to achieve a steady state. In order to avoid this short transient impact, a minor time delay of 40 ms is introduced to this protective relay, though this will slow down its operating speed. Moreover, negative-sequence directional elements also work nicely in Figure 2-12(c). In this case, the values of i_{1dref} and i_{1qref} are 1.0024 and -0.6800, respectively, demonstrating the ability of CIRESs to provide reactive power for the power grid to enhance the transient voltage. Figure 2-13 displays the positive-sequence voltage measured at the

point of common coupling (PCC), the output power from CIRESs, and three-phase currents detected at the inverter output.

In Figure 2-13 (a), the positive-sequence voltage detected at PCC falls to 70.5% of the nominal voltage. According to Figure 2-7, CIRESs operate in area B, so they can maintain the grid-connected state within a specific time. Additionally, in Figure 2-13(b), the reactive power is increased to 0.62 p.u., which indicates that the reactive power is injected to increase the grid voltage. After two or three iterations, the suggested iterative method converges, and the phase-A current approaches the permissible maximum value (1.5 p.u.), as displayed in Figure 2-13(c).

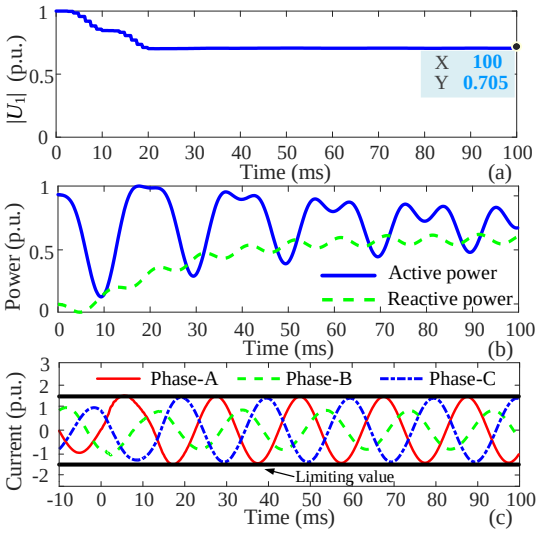

Figure 2-13 The associated measurement for the suggested method. (a) Positive-sequence voltage at PCC, (b) power detected at the inverter output, (c) currents at the inverter output. Source: J1 [95].

B. The effectiveness of the suggested method

The suggested approach is assessed for different fault kinds and fault points, and simulation results for metallic faults are displayed in Table 2-1. The values in the table were all collected at 100 ms. G stands for phase to ground, whereas the letters A, B, and C stand for faulty phases.

Table 2-1 demonstrates that, regardless of fault positions and fault types, the impedance angle computed by directional relays is near -90° for positive direction faults, thus the sensitivity has been enhanced. This demonstrates that the sequence incremental impedance angles of CIRESs are effectively regulated by this innovative control strategy. The impedance angle estimated at R_{12} for reverse faults at F1 shows

the impedance characteristic of the outgoing line and the connected grid, so directional elements can report a reverse fault correctly. The generated frequency from the PLL maintains the power frequency during three-phase bolted faults, so the suggested method can still work since the fault current from CIRES keeps the fundamental frequency. However, the fault current may be distorted for some grid-following inverters due to the instability of the inverter. The suggested control scheme cannot function effectively in this situation. Additionally, for reverse faults at F5, the impedance angles observed by direction relays at R_{21} are close to 90°, so a reverse fault can be detected. In addition, other simulation cases can be found in J1.

TABLE 2-1 VARIOUS FAULT LOCATIONS AND FAULT KINDS. *Source: J1 [95].*

Relay	Fault points	Fault types	$\angle Z_1$	$\angle Z_2$
R_{12}	F1	BG	79.19	79.20
		AB	79.27	79.27
		BCG	79.21	79.46
		ABCG	79.28	/
R_{12}	F2	BG	-90.69	-88.87
		AB	-90.65	-89.49
		BCG	-90.77	-88.90
		ABCG	-90.66	/
R_{12}	F3	BG	-90.79	-88.61
		AB	-90.66	-89.50
		BCG	-90.78	-88.75
		ABCG	-90.92	/
R_{12}	F4	BG	-90.98	-89.88
		AB	-90.68	-90.08
		BCG	-91.06	-89.33
		ABCG	-90.92	/
R_{21}	F5	BG	88.55	89.74
		AB	88.92	89.13
		BCG	88.88	89.97
		ABCG	88.72	/

2.3.5. RTDS VERIFICATION

As shown in Figure 2-14, real-time simulations are performed in RTDS to further verify the suggested strategy. A PC workstation, an internet router, and two Racks make up the RTDS platform. The Rack, which consists of many RTDS cards and an

internet switch, is the fundamental component of the RTDS. Among them, GPC cards are responsible for operating the complied model that is established in RSCAD. In addition, a GTWIF card with an internet switch and a router constitutes a local area network, which can be used to return the generated data from GPC cards to the PC workstation. Finally, MATLAB programming is used to confirm the effectiveness of the protection.

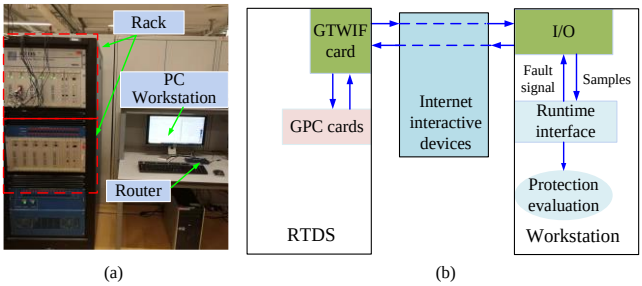

Figure 2-14 The RTDS platform. (a) Actual hardware devices, (b) hardware connection way. Source: J1 [95].

Figure 2-15 shows three-phase fault currents of CIRESs for an AG fault and the computed impedance angle at R_{12} for two faults at F4 (The fault types are an AG fault with 100 Ω of R_g and a BC fault with 20 Ω of R_g).

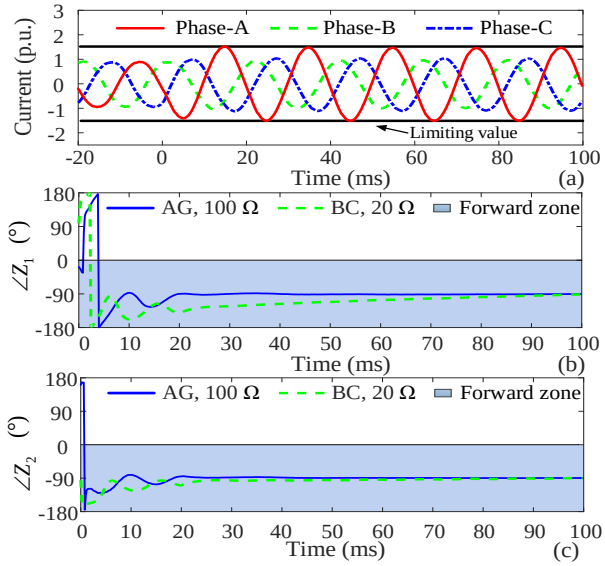

Figure 2-15 The CIRES fault currents and the operations of directional elements. (a) Three-phase fault currents for AG faults, (b) ∠Z_1, (c) ∠Z_2. Source: J1 [95].

The maximum fault current among the three phases is equal to the current limiting value, as shown in Figure 2-15(a), so the short-circuit capacity is fully utilized. In this situation, positive-sequence incremental-based directional relays can now behave properly since the detected impedance angle in Figure 2-15(b) is -90.65° for this AG fault and -91.36° for this BC fault. Additionally, for these two situations, the impedance angles observed by negative-sequence directional relays also get close to -90° in Figure 2-15(c). These results confirm that the operations of directional elements could be enhanced by using this novel control mechanism again.

2.4. SUMMARY

This chapter derives the fault current expression during the transient state and the steady state. At the fault inception, the change of current command values can be simplified as a step function, so the step response of the control system can be derived to obtain the transient fault current expression in the DQ frame. When the fault current comes into the steady state, the actual DQ-axis current will be equal to both respective command values, and the phase-A positive-sequence current expression during the steady state is given by the coordinate transform.

Based on this, the operation of directional elements is analyzed. The study shows that the controlled sequence current of CIRESs under typical FRT strategies will affect the correct direction identification of fault component-based directional elements. Therefore, a new fault control method is suggested to regulate the sequence superimposed impedance angle of CIRESs so that conventional directional elements can behave well. Meanwhile, the short-circuit capacity of CIRESs is fully utilized by an iteration method. PSCAD simulation and RTDS experiment confirm the suggested method.

Related Publications

C1. Z. Yang, Q. Zhang, Z. Liu, and Z. Chen, "Fault Current Calculation for Inverter-interfaced Power Sources Considering Saturation Element,"*2021 IEEE 4th International Electrical and Energy Conference (CIEEC)*, Wuhan, China, 2021.

J1. Z. Yang, Z. Liu, Q. Zhang, Z. Chen, J. d. J. Chavez, and M. Popov, "A Control Method for Converter-interfaced Sources to Improve Operation of Directional Protection Elements," in *IEEE Trans. Power Del.*, accepted.

CHAPTER 3. ADVANCED CONTROL TECHNOLOGIES FOR THE CORRECT OPERATION OF DISTANCE RELAYS

Besides directional elements, distance relays are also a common protective relay on the transmission line. In this chapter, the severe challenges of distance relays will be analyzed after CIRESs are connected. After that, two control methods are put forth to enhance the operations of distance relays. One is to design a new fault control scheme to generate a fundamental frequency fault current to make distance relays work properly. The other one is that the harmonic current is provided into the grid from CIRESs, and the apparent harmonic impedance is computed to eliminate the impact of the remote infeed.

3.1. ADAPTIVE ANALYSIS OF DISTANCE RELAYS

3.1.1. PHASE TO EARTH LOOP

There is a phase-to-earth loop for single-line ground faults, line-to-line ground faults, and three-phase ground faults. For a single-line ground fault, the fault phase is earthed by R_g while the faulty phases are connected by $2R_g$, and the middle is earthed by R_f for BCG faults, as seen in Figure 3-3. The apparent impedances are stated as follows when a line-A ground (AG) fault or a line-B-to-line-C ground (BCG) fault arises [99]:

$$Z_{ag} = Z_{k1} + \underbrace{\left(\frac{\dot{I}_{WA} + \dot{I}_{SA}}{\dot{I}_{WA} + k_0 \cdot 3\dot{I}_{W0}} \right)}_{M_{ag}} R_g \tag{3.1}$$

$$Z_{bg} = Z_{k1} + \underbrace{\left(\frac{\dot{I}_{WBC} + \dot{I}_{SBC}}{\dot{I}_{WB} + k_0 \cdot 3\dot{I}_{W0}} \right)}_{M_{bg1}} R_f + \underbrace{\left(\frac{\dot{I}_{WB} + \dot{I}_{SB}}{\dot{I}_{WB} + k_0 \cdot 3\dot{I}_{W0}} \right)}_{M_{bg2}} R_g \tag{3.2}$$

where subscripts W and S are the electrical components on the CIRES side and the grid side, Z_{k1} means the positive-sequence line impedance from the fault site to the relay site, and k_0 denotes the zero-sequence compensation factor. Additionally, $\dot{I}_{WBC}=\dot{I}_{WB} + \dot{I}_{WC}$, $\dot{I}_{SBC}=\dot{I}_{SB} + \dot{I}_{SC}$.

The zero-sequence current dominates the fault current for earth faults on the CIRES side since the high-voltage terminal of the main transformer is grounded. At the same

time, the zero-sequence equivalent impedance of the connected grid is often smaller than that of the main transformer, so there is also a large zero-sequence fault current on the grid side. In addition, the positive- and negative-sequence fault currents are also very large, so $\dot{I}_{\mathrm{SA}}$ is much higher than $\dot{I}_{\mathrm{WA}}$. Under this circumstance, the M_{ag} amplitude in (3.1) is far higher than 1, thus the additional impedance has a big amplitude that prevents the activation of distance relays. Moreover, because of the substantial zero-sequence fault current between the two terminals, the small angle difference between the two terminals leads to the dominant resistive component in the additional impedance. The analysis presented above also applies to (3.2).

3.1.2. PHASE-TO-PHASE FAULT LOOP

There are phase-to-phase fault loops for line-to-line faults, three-phase faults, and phase-to-phase ground faults. For line-to-line faults, the faulty phases are connected by R_{g}, as seen in Figure 3-3. The following does not include the apparent impedance expression for three-phase faults because it is the same as the expression for phase-to-phase faults. The measured impedance detected by distance relays is described as follows for line-B-to-line-C (BC) faults and BCG faults [26]:

$$Z_{\mathrm{bc}} = Z_{\mathrm{k1}} + \underbrace{\left(\frac{\dot{I}_{\mathrm{WB}} + \dot{I}_{\mathrm{SB}}}{\dot{I}_{\mathrm{WB}} - \dot{I}_{\mathrm{WC}}} \right)}_{M_{\mathrm{bc}}} R_{\mathrm{g}} \tag{3.3}$$

$$Z_{\mathrm{bcg}} = Z_{\mathrm{k1}} + \underbrace{\left(1 + \frac{\dot{I}_{\mathrm{SB}} - \dot{I}_{\mathrm{SC}}}{\dot{I}_{\mathrm{WB}} - \dot{I}_{\mathrm{WC}}} \right)}_{M_{\mathrm{bcg}}} R_{\mathrm{g}} \tag{3.4}$$

The fault current on the CIRES terminal for line-to-line faults only contains the positive-sequence current when DCC control is used because no zero-sequence fault current is present on both terminals. When compared to grounding faults, the current amplitude between two terminals will have a greater difference because the fault current produced by CIRESs is restrained to 1.2 to 1.5 times the nominal current. Under conventional FRT techniques, a significant current angle disparity between both terminals will appear. Consequently, the additional impedance is greater than the corresponding value for grounding faults because M_{bc} in (3.3) has a larger amplitude and angle than M_{ag} in (3.1). As a result, the fault resistance is more likely to affect distance relays. In addition, the zero-sequence current component for line-to-line ground faults will be canceled out by the equations $\dot{I}_{\mathrm{SB}} - \dot{I}_{\mathrm{SC}}$ and $\dot{I}_{\mathrm{WB}} - \dot{I}_{\mathrm{WC}}$ in (3.4). Therefore, the amplitude and the angle of M_{bcg} will have such big values that distance relays may be not activated for internal faults.

In summary, the remote infeed will lead to amplified fault resistance, especially for phase-to-phase faults, so the operation of distance relays will be undermined due to the CIRES integration.

3.2. FAULT COORDINATION CONTROL METHOD

In order to make distance relays work properly, the required fault current angle is derived from the basic principle of distance relays. Following that, the associated current command values are computed considering the FRT conditions including reactive current injection and the current restraint.

3.2.1. THE REQUIRED CURRENT ANGLE

A. Single-line grounding faults

The apparent impedance for single-line earth faults is given in (3.1). It can be known from (3.1) that when the angle of M_{ag} is controlled to 0°, the reactance component is not included in the additional impedance $M_{ag}R_g$. Under this circumstance, the apparent reactance is equivalent to the line reactance from the relay site to the fault site. To achieve this point, it is necessary to examine the relationship between the positive-sequence current angle of CIRES and the angle of M_{ag}.

The sequence fault network (Figure 3-3) is shown in Figure 3.1 for an AG fault at L_{12}. Z_p stands for the line L_{12} sequence impedances, Z_k denotes the line impedance from the relay site to the fault site, Z_T denotes the main transformer impedance, and Z_g denotes the impedance sum of the grid and line L_{23}. $\dot{U}_s$ denotes the internal potential of the connected grid. In addition, the positive-sequence fault loop of CIRESs is modeled as a controlled current source $\dot{I}_c$, and the negative-sequence equivalent fault loop of CIRESs can be seen as an open circuit since the negative-sequence fault current is not injected when the DCC is used [44].

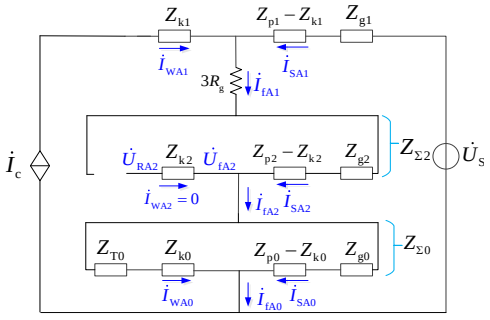

Figure 3.1 Sequence fault network for an AG fault. Source: J2 [100].

As shown in Figure 3-1, sequence currents conform to the relationship below [100]:

$$\begin{cases} \dot{I}_{\mathrm{fA1}} = \dot{I}_{\mathrm{WA1}} + \dot{I}_{\mathrm{SA1}} \\ \dot{I}_{\mathrm{fA2}} = \dot{I}_{\mathrm{SA2}} \\ \dot{I}_{\mathrm{fA0}} = \dot{I}_{\mathrm{WA0}} + \dot{I}_{\mathrm{SA0}} \end{cases}, \dot{I}_{\mathrm{fA1}} = \dot{I}_{\mathrm{fA2}} = \dot{I}_{\mathrm{fA0}} \tag{3.5}$$

When (3.5) is substituted for M_{ag} in (3.1), (3.6) can be obtained:

$$M_{\mathrm{ag}} = \frac{\dot{I}_{\mathrm{fA1}} + \dot{I}_{\mathrm{fA2}} + \dot{I}_{\mathrm{fA0}}}{\dot{I}_{\mathrm{WA1}} + k_0 \cdot 3\dot{I}_{\mathrm{WA0}}} = \frac{3\dot{I}_{\mathrm{SA2}}}{\dot{I}_{\mathrm{WA1}} + k_0 \cdot 3\dot{I}_{\mathrm{WA0}}} \tag{3.6}$$

With reference to sequence boundary requirements, the phase angle of $\dot{I}_{\mathrm{SA2}}$ in (3.6) is equivalent to that of $\dot{I}_{\mathrm{WA0}}$, hence the CIRES positive-sequence fault current angle is necessary to fulfill (3.7) for M_{ag}'s phase angle to be equal to 0°:

$$\angle\dot{I}_{\mathrm{WA1}} = \angle\dot{I}_{\mathrm{SA2}} \tag{3.7}$$

In a similar way, the positive-sequence fault current angle of CIRESs should satisfy (3.8) for BG and CG faults:

$$\begin{cases} \angle\dot{I}_{\mathrm{WB1}} = \angle\dot{I}_{\mathrm{SB2}}, \ \mathrm{BG} \\ \angle\dot{I}_{\mathrm{WC1}} = \angle\dot{I}_{\mathrm{SC2}}, \ \mathrm{CG} \end{cases} \tag{3.8}$$

B. line-to-line faults

From (3.3), it is clear that M_{bc}'s phase angle must be exactly 0° for the apparent reactance to equal the line reactance from the relay site to the fault site. The sequence boundary conditions must first be supplied for a BC fault to express M_{bc} using sequence fault currents [100]:

$$\begin{cases} \dot{I}_{\mathrm{fA1}} = -\dot{I}_{\mathrm{fA2}} \\ \dot{I}_{\mathrm{fB1}} + \dot{I}_{\mathrm{fB2}} = \alpha^2 \dot{I}_{\mathrm{fA1}} + \alpha \dot{I}_{\mathrm{fA2}} \\ \dot{I}_{\mathrm{WB1}} - \dot{I}_{\mathrm{WC1}} = -\mathrm{j}\sqrt{3}\dot{I}_{\mathrm{WA1}} \end{cases} \tag{3.9}$$

where α denotes the rotating factor.

When (3.9) is substituted for M_{bc} in (3.3), it can result in:

$$M_{\mathrm{bc}} = \frac{\dot{I}_{\mathrm{fB1}} + \dot{I}_{\mathrm{fB2}}}{\dot{I}_{\mathrm{WB1}} - \dot{I}_{\mathrm{WC1}}} = -\frac{\dot{I}_{\mathrm{fA2}}}{\dot{I}_{\mathrm{WA1}}} \tag{3.10}$$

The positive-sequence fault current angle of CIRESs must satisfy the following conditions to adjust the phase angle of M_{bc} to 0°:

$$\angle \dot{I}_{WA1} = \angle \dot{I}_{fA2} - 180^\circ = \angle \dot{I}_{SA2} - 180^\circ \tag{3.11}$$

It is better to compute the angle of $\dot{I}_{SA2}$ in the above equation with the local data, and the used approach is described in Section 3.2.2.

Likewise, it is possible to determine the analogous conditions for AB and CA faults:

$$\begin{cases} \angle \dot{I}_{WB1} = \angle \dot{I}_{SB2} - 180^\circ, \text{CA} \\ \angle \dot{I}_{WC1} = \angle \dot{I}_{SC2} - 180^\circ, \text{AB} \end{cases} \tag{3.12}$$

C. line-to-line grounding faults

For line-to-line ground faults, there are two line-to-ground fault loops and one phase-to-phase fault loop, thus the apparent impedances detected by two kinds of fault loops are examined independently.

1) Phase-to-phase fault loop. For a BCG fault at L_{12}, the apparent impedance of R_{12} has been given in (3.4).

The following are the boundary conditions of sequence currents for a BCG fault [100]:

$$\dot{I}_{fA1} + \dot{I}_{fA2} + \dot{I}_{fA0} = 0 \tag{3.13}$$

When (3.13) is substituted into M_{bcg} in (3.4), (3.14) is obtained:

$$M_{bcg} = \frac{\left(\dot{I}_{fB1} - \dot{I}_{fC1}\right) + \left(\dot{I}_{fB2} - \dot{I}_{fC2}\right)}{\dot{I}_{WB1} - \dot{I}_{WC1}} = -\frac{2\dot{I}_{fA2} + \dot{I}_{fA0}}{\dot{I}_{WA1}} \tag{3.14}$$

Since $3R_f$ is connected in series into the zero-sequence loop for the BCG sequence fault network, $\dot{I}_{fA2}$ will typically be greater than $\dot{I}_{fA0}$. Currently, $2\dot{I}_{fA2}$will dominate the numerator of M_{bcg}, and the smaller $\dot{I}_{fA0}$ will lead to a tiny positive phase angle when $\angle \dot{I}_{WA1}$is adjusted to be equal to $\dot{I}_{fA2}$-180°. Distance relays can work better in this condition by rotating the operational zone counterclockwise since $M_{bcg}R_g$ has a small inductive reactance component.

2) Line to ground fault loop. The apparent impedance detected at R_{12} has been displayed in (3.2) for a BCG fault, and the apparent impedance consists of two additional impedances, $M_{bg1}R_f$ and $M_{bg2}R_g$, hence M_{bg1} and M_{bg2} should be examined individually.

When (3.13) is substituted into M_{bg1} in (3.14), it can result in:

$$M_{bg1} = \frac{\dot{I}_{fB1} + \dot{I}_{fC1} + \dot{I}_{fB2} + \dot{I}_{fC2} + 2\dot{I}_{fC0}}{\dot{I}_{WB} + k_0 \cdot 3\dot{I}_{WB0}} = \frac{3\dot{I}_{fB0}}{\dot{I}_{WB1} + k_0 \cdot 3\dot{I}_{WB0}} \tag{3.15}$$

The condition in (3.16) must be met to make M_{bg1}'s phase angle equal to 0°:

$$\angle\dot{I}_{WB1} = \angle\dot{I}_{fB0} = \angle\dot{I}_{WB0} \tag{3.16}$$

In this situation, the angle of M_{bg2} is analyzed as follows:

$$M_{bg2} = \frac{\dot{I}_{WB} + \dot{I}_{SB}}{\dot{I}_{WB} + k_0 \cdot 3\dot{I}_{WB0}} = \frac{\dot{I}_{fB}}{\dot{I}_{WB1} + k_0 \cdot 3\dot{I}_{WB0}} \tag{3.17}$$

When $\angle\dot{I}_{WB1}$ is equal to $\dot{I}_{WB0}$, $\angle\dot{I}_{fB}$ leads $\dot{I}_{WB0}$ by an angle, therefore the phase angle of M_{bg2} is greater than 0°. Additionally, because of the zero-sequence fault current and the fact that R_g is the arc resistance with a small value, $M_{bg2}R_g$ will not have a very large amplitude. As a result, rotating the operational zone counterclockwise will enhance the operations of distance relays.

In summary, by adjusting the CIRES positive-sequence current angle, the additional impedance can become a purely resistive component for AG and BC faults. For BCG faults, the protection zone is rotated to elevate the operations of distance relays.

3.2.2. SUITABLE CURRENT REFERENCES

A. The controller based on DCC

Distance protection must first identify different fault kinds before it can pinpoint the fault loop. We can utilize the method described in [96] that is relying on the relative angle between the sequence voltages.

It is possible to select the appropriate fault loop once the fault type has been determined. To elevate the operations of distance relays for various fault kinds, the positive-sequence current angle of CIRESs is ought to meet diverse requirements, as shown in the theoretical analysis in Section 3.2.1. For R_{12}, an approach must be developed to compute the negative-sequence current angle on the grid side using only the local data because it cannot be measured directly.

There is no negative-sequence fault current output from CIRESs for the controller based on DCC, hence the negative-sequence voltage detected at R_{12} in Figure 3-3 is identical to the negative-sequence voltage at the position of the fault, which is [100]:

$$\dot{U}_{\mathrm{RA2}} = \dot{U}_{\mathrm{fA2}} \tag{3.18}$$

Based on this, the negative-sequence fault current angle on the grid side is computed:

$$\angle \dot{I}_{\mathrm{SA2}} = \angle \dot{U}_{\mathrm{RA2}} - \angle Z_{\mathrm{SL2}} + 180^{\circ} \tag{3.19}$$

Where Z_{SL2} denotes the negative-sequence impedance at the right side of the fault location, and the impedance angle is constant at 84.29° in the established model.

Following that, the necessary CIRES positive-sequence fault current angle is determined for various fault loops. After that, according to (2.10), it is clear that the current command values can regulate the positive-sequence current angle. Therefore, for a specific current angle, the corresponding command values should meet (3.20):

$$i_{\mathrm{1dref}} = \frac{i_{\mathrm{1qref}}}{\tan(\angle \dot{I}_{\mathrm{WA1}} - \theta_{\mathrm{1v}} - 90^{\circ})} \tag{3.20}$$

i_{1qref} in (3.20) is provided in accordance with the particular FRT technique shown in Figure 3-2 [101], and then, the relevant i_{1dref} is determined by (3.20).

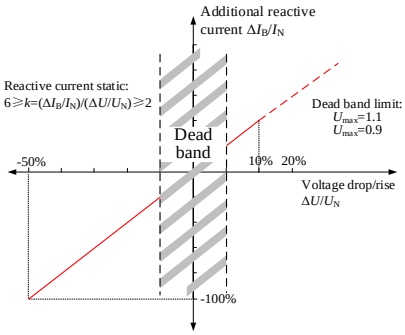

Figure 3-2 A FRT Strategy for reactive current. Source: J2 [100].

The aforementioned procedure does not account for the CIRESs' current restraint. Therefore, current command values should be changed below to prevent overcurrent:

$$\begin{cases} i'_{\mathrm{1dref}} = i_{\mathrm{1dref}} / N \\ i'_{\mathrm{1qref}} = i_{\mathrm{1qref}} / N \end{cases}, N = \max\left(1, \frac{\sqrt{i_{\mathrm{1dref}}^2 + i_{\mathrm{1qref}}^2}}{\gamma}\right) \tag{3.21}$$

In this case, if $\sqrt{i_{\mathrm{1dref}}^2 + i_{\mathrm{1qref}}^2}$ is higher than γ, i'_{1qref} would be lower than the specified value in Figure 3-2, yet this represents an essential concession because the limited current is more crucial to safeguarding power inverters. If not, it will be equivalent to

the value that is computed in Figure 3-2. Current references settled with respect to (3.21) function effectively for distance relays since there is no inclusion of reactance component in the additional impedance.

B. The controller based on DSC

Besides the DCC, the suggested method is also applicable for the controller based on DSC when the negative-sequence fault current is provided from CIRESs. The sequence currents should also fulfill (3.22) when combined with the expression of M_{ag} and sequence boundary conditions for AG faults [100]:

$$\angle \dot{I}_{WA1} = \angle \dot{I}_{WA2} = \angle \dot{I}_{fA2} = \angle \dot{I}_{SA2} \tag{3.22}$$

Following that, i_{1dref} and i_{1qref} are computed in the same manner as the case when the negative-sequence fault current is not present. The computation of negative-sequence current references is analogous. Negative-sequence current command values should meet (3.23) with respect to (3.20):

$$i_{2dref} = \frac{i_{2qref}}{\tan(-\theta_{2v} + 90^{\circ} - \angle \dot{I}_{WA2})} \tag{3.23}$$

Then, i_{2qref} is provided using the VDE-AR-N 4120 Rules in [20] and is settled with reference to the incremental negative sequence voltage. i_{2dref} is then calculated using (3.23). To prevent overcurrent, all the command values must be reduced:

$$\begin{cases} i'_{1dref} = i_{1dref} / M, \; i'_{1qref} = i_{1qref} / M \\ i'_{2dref} = i_{2dref} / M, \; i'_{2qref} = i_{2qref} / M \end{cases} \tag{3.24}$$

where M is:

$$M = \max\left(1, \frac{\sqrt{\left(\left|i_{1dref}\right| + \left|i_{2dref}\right|\right)^2 + \left(\left|i_{1qref}\right| + \left|i_{2qref}\right|\right)^2}}{\gamma}\right) \tag{3.25}$$

When current references are given according to (3.24), the performance of distance relays will be enhanced. Since the converter control needs one or two cycles to come into the stable state, this method is slightly slower than the common operating time of distance relays.

3.2.3. SIMULATION ANALYSIS

The simulation topology is displayed in Figure 3-3. The lines L_{12} and L_{23} are respectively 60 km and 40 km long, and the voltage levels for both are 220 kV. In addition, the CIRES capacity is 200 MW, and the impedance of the equivalent grid is 0.31+ j3.14 Ω. In the case of distance relay R_{12}, zone I covers 80% of the total line, zone II covers 125% of the local line, and the resistive reach is settled to be 100 Ω.

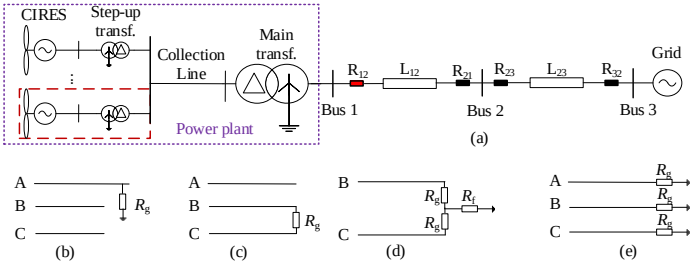

Figure 3-3 Simulation topology. (a) The system topology, (b) AG, (c) BC, (d) BCG, (e) ABCG.

A. The controller based on DCC

Figure 3-4 shows the related measurements of the controller and R_{12} when a BC fault occurs at 40% of L_{12} with 20 Ω of R_g, and the suggested control method is performed. Additionally, Figure 3-4 also provides the apparent impedance for traditional FRT.

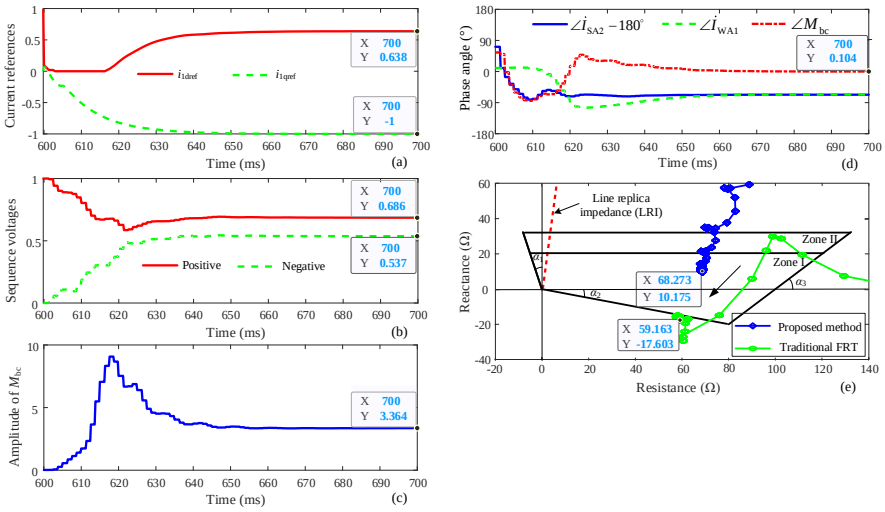

Figure 3-4 The related measurements for a BC fault. (a) Current references, (b) sequence voltage, (c) magnitude of M_{bc}, (d) angle of M_{bc}, (e) apparent impedance. Source: J2 [100].

The starting time of the fault is 0.6 s in Figure 3-4. i_{1dref} is equal to 0.638 and i_{1qref} equals -1 at 700 ms, as illustrated in Figure 3-4(a), which is settled with reference to the voltage drop in Figure 3-4(b). Because M_{bc} in Figure 3-4(c) has an amplitude of 3.364, the effect of fault resistance will be increased. Figure 3-4(d) shows that the CIRES positive-sequence current angle, $\angle\dot{I}_{WA1}$, is equal to $\angle\dot{I}_{SA2}$-180°, matching the control target in (3.11). In this case, the angle of M_{bc} in Figure 3-4(e) will be close to 0°, so the distance relay can function as intended because R_{12} observes an apparent reactance of 10.175 Ω, which approaches the line fault reactance of 10.368 Ω, but the apparent impedance is out of the protection zone if the conventional FRT is used. The simulation results for other fault cases can be observed in J2.

B. The controller based on DSC

The relay R_{12}'s measurements for an AG fault with 50 Ω of R_g at 40% of L_{12} are displayed in Figure 3-5.

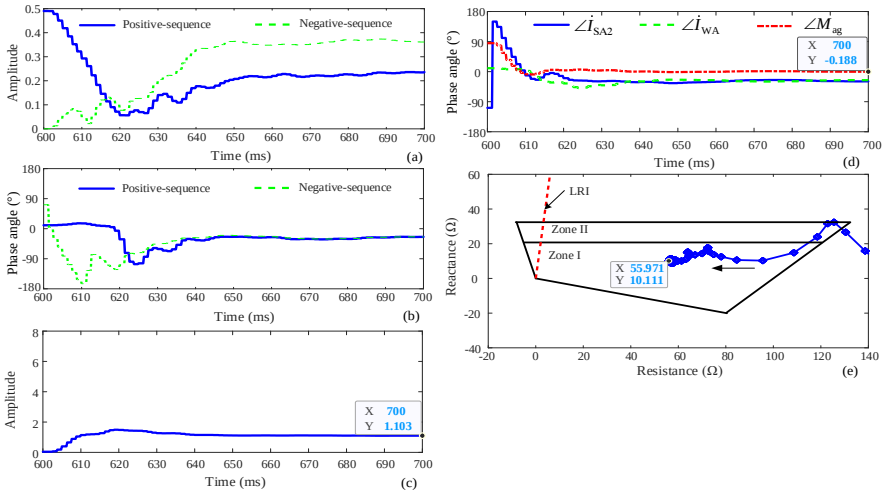

Figure 3-5 Associated measurements of R_{12} for an AG fault. (a) Current magnitude, (b) current angle, (c) M_{ag} amplitude, (d) M_{ag} angle, (e) apparent impedance. Source: J2 [100].

Figure 3-5 (a) and (b) show that a sizable negative-sequence fault current is generated from CIRESs, and the angle of $\dot{I}_{WA1}$ is regulated to equal that of $\dot{I}_{WA2}$. Currently, in Figure 3-5(c) and (d), the angle and amplitude of M_{ag} are -0.188° and 1.103. At this time, the apparent reactance in Figure 3-5(e) is near the line fault reactance of 10.368 Ω due to this narrow phase angle, allowing the distance relay to function as intended.

3.2.4. RTDS VERIFICATION

The suggested control-based scheme is also validated based on the RTDS experiment platform when the controller based on DCC is used. Figure 3-6 shows the associated

measurements of R_{12} when an AG fault with 100 Ω of R_g and a BC fault with 20 Ω of R_g arise at 40% of L_{12}.

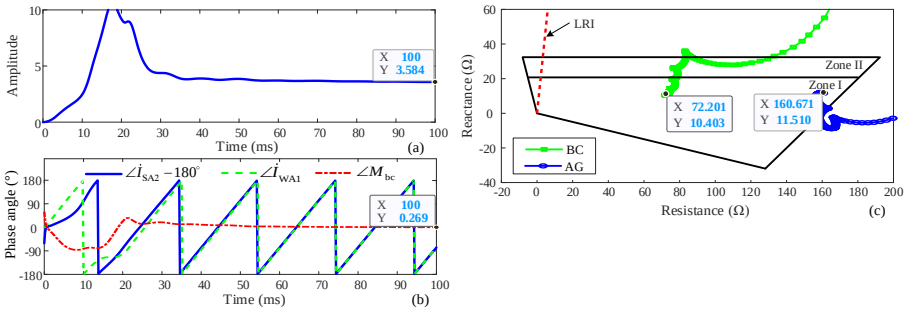

Figure 3-6 The associated measured data of R_{12} for a BC fault and an AG fault at 40% of L_{12}. (a) Magnitude of M_{bc}, (b) angle of M_{bc}, (c) impedance trace. Source: J2 [100].

When $\angle \dot{I}_{WA1}$ is regulated to be equal to $\angle \dot{I}_{SA2}$-180° for this BC fault, the amplitude of M_{bc} in Figure 3-6(a) is 3.584, and the phase angle of M_{bc} in Figure 3-6(b) is near 0°, thus the apparent reactance will approach the line fault reactance of 10.368 Ω, as shown in Figure 3-6(c). As a result, the operation of distance relays is enhanced. Additionally, a similar instance with AG faults is shown in Figure 3-6(c). But for this AG fault, the resistive part contained in the apparent impedance is so big, necessitating an increase in the resistive reach to 160 Ω. The maximum recommended resistive reach is 200 Ω for the examined power network since the load resistance measured at R_{12} is 244.444 Ω. These instances once more support the suggested method.

3.3. HARMONIC INJECTION-BASED DISTANCE RELAYS

Another method to elevate the operations of distance relays is proposed in this section. A 2nd order harmonic is provided by CIRESs through the PI controller. However, there is no this harmonic current on the remote end. Therefore, the apparent harmonic impedance can indicate the fault distance.

3.3.1. BASIC IDEA

Figure 3-7 depicts the fault loop for an AG failure with R_g when a certain harmonic current is generated from the inverter of CIRESs (The system topology is the same as Figure 2-8). $\dot{I}_{da}^{H}$ denotes the regulated harmonic current source. In addition, the harmonic currents on the grid side, the CIRES side, and the fault site are denoted as $\dot{I}_{SA}^{H}$, $\dot{I}_{WA}^{H}$, and $\dot{I}_{k}^{H}$, respectively. The transmission line's overall positive-sequence harmonic impedance is denoted as Z_{1L}^{H}, and the positive-sequence harmonic impedance of the transmission line from the fault site to the relay site is marked as Z_{1k}^{H}. Additionally, Z_{1s}^{H} stands for the grid's positive-sequence harmonic impedance.

It is apparent from Figure 3-7 that because the harmonic current is not present on the grid side, and R_g and the total value of $(Z_{1L}^H - Z_{1k}^H)$ and Z_{1s}^H constitute a parallel branch, I_k^H must be less than I_{WA}^H due to the current divider. M_{ag}^H will be less than 1 at this moment based on the measured harmonic impedance in (3.26). Therefore, the apparent harmonic impedance detected at the relay site could indicate the fault distance because the influence of fault resistance is suppressed [99].

$$Z_{ag}^H = Z_{1k}^H + \frac{\dot{I}_k^H}{\underbrace{\dot{I}_{WA}^H + k_0^H \cdot 3\dot{I}_{W0}^H}_{M_{ag}^H}} R_g \tag{3.26}$$

where superscript H denotes the related harmonic quantities.

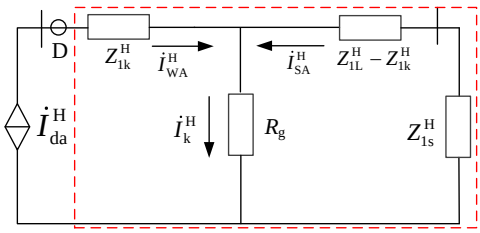

Figure 3-7 The fault harmonic circuit. Source: J3 [99].

3.3.2. FREQUENCY RESPONSE

It is necessary to study the frequency response of the controller to provide a certain harmonic into the grid. The PI controller is frequently utilized in the current control loop because it could follow constant command values without any static error. The tuning method of the PI controller and the corresponding system model have been given in (2.6) and (2.7). After that, a periodic signal in (3.27) is superimposed at the D axis because i_{1qref} is related to the reactive power injected from CIRESs [99]:

$$i_{dz}(t) = M \sin \omega_h t \tag{3.27}$$

The transfer function method can be used to determine how it will actually react in the present control loop combined with the system transfer function $G_0(s)$ in (2.7):

$$I_{dp}(s) = I_{dz}(s) \cdot G_0(s) = M \frac{\omega_h}{s^2 + \omega_h^2} \frac{\omega_c}{s + \omega_c} \tag{3.28}$$

The time-domain expression for the D-axis current is computed when the inverse Laplace transform is executed for (3.28):

$$i_{\mathrm{dp}}(t)=M\frac{\omega_{\mathrm{c}}\omega_{\mathrm{h}}}{\omega_{\mathrm{c}}^{2}+\omega_{\mathrm{h}}^{2}}\left(e^{-\omega_{\mathrm{c}}t}-\cos\omega_{\mathrm{h}}t\right)+M\frac{\omega_{\mathrm{c}}^{2}}{\omega_{\mathrm{c}}^{2}+\omega_{\mathrm{h}}^{2}}\sin\omega_{\mathrm{h}}t \tag{3.29}$$

Because of the large cut-off frequency ω_{c}, the DC component in (3.29) will soon fade to zero. Currently, (3.29) is simplified as:

$$\begin{aligned} i_{\mathrm{dps}}(t)&=M\frac{\omega_{\mathrm{c}}}{\sqrt{\omega_{\mathrm{c}}^{2}+\omega_{\mathrm{h}}^{2}}}\sin\left(\omega_{\mathrm{h}}t-\arctan\frac{\omega_{\mathrm{h}}}{\omega_{\mathrm{c}}}\right)\\ &=MA_{\mathrm{p}}\sin\left(\omega_{\mathrm{h}}t-\psi\right)\end{aligned} \tag{3.30}$$

As observed in (3.30), The actual D-axis current is less than the injected AC signal because A_{P} is smaller than 1. In addition, there is an angle difference between the superimposed signal and the actual harmonic current, but it does not influence the harmonic impedance calculation. Moreover, because the current loop uses feedforward decoupling, and the outer DC voltage control loop is shut down during a fault, i_{dqs}(t) won't be fed back to create additional harmonics.

In this case, the current for the D-axis has a settled DC component $i_{1\mathrm{d}}$ and an actual AC component $i_{\mathrm{dps}}(t)$, and the current for Q-axis includes a DC component $i_{1\mathrm{q}}$. Currently, the 2r/3s transformation can be used to determine the currents in the ABC frame:

$$\begin{bmatrix} i_{\mathrm{a}}\\ i_{\mathrm{b}}\\ i_{\mathrm{c}}\end{bmatrix}=\begin{bmatrix} \sin\theta & \cos\theta & 1\\ \sin\left(\theta-120^{\circ}\right) & \cos\left(\theta-120^{\circ}\right) & 1\\ \sin\left(\theta+120^{\circ}\right) & \cos\left(\theta+120^{\circ}\right) & 1\end{bmatrix}\begin{bmatrix} i_{1\mathrm{d}}+i_{\mathrm{dps}}\\ i_{1\mathrm{q}}\\ 0\end{bmatrix} \tag{3.31}$$

where θ stands for the phase-locked angle, which is written as $\omega_0 t+\theta_{1\mathrm{p}}$. Based on (3.31), the phase-A current formula is as follows:

$$\begin{aligned} i_{\mathrm{da}}(t)=&-\frac{1}{2}MA_{\mathrm{p}}\cos\left(\left(\omega_{\mathrm{h}}+\omega_0\right)t+\theta_{1\mathrm{p}}-\psi\right)+i_{1\mathrm{q}}\cos\left(\omega_0 t+\theta_{1\mathrm{p}}\right)\\ &+\frac{1}{2}MA_{\mathrm{p}}\cos\left(\left(\omega_0-\omega_{\mathrm{h}}\right)t+\theta_{1\mathrm{p}}+\psi\right)+i_{1\mathrm{d}}\sin\left(\omega_0 t+\theta_{1\mathrm{p}}\right)\end{aligned} \tag{3.32}$$

As can be seen from (3.32), an n-th harmonic signal added on the D-axis will lead to the n+1 th and n-1 th harmonic currents measured at the relay site. The fault currents for phase B and phase C are similar to (3.32), but the angle lags or leads by 120°.

3.3.3. HARMONIC SELECTION

The harmonic order at the relay site is selected taking into account the factors below:

1) Overhead lines are typically used for the high-voltage transmission line. At the fundamental frequency, the line model of the π-type can be used for the transmission line less than 300 km [102]. The grounding capacitive reactance and line reactance of the overhead line will decrease and grow in proportion to frequency, respectively, hence the appropriate length of the π-type equivalent model for an *n*-th harmonic can be [100]:

$$L_{\mathrm{n}} = 300/n \tag{3.33}$$

The harmonic frequency can be selected from 2 and 3 because the overhead line integrated into CIRESs is often between tens and 100 km long [36]. The fourth harmonic is also suitable if the length of the overhead line is less than 75 km. The difference between the π-type model and the frequency-dependent model at these frequencies is negligible.

2) As the odd harmonics are common for the power grid [103], the 2nd or 4th harmonic is used to prevent obstruction. As a result, the third harmonic should work as the added signal on the D-axis.

3) To ensure that the protective relay can detect the harmonic current, the injected harmonic must have a certain amplitude. However, the added D-axis signal should be limited to decrease the waveform distortion and leave adequate space for the FRT scheme, hence the added signal should be 0.2 to 0.3 p.u. [104].

4) The harmonic injection duration is ought to be smaller than the total time of the breaker opening time and the protection operating time on the remote end (about 100 ms) to prevent controller instability [105], [106]. Therefore, the harmonic injection duration is settled at 100 ms.

3.3.4. THE IMPACT OF HARMONIC INJECTION

The negative-sequence voltage will cause a twofold frequency fluctuation in the positive-sequence DQ-axis voltages $u_{1\mathrm{d}}$ and $u_{1\mathrm{q}}$ for asymmetrical faults. After a 3rd harmonic current is added on the D-axis, the active power provided by CIRESs would exhibit fifth frequency oscillations besides its power frequency. Additionally, the constant current component may cause the active power to fluctuate at the twofold frequency [12]. The DC voltage will fluctuate in the same ways that the active power does. However, during the onset of the fault, the voltage control loop would be shut

down, preventing these fluctuations from entering the controller again to generate additional harmonics.

The 2nd and 4th harmonics will be injected into the power grid by adding a 3rd order harmonic on the D-axis, and these harmonics may raise the fault current peak value of CIRESs. When the angles of different harmonics in (3.32) are ignored, the greatest peak value is expressed by (3.34).

$$i_{\text{peak}} = MA_{\text{p}} + \sqrt{i_{1\text{dref}}^2 + i_{1\text{qref}}^2} \tag{3.34}$$

After $i_{1\text{qref}}$ is given by the particular FRT scheme, $i_{1\text{dref}}$ should meet (3.35) because the peak value should be restricted from 1.2 p.u. to 1.5 p.u. [94], [98]:

$$i_{1\text{dref}} = \sqrt{\left(\gamma - MA_{\text{p}}\right)^2 - i_{1\text{qref}}^2} \tag{3.35}$$

In summary, the protection flowchart can be observed in Figure 3-7. The 2nd harmonic is provided into the power grid after a fault happens. Distance relays then extract harmonic voltage and current phasors and compute the apparent harmonic impedance using the full-cycle Fourier technique. Distance relays would be activated to cut off the fault with the appropriate delay if the apparent harmonic impedance comes into zones I and II. If not, the protective relay will not be activated.

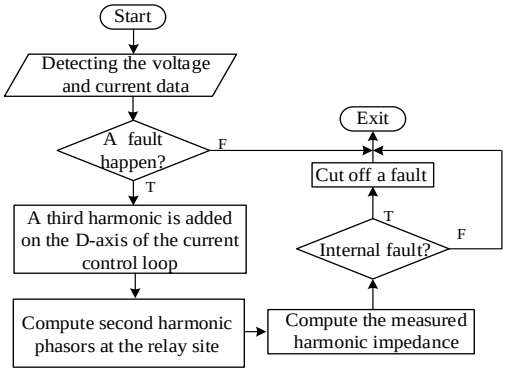

Figure 3-8 The detailed flow chart. Source: J3 [99].

3.3.5. SIMULATION ANALYSIS

The simulation topology is the same as that in Figure 2-8. The nominal capacity of the CIRES power park is 100 MW, the overhead line length is 40 km, and its voltage level is 220 kV. In addition, the equivalent grid impedance is 0.1+j3.14 Ω. The protection range of zone I and zone II are 85% and 125% of the total line,

respectively, with a resistive reach of 100 Ω [52], hence $X_{\text{set}}^{\text{I}}$ and $X_{\text{set}}^{\text{II}}$ are calculated as 22.984 Ω and 33.8 Ω at the twofold frequency. Additionally, every fault happens at 0.6 s, γ is settled to 1.2, and M is settled to 0.2 p.u..

A. The injected harmonic current

At the D axis, the 3rd harmonic signal is added to enhance the operations of distance relays. Since ω_c is settled to 400π, the phase angle should be behind the injected signal by 36.870°, and the real harmonic current magnitude for the D-axis should be 0.16 p.u regarding (3.30). Figure 3-9 displays the magnitude and the angle of real and the injected currents on the D axis when an AG failure (with 20 Ω of R_g) appears at the midpoint of the line.

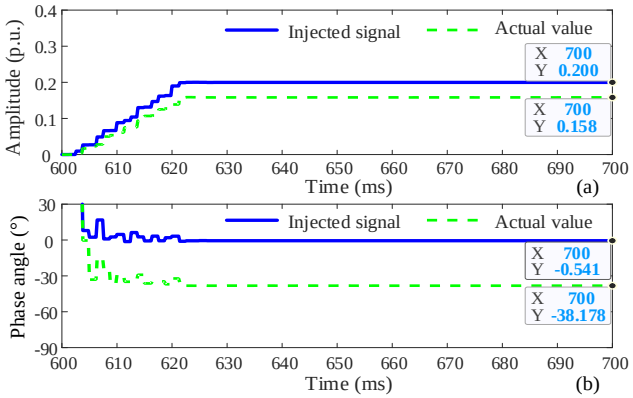

Figure 3-9 The currents on the D axis. (a) Amplitude, (b) phase angle. Source: J3 [99].

The real D-axis harmonic current is 0.158 p.u., which is extremely similar to the computed value of 0.16 p.u., as observed in Figure 3-9(a). In addition, the real current angle in Figure 3-9(b) will lag the applied signal by a value of 37.637°, which is nearly the same as the theoretical value of 36.870°. These events demonstrate the accuracy of (3.30).

In the meantime, Figure 3-10 illustrates the frequency spectrum of the phase-A fault current, three-phase fault currents, and the reactive power produced by CIRESs.

In Figure 3-10(a), three-phase currents are less than the restrained current value, ensuring that the inverter is not damaged by the added harmonic component. The phase-A current in Figure 3-10(b) currently only has a power frequency order, a 2nd order, and a 4th order, which is consistent with the study in (3.32). The FRT condition for reactive power injection is still met because the provided reactive power in Figure 3-10(c) will be essentially identical for the two FRT techniques.

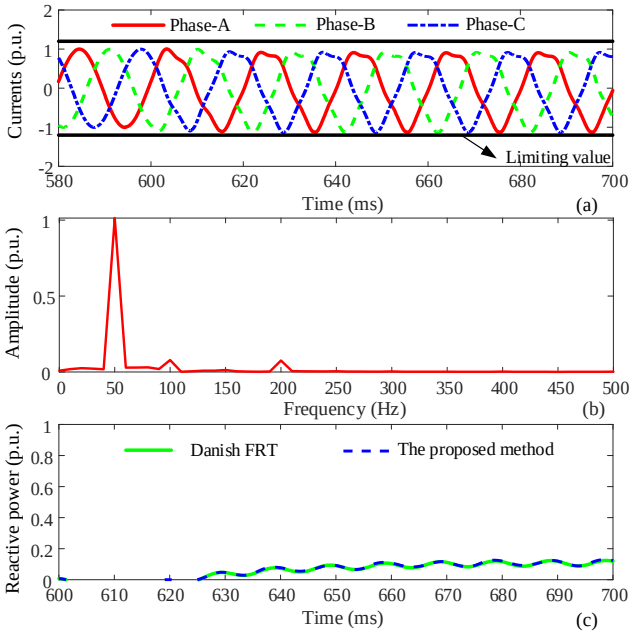

Figure 3-10 The related measurements from CIRESs. (a) Three-phase currents, (b) frequency spectrum, (c) reactive power. Source: J3 [99].

B. Zone I distance relay

The effectiveness of zone I distance relays is examined in this section. The apparent harmonic impedance is displayed in Figure 3-11 after a BC failure with 10 Ω of R_g and an AG fault with 20 Ω of R_g arise at the midpoint of the line. In addition, the amplitude and the angle of the numerator and denominator of M_{bc}^{H} is also presented in Figure 3-11.

Because the numerator of M_{bc}^{H} is less than the denominator, as seen in Figure 3-11(a), the additional impedance has a tiny value. At the same time, the resistive component dominates the additional impedance since the numerator angle of M_{bc}^{H} leads the denominator by 14.266° in Figure 3-11(b). For this BC fault, the reactance component included in the observed harmonic impedance just increases by 1.149 Ω compared to the line fault impedance of 1.52+j13.52 Ω, as shown in Figure 3-11(c), so the measured impedance enters zone I such that distance relays could be triggered instantly. For this AG failure, the increased reactance part is equal to 6.338 Ω, and it is still within zone I. However, distance relays are likely to fail due to the increased reactance component if a fault arises at the reach limit. To make distance relays have better performance, the protection zone can be rotated counterclockwise by a certain angle [59]. As for other fault scenarios, they can be found in J3.

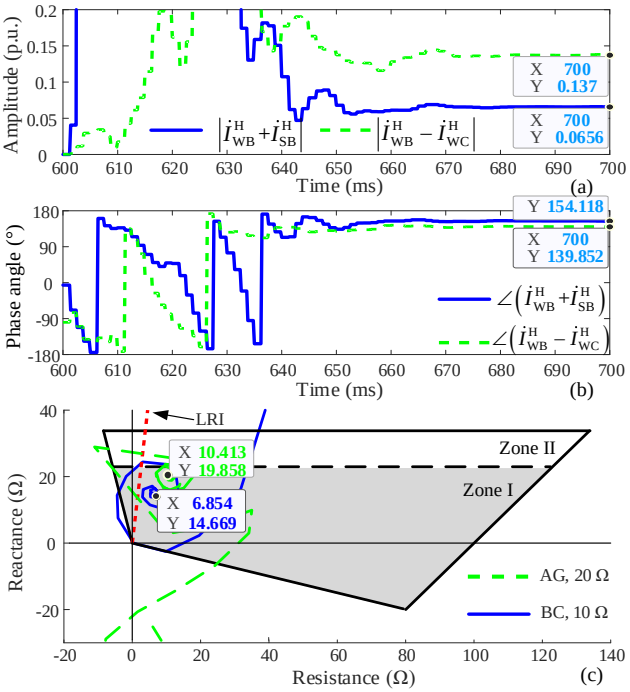

Figure 3-11 The associated measured data for the suggested method. (a) Magnitude, (b) phase angle, (c) measured harmonic impedance. Source: J3 [99].

3.3.6. RTDS VERIFICATION

The RTDS experiment testing is also performed to verify the suggested scheme. Figure 3-12 displays the observed harmonic impedance and the related measurements when a BC failure with a 20 Ω of R_g and an AG fault with a 100 Ω of R_g arise at the midpoint of the line.

The safe operation of the controller is guaranteed because the three-phase fault currents in Figure 3-12(a) are less than the current upper limit of the inverter for BC faults. The superimposed signal and the actual value on the D axis are shown in Figure 3-12(b), and both relationships satisfy (3.30) for this BC failure. The detected harmonic impedance in Figure 3-12(c) comes into zone I for this BC fault, so the distance relay can function as intended, but the measured impedance is stable at zone II for this AG fault because of high fault resistance, so the distance relay will trip with a time step of 0.3 to 0.5 s. These results further validate the suggested strategy.

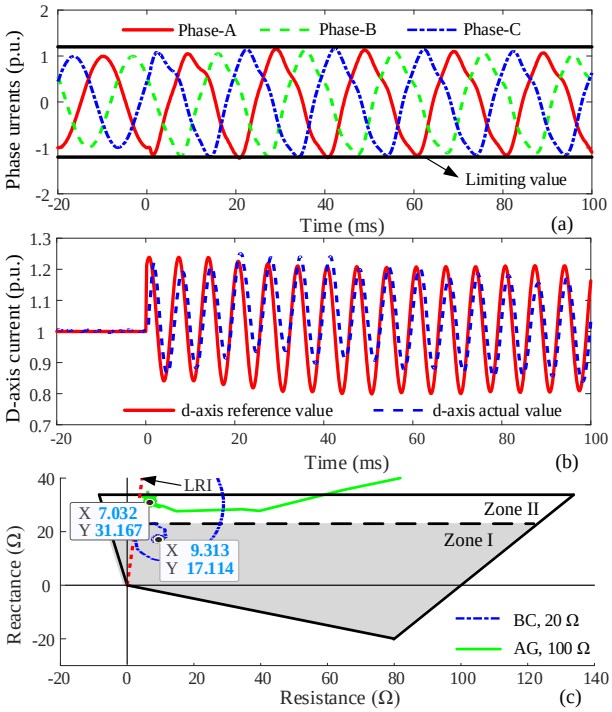

Figure 3-12 The fault current of CIRESs and the measured impedance based on RTDS. (a) Three-phase currents, (b) D-axis fault current, (c) harmonic impedance. Source: J3 [99].

3.4. SUMMARY

In this chapter, combined with the apparent impedance formula, it is found that distance relays may fail to be triggered due to the remote infeed, especially for phase-to-phase faults.

In order to deal with this issue, two schemes are put forth. One is to adjust the angle of the fundamental frequency current to ensure that the apparent reactance is equivalent to the line fault reactance by designing a suitable fault control scheme. Consequently, the apparent reactance could indicate the fault distance accurately while reactive current injection and the limited current condition can be satisfied.

The other method is to generate a second harmonic from CIRESs. The controller of CIRESs can achieve the flexible control objective including the harmonic injection. By adding the 3rd harmonic at the D-axis, a 2nd harmonic and a 4th harmonic could be found at the relay site. Meanwhile, the requirements for the reactive current and the limited current are considered when current command values are computed. After that, the harmonic impedance is computed to reflect the distance of a fault. This is

effective because there is no harmonic current on the remote end. PSCAD simulation and RTDS experiment are done to verify the above two protection schemes.

Related Publications

J2. Z. Yang, W. Liao, Q. Zhang, C. L. Bak, and Z. Chen, "Fault Coordination Control for Converter-interfaced Sources Compatible with Distance Protection during Asymmetrical Faults," in *IEEE Trans. Ind. Electron.*, accepted.

J3. Z. Yang, Q. Zhang, W. Liao, C. L. Bak, and Z. Chen, "Harmonic Injection Based Distance Protection for Line with Converter-interfaced Sources," in *IEEE Trans. Ind. Electron.*, accepted.

CHAPTER 4. NEW METHODS TO ENHANCE THE OPERATION OF DIFFERENTIAL PROTECTION

Distance relays cannot cut off all the faults with no delay, so differential protection often works as the main protection due to its absolute selectivity and high speed. In this chapter, the adaptive problem of proportional restraint differential protection is analyzed, and new solutions are proposed including a control-based method and two new protection algorithms.

4.1. ADAPTIVE ANALYSIS OF DIFFERENTIAL PROTECTION

The fault current angles between both terminals for conventional transmission lines with two-terminal synchronous sources are essentially the same for internal faults but the opposite for external faults. As a result, for internal faults, the operating current in (4.1) will be significantly larger than the restraint current, and the result is the opposite for external faults [69].

$$\begin{cases} I_{\mathrm{op}} \geq k_1 I_{\mathrm{res}} \text{ and } I_{\mathrm{op}} \geq I_{\mathrm{op0}}, \\ I_{\mathrm{op}} = \left|\dot{I}_{\mathrm{S}} + \dot{I}_{\mathrm{W}}\right|, I_{\mathrm{res}} = \left|\dot{I}_{\mathrm{S}} - \dot{I}_{\mathrm{W}}\right| \end{cases} \tag{4.1}$$

where I_{op} stands for the operating current, I_{res} stands for the restraint current, and I_{op0} stands for the starting current. $\dot{I}_{\mathrm{S}}$ and $\dot{I}_{\mathrm{W}}$ stands for the current phasors detected at R_{12} and R_{21}, respectively, and k_1 denotes the restraint coefficient, which is settled at 0.8.

These current phasors will meet the relationship in (4.2) if a BC fault develops at the transmission line [107]:

$$\dot{I}_{\mathrm{WB}} + \dot{I}_{\mathrm{WC}} + \dot{I}_{\mathrm{SB}} + \dot{I}_{\mathrm{SC}} = 0 \tag{4.2}$$

When the controller based on DCC is used, the fault current of CIRESs keeps balanced (only includes the positive-sequence current), so (4.2) can be transformed to (4.3):

$$\dot{I}_{\mathrm{SB}} + \dot{I}_{\mathrm{SC}} = \dot{I}_{\mathrm{WA}} \tag{4.3}$$

Additionally, the angle difference between $\dot{I}_{\mathrm{SB}}$ and $\dot{I}_{\mathrm{SC}}$ will be marginally less than 180° [36]. As a result, when CIRESs are coupled, the current phasor relationship can be drawn in Figure 4-1.

When $\dot{I}_{SC}$ leads that of $\dot{I}_{SB}$ by a certain angle less than 180° in Figure 4-1(a), the angle difference between $\dot{I}_{SC}$ and $\dot{I}_{WC}$ is greater than 90° and less than 120°. In this case, the operating current is smaller than the restraint current for phase C. Additionally, when the phase angle of $\dot{I}_{SC}$ lags that of $\dot{I}_{SB}$ by a certain angle less than 180° in Figure 4-1(b), the angle difference will be greater than 120°, so the sensitivity of differential protection may be declined and even it will fail to be activated.

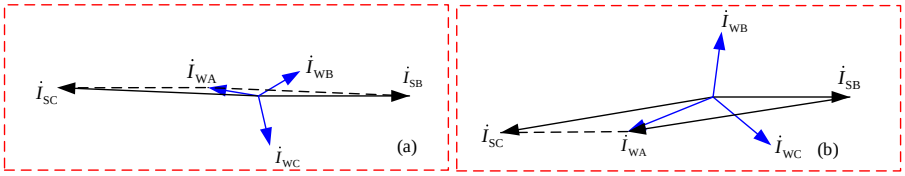

Figure 4-1 Current angle difference between both terminals. Source: C2 [107].

Moreover, a significant zero-sequence fault current is present on both terminals of the transmission line for grounding faults, so the angle difference between the two terminals is drastically minimized. As a result, differential protection can work properly.

In conclusion, traditional differential protection may not operate properly for line-to-line faults but can work for earth faults.

4.2. ACTIVE CONTROL-BASED METHOD

An appropriate fault current angle of CIRESs is discovered to ensure that differential relays can perform properly. After that, the associated current command values are computed considering FRT requirements.

4.2.1. SUITABLE CURRENT ANGLE

The sequence fault network for a BC fault is shown in Figure 4-2 (the system topology is Figure 2-8).

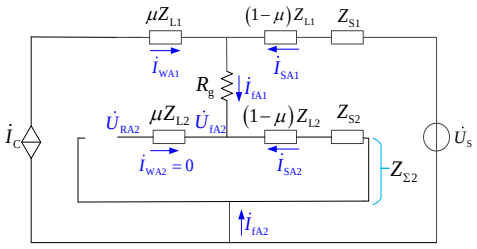

Figure 4-2 Sequence fault network for a BC fault. Source: C2 [107]

The impedances for the grid and the transmission line are denoted by Z_S and Z_L, respectively. The grid is described as a fixed voltage source with a constant impedance, whereas CIRESs are modeled as a regulated current source. Moreover, the fault resistance is denoted by R_g. The following is true in accordance with sequence current boundary conditions for line-to-line faults [107]:

$$\begin{cases} \dot{I}_{fA1} = -\dot{I}_{fA2} \\ \dot{I}_{WA1} + \dot{I}_{SA1} = \dot{I}_{fA1} \end{cases} \tag{4.4}$$

On this basis, Figure 4-3(a) shows the angle relationship among different sequence currents. The angle of $\dot{I}_{SA1}$ will also be equal to that of $\dot{I}_{fA1}$ when the angle of $\dot{I}_{WA1}$ is regulated to be equal to that of $\dot{I}_{fA1}$ according to (4.4). In this case, Figure 4-3(b) shows the phase current angles on two terminals. The angle difference between $\dot{I}_{WB}$ and $\dot{I}_{SB}$ will be equal to that between $\dot{I}_{WC}$ and $\dot{I}_{SC}$, and both will be less than 60°. Under this circumstance, traditional differential protection will function as intended because the operating current is greater than the restraint current for internal faults.

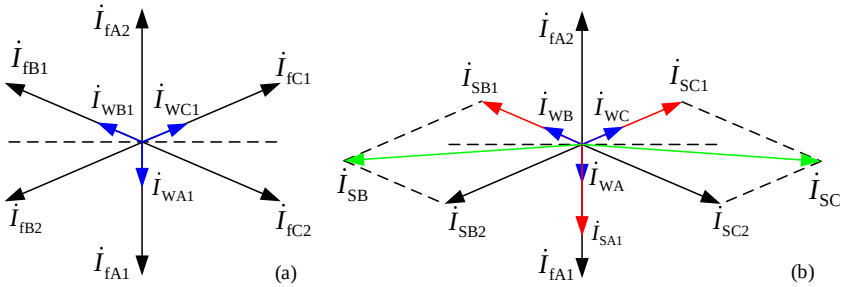

Figure 4-3 The relationship among different currents for line-to-line faults. Source: C2 [107].

Since R_{12} cannot directly measure the phase angle of $\dot{I}_{fA1}$, a scheme to discover this angle must be given. Since CIRESs do not produce any negative-sequence current, (4.5) can result in [107]:

$$\begin{cases} \dot{I}_{SA2} = \dot{I}_{fA2} \\ \dot{U}_{RA2} = \dot{U}_{fA2} = -\dot{I}_{fA2}\left((1-\mu)Z_{L2} + Z_{S2}\right) \end{cases} \tag{4.5}$$

The impedance angle of $(1-\mu)Z_{L2}+Z_{S2}$ can be thought of as a constant number of about 84.29° since the grid impedance angle is stable, so the phase angle of $\dot{I}_{fA2}$ can be computed by $\dot{U}_{RA2}$ with reference to (4.5). As a result, (4.6) can result in:

$$\angle\dot{I}_{SA2} = \angle\dot{U}_{RA2} - \angle\left((1-\mu)Z_{L2} + Z_{S2}\right) + 180^{\circ} \tag{4.6}$$

The necessary phase angle of $\dot{I}_{\mathrm{WA1}}$ in Figure 4-3(a) can then be determined as follows:

$$\angle \dot{I}_{\mathrm{WA1}} = \angle \dot{I}_{\mathrm{fA1}} = \angle \dot{I}_{\mathrm{fA2}} - 180^{\circ} \tag{4.7}$$

It can be found that the control objective in (4.7) is the same as (3.11), so the control strategy in Section 3.2.2 is reasonable to enhance the operations of differential protection besides distance relays.

4.2.2. SIMULATION ANALYSIS

This section will carry out the necessary simulation testing to verify the traditional differential protection issues and the correctness of the suggested approach. The simulation topology is the same as in Figure 2-8. The CIRES power park has a 500 MW nominal capacity and a 40 km long, 220 kV transmission line. Since the grid impedance is settled to 0.4+j12.568 Ω and the line positive-sequence impedance is 0.043+j0.432 Ω/km, the CIRES capacity is equal to one-fourth of the short-circuit capacity of the integrated grid. In addition, the fault time is set to 0.6 s. K1, K2, K3, and K4 are respectively 0%, 50%, and 100% of the line and the output of the next-level line.

A. Adaptive analysis

When a BC fault happened at K1, and the conventional Danish FRT is performed, the related measurements of conventional differential protection are given in Figure 4-4.

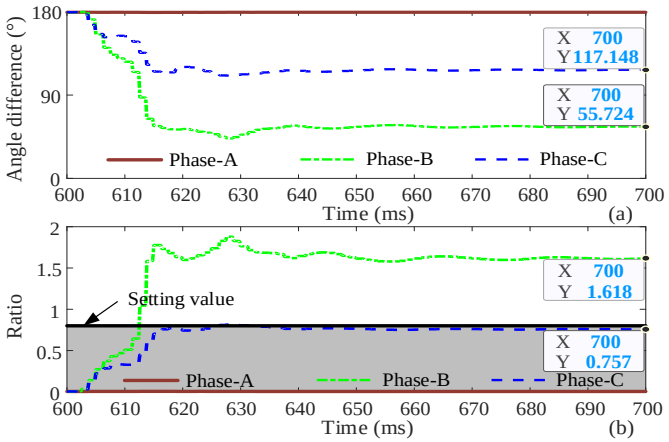

Figure 4-4 Associated measurements of differential protection for Danish FRT strategy. (a) Angle difference, (b) ratio of the operating current to the restraint one. Source: C2 [107].

It can be known in Figure 4-4(a) that the angle difference between both terminals of fault currents is 117.148° for phase C, and 55.724° for phase B. Under this circumstance, the ratio between the operating current and the restraint current will fall below the threshold value for phase C, so the differential relay for phase C would fail to be triggered.

B. Different fault points

To enhance the operations of differential protection, the suggested control scheme is executed under identical fault conditions. At this time, the associated measured quantities are illustrated in Figure 4-5.

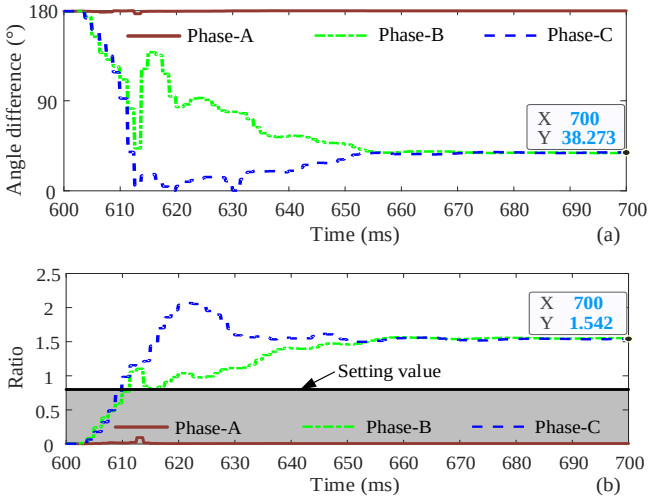

Figure 4-5 Related measured data of differential protection for the given control strategy. (a) Angle difference, (b) ratio of the differential current to the restraint one. Source: C2 [107].

As seen in Figure 4-5(a), the angle differences are roughly equal to 38.273° for phase B and phase C, and both are less than 60°. These results are identical to the findings in Figure 4-3(b). In this case, the ratios between the operating current and the restraint current for phase B and phase C are higher than the setting value, hence differential protection could function as intended.

Table 4-1 provides an overview of the current angle difference and the ratio of the operating current to the restraint current detected by differential relays when BC failures arise at different fault points. All values are derived from 100 ms after the fault inception.

As seen in Table 4-1, the ratios of the operating current to the restraint current are essentially equal for two faulty phases, and these values are greater than the setting

value since the current angular disparity between both terminals is smaller than 60°. Furthermore, the ratio will be less than the setting value for external faults, hence differential protection can keep being blocked. These simulation findings are identical to the theoretical study.

TABLE 4-1 THE RELATED MEASUREMENTS OF DIFFERENTIAL PROTECTION. Source: C2 [107].

Fault location		A	B	C
K1	Difference	179.871	37.987	38.273
	Ratio	0.008	1.551	1.542
K2	Difference	179.867	35.336	35.398
	Ratio	0.008	1.358	1.352
K3	Difference	179.865	32.967	32.869
	Ratio	0.009	1.192	1.191
K4	Difference	179.897	179.567	179.621
	Ratio	0.009	0.004	0.004

4.3. AMPLITUDE RATIO-BASED METHOD

In addition, the fault current of CIRESs is often far less than that from the grid, so a current magnitude ratio-based pilot protection can be suggested.

4.3.1. BASIC PROTECTION PRINCIPLE

The circuit loop can be depicted in Figure 4-6 for a three-phase fault at the transmission line (The system topology is the same as in Figure 2-8). In the figure, CIRESs are modeled as a controlled current source, and the traditional grid is modeled as a voltage source integrated with a constant impedance. λ is the ratio of the line impedance between the fault site and the grid-side relay site to the total line impedance.

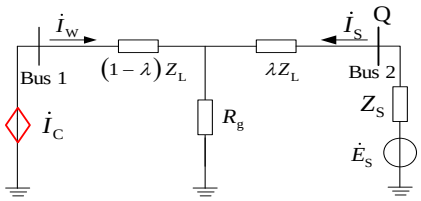

Figure 4-6 The fault circuit for a three-phase fault. Source: C3 [65].

In this situation, the fault currents on both terminals conform to the relationship below [65]:

$$\dot{I}_S\left(\lambda Z_L + Z_S\right) = \dot{E}_S - \left(\dot{I}_W + \dot{I}_S\right)R_g \tag{4.8}$$

After that, the current amplitude ratio between two sides, denoted by ξ, is written as:

$$\xi = \left|\dot{I}_S / \dot{I}_W\right| = \left|\frac{\dot{E}_S / \dot{I}_W - R_g}{\lambda Z_L + Z_S + R_g}\right| \tag{4.9}$$

The fault current from CIRESs is restrained with 1.2 times the nominal current, so the magnitude of E_s/I_w is significantly bigger than R_g and (λZ_L+Z_S+R_g) if R_g is not a large value. In addition, it is also slightly smaller than the load impedance. As a result, ξ is typically greater than 1. When there is no wind or light, CIRESs may not provide the fault current. So as to avoid the invalidation of the protection, the criterion can be revised as:

$$\eta_f = \left|\dot{I}_W / \dot{I}_S\right| < \eta_{set} \tag{4.10}$$

where η_{set} is the setting value of the suggested protection scheme.

$$\begin{cases} \eta_f = \left|\dot{I}_W / \dot{I}_S\right| < \eta_{set}, \eta_1 = \left|\dot{I}_{W1} / \dot{I}_{S1}\right| < \eta_{set} \\ \eta_2 = \left|\dot{I}_{W2} / \dot{I}_{S2}\right| < \eta_{set} \end{cases} \tag{4.11}$$

When one condition of η_f, η_1, and η_2 is achieved, the criterion will be triggered to cut off the fault. For η_f, η_1, and η_2, the setting value can be the same since the considered factors are the same.

4.3.2. PROTECTION SETTING

It is important to think about the impact of the fault current of SGs since the decayed DC component will cause a tiny inaccuracy in the extraction of power frequency components. Additionally, different types of current transducers (CTs) on both terminals will also lead to a difference in measurement accuracy. With reference to these factors, the threshold value can be tuned as [65]:

$$\eta_{set} = 1\text{-}\rho_{rel}\rho_{er}\rho_{st}\rho_{np} \tag{4.12}$$

where ρ_{rel} stands for the reliability factor, which is typically between 1.2 and 1.3. ρ_{er} stands for the error coefficient of CTs, which is typically settled at 1.1. ρ_{st} stands for the same type coefficient, which is 0.5 when the CTs on both ends are the same and 1 when their type is different. ρ_{np} stands for the non-periodic component factor. It is settled to 1 if a fast saturation relay is used, and it can be chosen between 1.5 and 2 if a series resistance is present to remove the unbalanced current [63]. Considering these factors, η_{set} can be taken as 0.82.

The suggested protection lacks the function of phase selection if the sequence current magnitude ratio is utilized, hence it is necessary to add an extra criterion to achieve the phase selection. The particular protection logic diagram is shown in Figure 4-7.

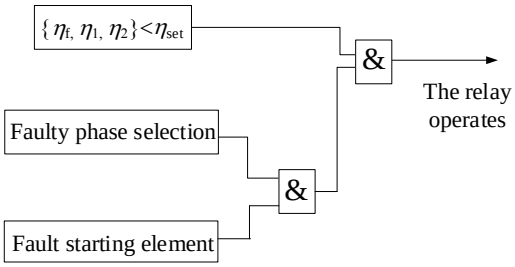

Figure 4-7 The protection logic diagram. Source: C3 [65].

4.3.3. SIMULATION ANALYSIS

In this part, the operations of the suggested protection will be verified. The simulation topology is the same as in Figure 2-8. The nominal capacity of the CIRES power park is set to 500 MW, and the overhead line is 80 km. in addition, the grid equivalent impedance is settled at 0.3+j9.42 Ω, and the positive- and zero-sequence impedances of the transmission line are 0.076+ j0.338 Ω and 0.284+ j0.824 Ω, respectively.

A. Different fault points and fault types

First, Figure 4-8 depicts the simulation results for the phase current magnitude ratio-based criterion for inside-of-zone faults at F2 at 0.6 s. For AG and BC faults in Figure 4-8(a) and (b), η_f for the faulty phase is lower than the setting value, so this method can function as intended. A similar occasion could be seen for ABCG faults in Figure 4-8(d). However, since there is a significant zero-sequence fault current on the CIRES terminal, the phase-C sensitivity for this BCG fault in Figure 4-8(c) is relatively low. To improve the protection sensitivity, positive- and negative-sequence current magnitude ratio-based criteria are therefore required, as shown in Figure 4-9.

Since the most serious scenario should be taken into account in the protection subject, the curve in Figure 4-8 with the poorest sensitivity is used as η_f in Figure 4-9. Aimed at AG and BC faults, η_1 is the largest, and η_2 is the lowest in Figure 4-9(a) and (b) since no negative-sequence fault current is provided from CIRESs. As a result, the sensitivity of η_2 is the highest. Additionally, in Figure 4-9(c), η_f is greater than η_1, indicating that the positive-sequence current ratio-based approach is more sensitive to BCG faults. Since the fault currents on both terminals only include the positive-sequence components for ABCG faults, so η_1 is essentially identical to η_f in Figure 4-9(d). At the same time, η_2 at this point has no significance, so the criteria relied on the

negative-sequence current magnitude ratio ought to be triggered after an unbalanced fault is determined.

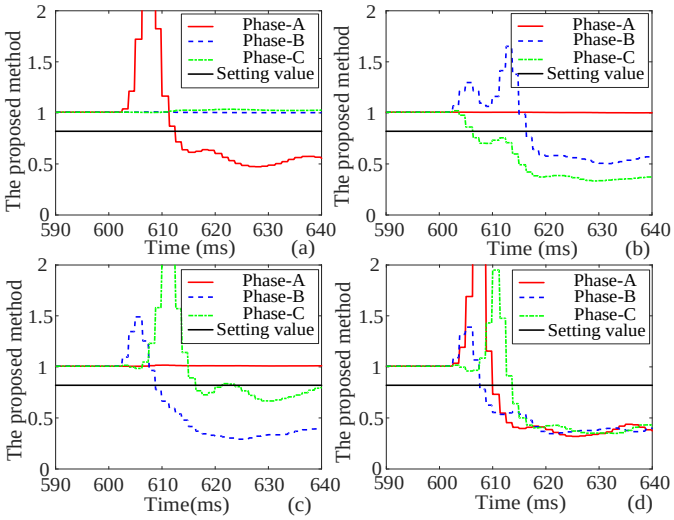

Figure 4-8 The method based on phase current amplitude ratio for inside-of-zone faults. (a) AG, (b) BC, (c) BCG, (c) ABCG. Source: C3 [65].

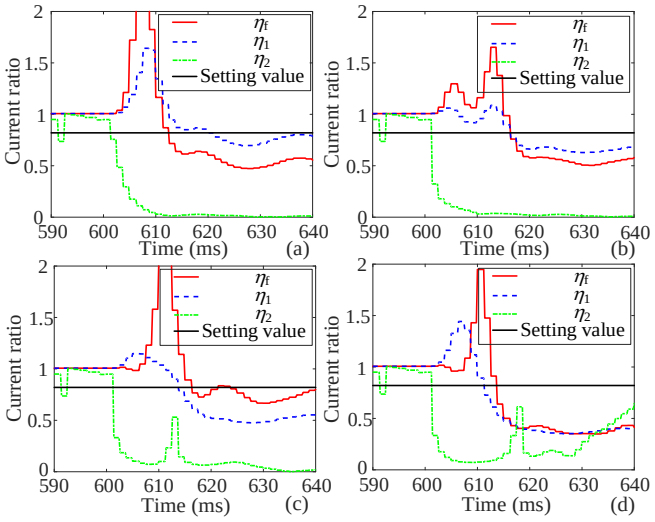

Figure 4-9 The method based on comprehensive current ratio for internal faults. (a) AG, (b) BC, (c) BCG, (c) ABCG. Source: C3 [65].

Additionally, the associated measured quantities of the proposed method are also shown in Figure 4-10 for outside-of-zone faults on the right side of R_{21}. Only the operations of the suggested method are provided for AG and BC faults because the curves for the other fault types are identical.

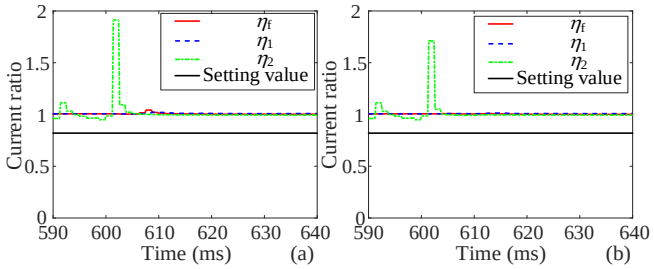

Figure 4-10 Performance for outside-of-zone faults. (a) AG, (b) BC. Source: C3 [65].

As observed in Figure 4-10, the suggested protection scheme will not operate for external faults because η_f, η_1, and η_2 are near 1 at 640 ms and greater than the threshold value under AG and BC failures.

B. Different fault resistances

TABLE 4-2 THE SUGGESTED METHOD UNDER VARIOUS FAULT RESISTANCES. Source: C3 [65].

Fault kind	R_g (Ω)	η_f	η_1	η_2
AG	10	1.210	1.210	0.010
	25	1.740	1.597	0.010
	50	2.728	1.495	0.002
	100	2.766	1.379	0.002
BC	5	0.720	0.844	0.002
	10	0.740	0.907	0.002
	15	0.761	0.976	0.002
	20	0.787	1.050	0.002
BCG	10	1.473	0.749	0.001
	25	1.532	1.198	0
	50	2.041	3.610	0.002
	100	2.350	2.314	0.004
ABCG	10	0.476	0.475	/
	25	0.606	0.605	/
	50	1.411	1.408	/
	100	7.692	7.650	/

The effect of fault resistance will be taken into account in this section. If a fault develops at the exit of R_{12}, the fault current is the smallest on the grid side, therefore the capacity to withstand fault resistance of the suggested method is also at its lowest. Table 4-2 shows the simulation findings for faults at F2 for diverse fault resistances. The maximum fault resistance is settled to 20 Ω for BC faults since the fault resistance for line-to-line faults is the arc resistance. Additionally, 100 Ω is assumed to be the maximum fault resistance for grounding faults. The data at 640 ms is the source of all the values in the table.

Since η_2 in Table 4-2 is substantially smaller than the threshold value for unbalanced faults, η_2 is triggered to cut off the fault even for faults with high fault resistance. In addition, more novel techniques need to be investigated for this fault condition as the suggested scheme can only cover 25 Ω under ABCG failures.

4.4. EUCLIDEAN DISTANCE-BASED METHOD

It is clear that the transient fault current characteristics of CIRESs differ greatly from that of SGs in terms of phase angles, amplitudes, and frequency characteristics. These disparities can be measured using the improved Euclidean distance to detect internal and external faults.

4.4.1. BASIC PROTECTION PRINCIPLE

The Euclidean distance was often applied to measure the spatial distance between two space vectors, $h=\{h_1,h_2,\ldots,h_n\}$ and $g=\{g_1,g_2,\ldots,g_n\}$, and its specific expression is as follows [32]:

$$q=\sqrt{\sum_{i=1}^{n}\left(h_i-g_i\right)^2} \tag{4.13}$$

where q denotes the Euclidean distance, and h_i and g_i denotes any element of the vectors h and g.

h and g are corresponding to current sampling points on two sides inside a time window when the Euclidean distance is applied in the protection field. In order to make it convenient for the protection setting, the Euclidean distance stated in (4.13) is normalized by dividing by the minimal value of the square root of the square sum of two sampling sequences. At this time, it is not possible to obtain a valid calculation result if the current sampling values on one side are equal to 0. To avoid this situation, a constant is added in the denominator as the stability factor, so the improved Euclidean distance is expressed as follows:

$$q_1 = \frac{\sqrt{\sum_{i=1}^{n}\left(|h_i| - |g_i|\right)^2}}{\min\left(\sqrt{\sum_{i=1}^{n} h_i^2}, \sqrt{\sum_{i=1}^{n} g_i^2}\right) + \beta} \tag{4.14}$$

The currents on both terminals of the line are exactly opposite for both normal operation and external faults. Under this circumstance, the improved Euclidean distance q_1 will be zero when all sampling points are treated as their corresponding absolute values. But for inside-of-zone faults, the transient currents between two ends differ significantly, thus q_1 in (4.14) is much larger than 0. Therefore, the protection operation condition is as follows:

$$q_1 > q_{\text{set}} \tag{4.15}$$

where q_{set} denotes the suggested threshold value, which is covered in the next part.

For the time window that is used to compute the Euclidean distance, a long window could increase the stability of the calculation result, but the operating speed will become slow. Considering the trade-off between numerical stability and protection speed, 20 ms is selected as the time window.

Figure 4-11 shows the protection flowchart of the suggested protection scheme. After a low-pass filter is applied to the collected current data between both terminals, the improved Euclidean distance q_1 is computed. The circuit breakers on both terminals will cut off the fault if q_1 is higher than the threshold value; if not, an external fault could be identified. Please note that the suggested scheme is also suitable for the transmission line with DFIGs.

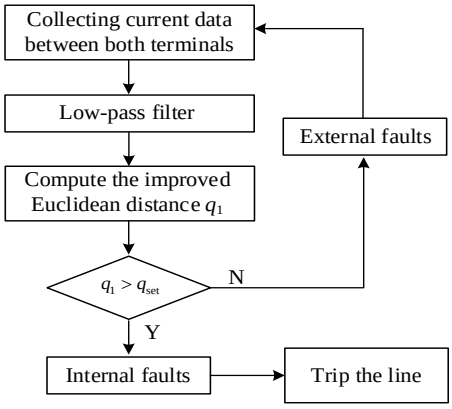

Figure 4-11 The protection flowchart. Source: J4 [32].

4.4.2. PROTECTION SETTING

In the protection tuning, the impact of the angle error, the amplitude error, and the noise is taken into account. It is assumed that the current amplitude error at both terminals is 10%. When the sampling rate is 5 kHz, the angle error due to the sampling delay is lower than 0.9° because the sampling delay between both terminals is often smaller than 5% of the sampling step. The total angle error is finally fixed to 7° because current transformers (CTs) on both sides might also cause a tiny angle error. When fault currents between both terminals contain a 10% error in amplitude and a 7° error in angle, the improved Euclidean distance is displayed in Figure 4-12 when the sampling rate is 5 kHz. Assuming that the current magnitudes between both terminals are 1.1*p* and *p*, respectively.

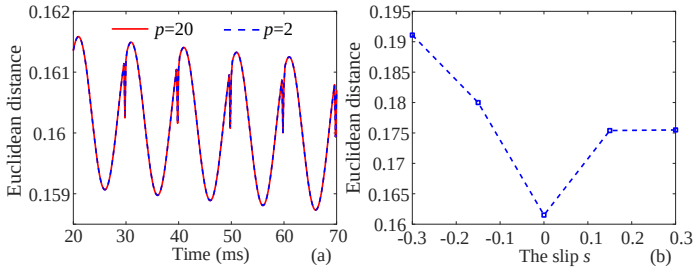

Figure 4-12 Euclidean distance of fault currents with a certain error. (a) different current magnitudes, (b) different slips. Source: J4 [32].

As shown in Figure 4-12 (a), the normalization process ensures that the amplitude *p* has no influence on q_1. When the noise impact and a particular margin are taken into account, the threshold value is settled at 0.3 since the maximum value of q_1 in Figure 4-12 (b) is 0.1911 under various slips.

When the current sampling points are equal to 0 on one side, the stability factor β is attached to the denominator to prevent an invalid result. This issue will occur if the power from RESs is low, or the circuit breaker recloses with a permanent failure. In this case, the protection scheme must guarantee that non-faulty phases can keep being blocked. Given that a line capacitance current is present on the grid side, β ought to be chosen to minimize its impact. The introduction of the stability factor β will decline the sensitivity of the suggested protection scheme for inside-of-zone faults, but the impact is limited since the line capacitance current is very low. The peak value of the capacitance current for non-faulty phases can be expressed as (4.16) when the maximum voltage is considered 1.05 times the nominal voltage [32].

$$I_{\mathrm{Cmax}} = \frac{1.05\sqrt{2}U_N}{\sqrt{3}X_{\mathrm{C}}} \tag{4.16}$$

where X_C denotes the grounding capacitive reactance of the overhead line. After that, the stability factor is obtained as follows:

$$\beta = \frac{k_{rel}}{q_{set}} \sqrt{\sum_{i=1}^{n} \left(I_{Cmax} \sin\left(\omega_0 t_i\right)\right)^2} = \frac{k_{rel}\mu}{q_{set}} \tag{4.17}$$

where k_{rel} denotes a reliability coefficient that ranges from 1.15 to 1.3.

The line capacitance current will not cause the suggested criterion in (4.14) to be activated wrongly when β is set in accordance with (4.17) since q_1 is always lower than q_{set}.

4.4.3. SIMULATION ANALYSIS

In this part, the operations of the suggested protection will be evaluated. The simulation topology is the same as in Figure 2-8. The nominal capacity of the power park is 500 MW, and the grid impedance is equal to 0.4+j12.568 Ω. Moreover, the line length is 40 km. The power sources can be transformed between CIRESs and DFIGs, and all the faults develop at 0.6 s.

A. Time window selection

The time window is respectively settled to 10 ms and 20 ms, to study its impact on the suggested method. Under this circumstance, the improved Euclidean distance is now displayed in Figure 4-13 when a BC fault for DFIGs happens at F4.

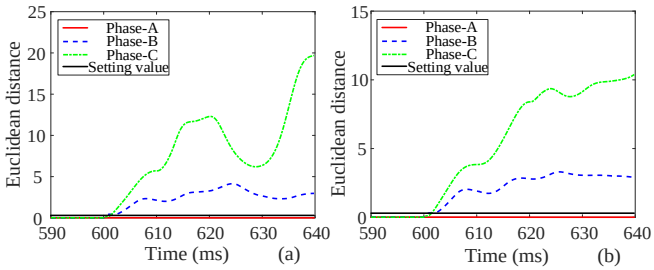

Figure 4-13 Performance under various time windows. (a) 10 ms, (b) 20 ms. Source: J4 [32].

Analyzing the results in Figure 4-13(a) and (b), it can be known that the improved Euclidean distance q_1 will vary within a wide range after the fault while the time window is set to 10 ms. This result is detrimental to the reliability of the suggested scheme. Since the proposed method can operate within 3 ms (1.2 ms for 10 ms of the time window and 2.2 ms for 20 ms of the data window), the reliability is more significant than the operating speed, so 20 ms is chosen as the final value for the time window.

B. Stability factor selection

According to (4-17), β is settled at 0.6. When the system is operating normally and RESs have no output power, Figure 4-14 displays the phase-A fault currents on both terminals and the operation of the suggested technique.

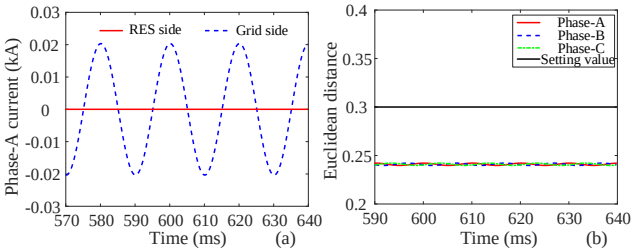

Figure 4-14 Phase-A current and the related Euclidean distance when RESs have no power. (a) Phase-A current waveform, (b) improved Euclidean distance. Source: J4 [32].

It is apparent from Figure 4-14(a) that even though the RES-side fault current is 0 since there is no power provided from CIRESs, the line capacitive current is still present on the grid end. In Figure 4-14(b), q_1 is smaller than the setting value, and this shows that the stability factor could mitigate the impact of the capacitance current.

C. Different fault locations and fault types

Figure 4-15 provides q_1 for external BC faults at F1 and F5.

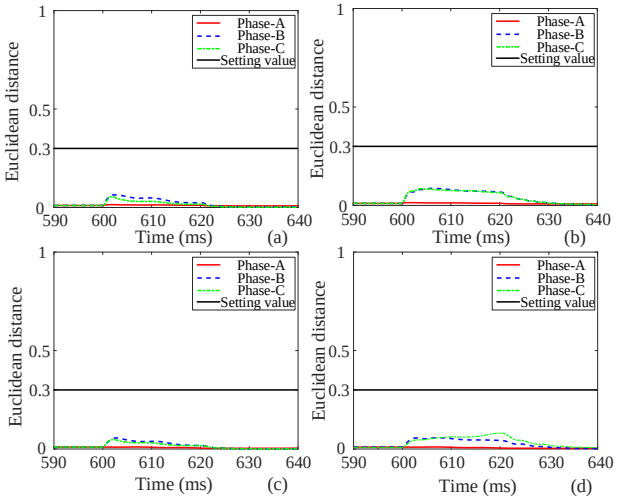

Figure 4-15 The value q_1 for external faults. (a) F1, CIRESs, (b) F5, CIRESs, (c) F1, DFIGs, (d) F5, DFIGs. Source: J4 [32].

In Figure 4-15, the improved Euclidean distance q_1 is always less than the threshold value, making it possible to successfully block the suggested protection.

In addition, the value q_1 is given in Figure 4-16 for AG and BC faults at F3 to assess the operation of the suggested approach for inside-of-zone faults.

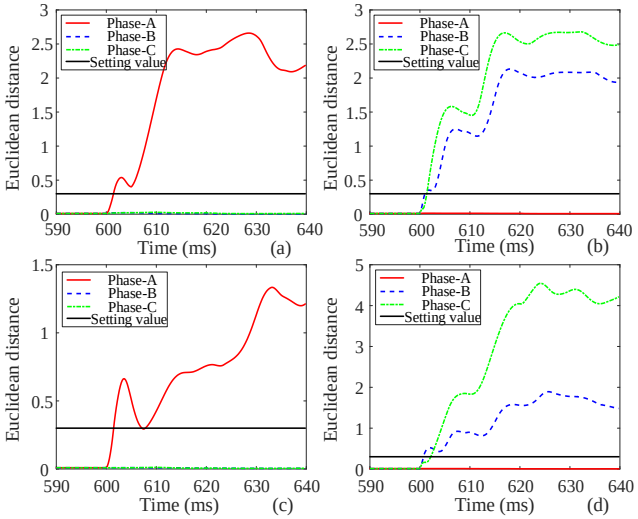

Figure 4-16 The value q_1 for inside-of-zone faults at F3. (a) AG, CIRESs, (b) BC, CIRESs, (c) AG, DFIGs, (d) BC, DFIGs. Source: J4 [32].

As shown in Figure 4-16(a) and (b), q_1 for CIRESs can quickly overtake the threshold value for faulty phases but is smaller than the threshold value for non-faulty phases. Therefore, the proposed approach performs well regardless of whether there are BC faults or AG faults. In addition, the suggested approach can work well for DFIGs according to Figure 4-16(c) and (d).

4.4.4. RTDS VERIFICATION

The suggested protection scheme is validated based on the RTDS experiment platform, too. The improved Euclidean distance is illustrated in Figure 4-17 for the situation when AG and BC failures manifest at F3 at 0 s.

As known in Figure 4-17(a) and (b), the suggested method can function well for AG and BC failures when the source is CIRESs. Similarly, the faulty phases are also detected when the source is DFIGs, and the non-faulty phases are not triggered according to simulation results in Figure 4-17(c) and (d). The protection speed is likewise comparable to the PSCAD simulation findings. These phenomena once more firmly support the suggested protection scheme.

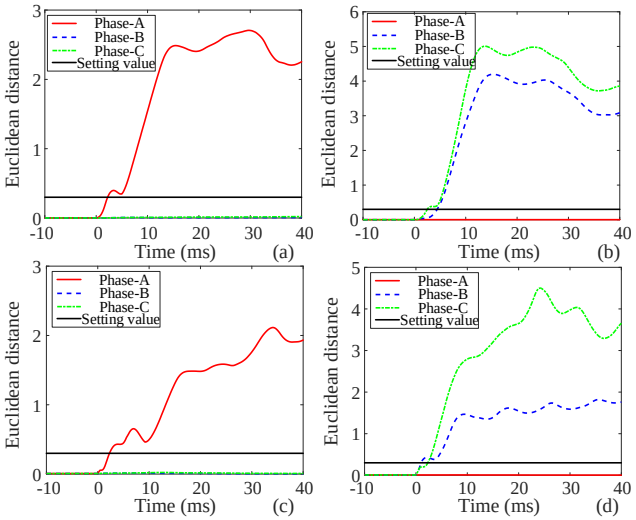

Figure 4-17 The simulation results for internal faults based on the RTDS experiment platform. (a) AG, CIRESs, (b) BC, CIRESs, (c) AG, DFIGs, (d) BC, DFIGs. Source: J4 [32].

4.5. SUMMARY

This chapter analyzed the adaptive problem of traditional proportional restraint differential protection and proposed three novel methods to enhance its performance.

The first method designs a new control strategy to decrease the current angle difference between both terminals by less than 60° for line-to-line faults. As a result, the operating current of differential protection is always larger than the restraint quantity, so conventional differential protection can function as intended.

However, this may be difficult to be performed for protection engineers since fault control strategies of CIRESs are managed by the manufactory. Therefore, a comprehensive current magnitude ratio-based pilot protection is also suggested. The fault current of CIRESs is far lower than that from the connected grid, and this feature can be applied to form a new protection method. This scheme can be suitable for diverse fault points and fault kinds, and it can work well for different fault control strategies.

Following that, an improved Euclidean distance-based pilot protection method is also put forward, which is applicable to both CIRESs and DFIGs. The approach relies on the fact that the fault signatures of RESs are significantly diverse from those of SGs, and the improved Euclidean distance can be utilized to detect this difference. The suggested scheme can function as intended for various fault locations and fault types. In addition, the proposed scheme is also applicable to the case when RESs do not

provide any power, or the circuit breaker recloses with a permanent failure. Moreover, this method uses a 20 ms of data window to compute the improved Euclidean distance, so the extraction of the power frequency phasors is not necessary, which avoids the impact of frequency offset on the suggested method.

Related Publications

J4. Z. Yang, W. Liao, H. Wang, C. L. Bak, and Z. Chen, "Improved Euclidean Distance Based Pilot Protection for Lines with Renewable Energy Sources," in *IEEE Trans. Ind. Informat.*, accepted.

C2. Z. Yang, W. Liao, C. L. Bak, and Z. Chen, "Fault coordination control for converter-interfaced sources compatible with differential protection during asymmetrical faults," *The 5th International Conference on Electrical Engineering and Green Energy (CEEGE)*, Berlin, Germany, 2022.

C3. Z. Yang, W. Liao, C. L. Bak, and Z. Chen, "Comprehensive current amplitude ratio based pilot protection for line with converter-interfaced sources," *2022 The 4th International Conference on Clean Energy and Electrical Systems (CEES 2022)*, Tokyo, Japan, 2022.

CHAPTER 5. THREE-PHASE RECLOSING SCHEME BASED ON ACTIVE CONTROL

In addition, fault nature detection is also important for the resilience of the power system. In this chapter, a fault nature detection scheme relying on active control will be proposed to avoid the secondary impact after the current circuit breaker recloses on a permanent failure. After that, the time sequence for reclosing is also discussed to restore the power supply if a temporary fault is detected.

5.1. FAULT NATURE DETECTION

5.1.1. LOW CURRENT INJECTION

The studied topology is depicted in Figure 5-1(a). Five fault locations, designated K1, K2, K3, K4, and K5, are located at 0%, 25%, 50%, 75%, and 100% of the line away from Bus 1. The circuit breakers BRK2 and BRK3 are deployed on both terminals of the transmission line to cut off the fault. BRK1 is the grid-connected switch of the wind turbine, and back-to-back converters are used to link the wind turbine to the grid, and an LCL filter is placed at the inverter outlet to remove high-order harmonics in Figure 5-1(b). Moreover, a chopper circuit is also equipped on the DC side to impede overvoltage caused by power imbalance during a fault.

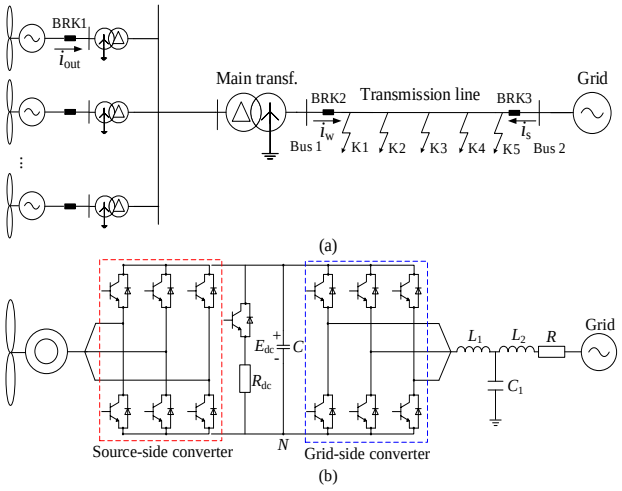

Figure 5-1 The studied system topology. (a) Line, (b) structure of PMSGs. Source: J5.

After BRK1 and BRK2 are reclosed, a low fault current can be measured at the relay site to distinguish a temporary fault or a permanent fault when a novel control scheme is proposed to make the converter interfaced generation system act as a regulated voltage source. By using pulse width modulation (PWM) technologies, the voltage on the inverter outlet can be regulated [93]. Three-phase voltages at the inverter terminal can be stated as (5.1) when the modulation wave is *m* [108].

$$u_{\text{out}} = m \cdot \frac{1}{2} E_{\text{dc}} \tag{5.1}$$

where E_{dc} is the DC bus voltage, and u_{out} is three-phase voltages at the inverter terminal.

The modulation wave is often calculated by the required terminal voltage divided by half of the nominal rate of the DC voltage. However, the DC voltage will fluctuate once a fault appears. During an asymmetric fault, active power will experience a twofold frequency fluctuation because the negative-sequence voltage is a double-frequency component in the rotating positive-sequence DQ frame, as seen in (5.2) [12]:

$$P = P_0 + P_{\text{c2}} \cos\left(2\omega_1 t\right) + P_{\text{s2}} \sin\left(2\omega_1 t\right) \tag{5.2}$$

P_0 stands for the average power, P_{c2} and P_{s2} are the active power's double frequency components, and ω_1 denotes the fundamental frequency angular velocity.

The DC capacitor discharge provides active power on the AC side when the source-side converter is blocked, so (5.3) yields in accordance with the power balance [J5]:

$$C \frac{dE_{\text{dc}}}{dt} = -\frac{P}{E_{\text{dc}}} \tag{5.3}$$

By resolving (5.3), E_{dc} can be written as:

$$E_{\text{dc}} = \sqrt{\frac{1}{C}\left(-2P_0 t + \frac{P_{\text{s2}} \cos 2\omega_1 t - P_{c2} \sin 2\omega_1 t - P_{\text{s2}}}{\omega_1}\right) + E_{\text{dc0}}^2} \tag{5.4}$$

where E_{dc0} denotes the initial value of the DC bus voltage.

It is apparent from (5.4) that the DC voltage E_{dc} gradually decreases with double-frequency oscillations. According to (5.1), u_{out} will have a triple frequency component, which will cause the active power to fluctuate at a quadruple frequency. Accordingly, the DC voltage will fluctuate with a quadruple frequency. In this way,

various harmonic components are produced on DC and AC sides. Therefore, the modulation wave should be calculated by the actual value of the DC voltage instead of the nominal value to remove the effect of the DC voltage variation. Assumed that the required three-phase voltage is u_{cout} (its amplitude is U_{am}), the related modulation wave should be:

$$m_{\mathrm{cout}} = u_{\mathrm{cout}} \Big/ \frac{1}{2} E_{\mathrm{dc}} \tag{5.5}$$

Consequently, the inverter acts as a three-phase voltage source because the DC voltage at the inverter terminal no longer has an impact on the AC voltage according to (5.5). An overcurrent on the faulty phases will be measured at BRK2 for permanent faults after BRK1 and BRK2 have been reclosed. If not, a temporary fault will be detected. As a result, the criterion for a permanent fault is:

$$I_{\varphi} > I_{\mathrm{set}} \tag{5.6}$$

where I_{set} is the threshold value, which will be covered in the following section, and the subscript φ stands for the defective phase.

The combined duration of the protection operation and the circuit breaker opening for 110 kV transmission lines is often estimated to be 200 ms [109]. In addition, the insulation recovery time (arc extinguishing time) is typically 200 to 300 ms and depends on a number of variables, including wind speed, humidity, and arc length [85], [86]. Given these characteristics, 500 ms following the fault is chosen as the time to reclose BRK1 and BRK 2. The period for fault nature determination is set to 40 ms in order to offer enough information to extract the fundamental frequency current.

5.1.2. THRESHOLD VALUE SETTING

There is no load current for temporary faults after the grid-side current circuit breaker is on, so the threshold value can only be settled with the intention of minimizing the influence of the capacitance current on the non-faulty phase. Additionally, the cable line is not taken into consideration because overhead lines are the main type for the high-voltage transmission line. The sequence equivalent loops of phase A, assuming it is the non-faulty phase, are shown in Figure 5-2. In the diagram, X_{C} represents the line capacitive reactance, Z_{L} stands for the equivalent impedance of the transmission line, and Z_{Σ} stands for the total impedance of the main transformer, the collecting line, the step-up transformer, and the LCL filter. The positive and negative-sequence impedances of these elements are identical because they are static elements. Additionally, U_{fA} denotes the voltage at the fault location, E_{V} denotes the effective value of the applied voltage, and U_{RA} is the voltage measured at BRK2 (marked in red point).

The capacitance current can be represented as follows according to Figure 5-2 [J5]:

$$\dot{I}_{\mathrm{c}} = \frac{\dot{U}_{\mathrm{fA1}}}{-\mathrm{j}X_{\mathrm{C1}}} + \frac{\dot{U}_{\mathrm{fA2}}}{-\mathrm{j}X_{\mathrm{C2}}} + \frac{\dot{U}_{\mathrm{fA0}}}{-\mathrm{j}X_{\mathrm{C0}}} \tag{5.7}$$

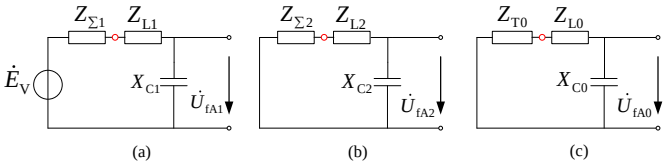

Figure 5-2 Sequence equivalent circuit. (a) Positive-sequence, (b) negative-sequence, (c) zero-sequence. Source: J5.

Additionally, because X_{C0} is often higher than X_{C1} and X_{C2}, the capacitive current conforms to the following relationship:

$$\dot{I}_{\mathrm{c}} < \dot{I}_{\mathrm{Cmax}} = \frac{\dot{U}_{\mathrm{fA}}}{-\mathrm{j}X_{\mathrm{C1}}} \tag{5.8}$$

At the same time, U_{fA} can be regarded as being equal to E_{V} since the current in the non-faulty phase is incredibly low. Therefore, the threshold value can now be set as follows:

$$I_{\mathrm{set}} = k_{\mathrm{rel}} k_{\mathrm{u}} I_{\mathrm{Cmax}} = k_{\mathrm{rel}} \frac{k_{\mathrm{u}} E_{\mathrm{V}}}{X_{\mathrm{C1}}} \tag{5.9}$$

where k_{u} denotes the overvoltage factor from 1.5 to 2, and k_{rel} denotes the reliability factor, which can be selected between 1.2 and 1.5.

5.1.3. THE APPLIED VOLTAGE AMPLITUDE

To protect these electrical devices, U_{am} should not be greater than the nominal voltage, i.e., $U_{\mathrm{am}} \leqslant U_{\mathrm{Nm}}$.

In order to safeguard the converter from overcurrent problems, the current at the inverter terminal cannot overtake the limiting value of the converter. In addition, when CIRESs are regulated as a controlled voltage source, the fault current will have a DC component besides the power frequency component since the inductive current in an AC system cannot vary abruptly. When BRK2 recloses on a permanent fault, the maximum inrush current can now be represented as (5.10) [J5]:

$$i_{\mathrm{M}} = \left(1 + e^{-0.01/T_{\mathrm{a}}}\right) I_{\mathrm{m}} = K_{\mathrm{m}} I_{\mathrm{m}} \tag{5.10}$$

where I_{m} denotes the peak value of the steady-state AC component, T_{a} denotes the decayed time constant of the DC component, and K_{m} denotes the inrush factor that ranges from 1.8 to 1.9 in actual calculations [38].

The maximum AC component I_{V} should meet (5.11) when the inrush current is lower than the current limiting value of the inverter.

$$I_{\mathrm{V}} = \frac{\gamma I_{\mathrm{N}}}{K_{\mathrm{m}}} \tag{5.11}$$

where I_{N} denotes the nominal current, and γ is the inverter's current restraint multiple.

The main transformer's wiring connection is YND, so there is no zero-sequence fault current at the inverter terminal for an unbalanced earth fault at the transmission line. Under this circumstance, the fault current at the inverter terminal is at its maximum for three-phase metallic faults at K1. To compute the applied voltage value, the loop impedance is illustrated when the unlocked turbine number is n_{v}:

$$Z_{\Sigma 1} = \frac{1}{n_{\mathrm{v}}}\left(Z_{\mathrm{FI}} + Z_{\mathrm{step}}\right) + Z_{\mathrm{co}} + Z_{\mathrm{T1}} \tag{5.12}$$

where Z_{step}, Z_{FI}, and Z_{co} are the impedances of the step-up transformer, the LCL filter, and the collection system, and Z_{T1} is the main transformer's positive-sequence impedance.

At this time, the fault current at the inverter outport for three-phase faults is stated as:

$$I_{\max} = \frac{E_{\mathrm{V}}}{n_{\mathrm{v}} \left| Z_{\Sigma 1} \right|} \tag{5.13}$$

Take $I_{\max}$ equal I_{V}, and the related applied voltage amplitude E_{V} is obtained:

$$E_{\mathrm{V}} = I_{\mathrm{V}} \left| Z_{\mathrm{FI}} + Z_{\mathrm{step}} + n_{\mathrm{v}} Z_{\mathrm{co}} + n_{\mathrm{v}} Z_{\mathrm{T1}} \right| \tag{5.14}$$

When $\underline{n}_{\mathrm{v}}$ is equal to 1, E_{V} is considered to be at its minimal value according to (5.14). At this point, under no circumstances will the fault current at the inverter terminal exceed the current limiting setting. The final value of the applied voltage U_{am} will be the smaller value between $\sqrt{2}U_{\mathrm{N}}$ and $\sqrt{2}E_{\mathrm{V}}$.

5.1.4. THE MINIMUM UNLOCKED NUMBER

More unlocked wind turbines (perform the proposed control method) can lower the loop impedance between the inverter outport and the fault location, which is advantageous for fault nature detection due to the increased fault current, as can be seen from (5.12). The minimum unlocked number should be computed with the understanding that the criterion must detect the fault nature reliably for remote high-resistance faults (the worst scenarios). The evaluated largest fault resistance is 100 Ω for grounding faults and 20 Ω for phase-to-phase faults, so four permanent faults at K5 have been studied: an AG fault with 100 Ω of fault resistance, a BC fault with 20 Ω of fault resistance, a BCG fault with 100 Ω of fault resistance, and an ABCG fault with 100 Ω of fault resistance.

1) An AG fault with 100 Ω of fault resistance. The fault current flowing through the BRK2 is as follows [J5]:

$$I_{\min 1}=\frac{3E_{\mathrm{V}}}{\sqrt{\left(2R_{\Sigma 1}+2R_{\mathrm{L1}}+R_{\mathrm{L0}}+3R_{\mathrm{f}}\right)^{2}+\left(2X_{\Sigma 1}+2X_{\mathrm{L1}}+X_{\mathrm{L0}}+X_{\mathrm{T0}}\right)^{2}}} \tag{5.15}$$

When $R_{\Sigma 1}$ is disregarded, the minimum unlocked number of wind turbines can be computed by setting $I_{\min 1}$ equal to I_{set}:

$$n_{\min 1}=\frac{X_{\mathrm{FI}}+X_{\mathrm{step}}}{\frac{1}{2}\sqrt{\frac{9E_{\mathrm{V}}^{2}}{I_{\mathrm{set}}^{2}}-\left(2R_{\mathrm{L1}}+R_{\mathrm{L0}}+3R_{\mathrm{f}}\right)^{2}}-X_{\mathrm{L1}}-\frac{1}{2}X_{\mathrm{L0}}-\frac{1}{2}X_{\mathrm{T0}}-X_{\mathrm{CO}}-X_{\mathrm{T1}}} \tag{5.16}$$

2) A BC fault with 20 Ω of fault resistance. The fault current measured at BRK2 is displayed as follows:

$$I_{\min 2}=\sqrt{3}\frac{E_{\mathrm{V}}}{\sqrt{\left(2R_{\Sigma 1}+2R_{\mathrm{L1}}+R_{\mathrm{f}}\right)^{2}+\left(2X_{\Sigma 1}+2X_{\mathrm{L1}}\right)^{2}}} \tag{5.17}$$

After that, the smallest unlocked number can be calculated by setting $I_{\min 2}$ equal to I_{set}:

$$n_{\min 2}=\frac{X_{\mathrm{FI}}+X_{\mathrm{step}}}{\frac{1}{2}\sqrt{\frac{3E_{\mathrm{V}}^{2}}{I_{\mathrm{set}}^{2}}-\left(2R_{\mathrm{L1}}+R_{\mathrm{f}}\right)^{2}}-X_{\mathrm{L1}}-X_{\mathrm{CO}}-X_{\mathrm{T1}}} \tag{5.18}$$

3) A BCG fault with 100 Ω of fault resistance. The phase-B and phase-C fault currents measured at BRK2 can be expressed as:

$$\dot{I}_{\mathrm{fb}} = \dot{I}_{\mathrm{fa(1)}}\left(\alpha^2 - \frac{Z_{\Sigma 2} + Z_{\mathrm{L}2} + \alpha\left(Z_{\mathrm{T}0} + Z_{\mathrm{L}0} + 3R_{\mathrm{f}}\right)}{Z_{\Sigma 2} + Z_{\mathrm{L}2} + Z_{\mathrm{T}0} + Z_{\mathrm{L}0} + 3R_{\mathrm{f}}}\right) \tag{5.19}$$

$$\dot{I}_{\mathrm{fc}} = \dot{I}_{\mathrm{fa(1)}}\left(\alpha - \frac{Z_{\Sigma 2} + Z_{\mathrm{L}2} + \alpha^2\left(Z_{\mathrm{T}0} + Z_{\mathrm{L}0} + 3R_{\mathrm{f}}\right)}{Z_{\Sigma 2} + Z_{\mathrm{L}2} + Z_{\mathrm{T}0} + Z_{\mathrm{L}0} + 3R_{\mathrm{f}}}\right) \tag{5.20}$$

where $I_{\mathrm{fa(1)}}$ is equal to:

$$\dot{I}_{\mathrm{fa(1)}} = \frac{\dot{E}_{\mathrm{V}}}{Z_{\Sigma 1} + Z_{\mathrm{L}1} + \dfrac{\left(Z_{\Sigma 2} + Z_{\mathrm{L}2}\right)\left(Z_{\mathrm{T}0} + Z_{\mathrm{L}0} + 3R_{\mathrm{f}}\right)}{Z_{\Sigma 2} + Z_{\mathrm{L}2} + Z_{\mathrm{T}0} + Z_{\mathrm{L}0} + 3R_{\mathrm{f}}}} \tag{5.21}$$

The minimal unlocked number n_{min3} is calculated using a searching approach because it is difficult to take the modulus of $\dot{I}_{\mathrm{fbmin}}$ and $\dot{I}_{\mathrm{fcmin}}$. These are the detailed steps:

① Set n_{v} equal to 1, the fault currents for phase B and phase C are computed by (5.19), (5.20), and (5.21).

② Increase n_{v} until I_{fb} and I_{fc} are both greater than I_{set}. In this way, n_{min3} can be computed.

4) An ABCG fault with 100 Ω of fault resistance. In this case, the fault current measured at BRK2 is computed as follows:

$$I_{\mathrm{min}\,4} = \frac{E_{\mathrm{V}}}{\sqrt{\left(R_{\Sigma 1} + R_{\mathrm{L}1} + R_{\mathrm{f}}\right)^2 + \left(X_{\Sigma 1} + X_{\mathrm{L}1}\right)^2}} \tag{5.22}$$

If we set I_{min4} equal to I_{set}, the smallest unlocked number can yield:

$$n_{\mathrm{min}\,4} = \frac{X_{\mathrm{FI}} + X_{\mathrm{step}}}{\sqrt{\dfrac{E_{\mathrm{V}}^2}{I_{\mathrm{set}}^2} - \left(R_{\mathrm{L}1} + R_{\mathrm{f}}\right)^2} - X_{\mathrm{L}1} - X_{\mathrm{CO}} - X_{\mathrm{T}1}} \tag{5.23}$$

The ultimate minimum unlocked number of wind turbines is (5.24) to guarantee that the suggested criterion can recognize all the defective phases in any situation.

$$n_{\mathrm{min}} = \begin{cases} \mathrm{round}\left(n_{\mathrm{p}}\right), \mathit{if}\ n_{\mathrm{p}} \le \mathrm{round}\left(n_{\mathrm{p}}\right) \\ \mathrm{round}\left(n_{\mathrm{p}}\right) + 1, \mathit{if}\ n_{\mathrm{p}} > \mathrm{round}\left(n_{\mathrm{p}}\right) \end{cases} \tag{5.24}$$

where round () denotes the rounding function, and n_{p} is equal to:

$$n_{\mathrm{p}} = \max\left(n_{\min 1}, n_{\min 2}, n_{\min 3}, n_{\min 4}\right) \tag{5.25}$$

where max () denotes the maximum value function.

By this process, the minimum unlocked number of wind turbines is computed to detect the fault property reliably.

5.2. FAST MATRIX PENCIL EXTRACTION METHOD

The charging and discharging process between the line inductance and the line capacitance will produce the inter-harmonic after reclosing BRK1 and BRK2. In addition, the fault current will also include the decayed DC component to ensure waveform continuity. These components will compromise the accuracy of the conventional fast Fourier transform (FFT) algorithm. To extract accurate power frequency phasors, a fast matrix pencil extraction (FMPE) approach is used [110]. The following are the detailed steps of this algorithm:

1) Assumed that the initial signal, y(t), is composed of a finite number of attenuated cosines [J5]:

$$y(t) = \sum_{n=1}^{p} A_n e^{\lambda_n t} \cos\left(2\pi f_n t + \varphi_n\right) \tag{5.26}$$

where A_{n} denotes the amplitude of the n-th order, p denotes the number of sub-signals, λ_{n} denotes the attenuation coefficient that is smaller than 0, φ_{n} represents the initial phase angle of differential signals, and f_{n} represents the frequency of every sub-signal.

2) After a low-pass filter is applied to $y(t)$, the filtered signal is sampled at 5 kHz. The matrix Y below is built using the data within one cycle (100 consecutive sampling points):

$$Y = \begin{bmatrix} y(1) & y(2) & \cdots & y(60) \\ y(2) & y(3) & \cdots & y(61) \\ \vdots & \vdots & & \vdots \\ y(41) & y(82) & \cdots & y(100) \end{bmatrix}_{41\times 60} \tag{5.27}$$

3) A reference signal with the formula $s(t)=\cos(2f_0 t)$ is constructed, where f_0 is the fundamental frequency. The next step is to repeat step 2) to create a new sampling matrix $\boldsymbol{S}$:

$$S = \begin{bmatrix} s(1) & s(2) & \cdots & s(60) \\ s(2) & s(3) & \cdots & s(61) \\ \vdots & \vdots & & \vdots \\ s(41) & s(82) & \cdots & s(100) \end{bmatrix}_{41\times 60} \tag{5.28}$$

4) The Moore-Penrose pseudoinverse of matrix $\boldsymbol{Y}$ is designated as $\boldsymbol{Y}^{+}$, and it is right multiplied by the matrix $\boldsymbol{S}$ to produce the matrix $\boldsymbol{A}$, that is, $\boldsymbol{A}=\boldsymbol{S}\boldsymbol{Y}^{+}$. Then, matrix $\boldsymbol{A}$ is subjected to QR decomposition to generate an orthogonal matrix $\boldsymbol{Q}$ and an upper triangular matrix $\boldsymbol{R}$. Additionally, the matrix $\boldsymbol{R}$ can be expressed as the singular product form of the upper triangular full-rank matrix $\boldsymbol{W}$ and the diagonal matrix $\boldsymbol{\Lambda}$, i.e., $\boldsymbol{R}=\boldsymbol{\Lambda}\boldsymbol{W}$.

5) A similar transformation is done for matrix $\boldsymbol{A}$ to yield matrix $\boldsymbol{B}$, i.e., $\boldsymbol{B}=\boldsymbol{W}\boldsymbol{Q}\boldsymbol{\Lambda}$, and its second-order principal minor is designated as matrix $\boldsymbol{C}$. Thus, the characteristic roots of matrix $\boldsymbol{C}$ are precisely the two non-zero characteristic roots of matrix $\boldsymbol{B}$, as well as a pair of conjugate complex eigenvalues corresponding to frequency f_0:

$$\lambda_{1,2} = a \pm \mathrm{j}b \tag{5.29}$$

After that, the power frequency current amplitude A_1 in (5.26) can be expressed as (5.30):

$$A_1 = \frac{1}{|\lambda_1|} = \frac{1}{|\lambda_2|} \tag{5.30}$$

In this way, the power frequency current amplitude can be successfully extracted to identify the fault property. Only the measured value after 20 ms at the beginning of detection can be used for the fault nature detection because this technique needs one cycle of the data window.

5.3. TIME SEQUENCE FOR RECLOSING

When the conventional three-phase reclosing technique is reclosed, BRK3 is reclosed first after the insulating capacity at the fault location has been recovered. And then, BRK1 and BRK2 are reclosed to recover the power supply. Figure 5-3 depicts the detailed time sequence diagram for this traditional reclosing. The time sequences on both sides are different because the circuit breakers on both sides may be triggered by various relays with various time delays. In the diagram, t_{pr} stands for protection operation time, t_{QF} stands for the circuit breaker's opening time, t_u stands for the arc extinguishing time at the fault location, and t_{ARD} stands for a time delay before reclosing for the circuit breaker that trips first (assuming BRK3).

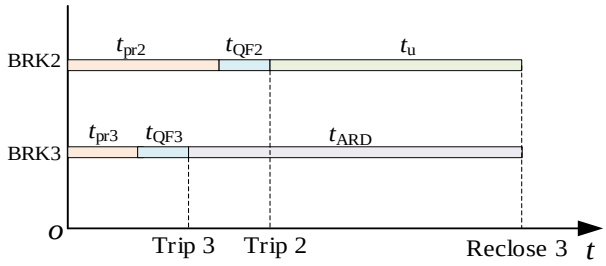

Figure 5-3 The time sequence of the conventional reclosing method. Source: J5.

When a fault occurs, PMSGs will perform the FRT strategy to raise the grid voltage. After BRK2 and BRK3 trip, the FRT control will be stopped because of the open circuit. Before detecting, the suggested voltage control scheme will be executed to make PMSGs act as a three-phase voltage source. After 500 ms following the fault, BRK1 and BRK2 are reclosed. When BRK2 detects an overcurrent, BRK2 is turned off once more, and the inverter is once more blocked. For permanent faults, the secondary impact will be lessened because the fault current provided by PMSGs is far lower than that from the grid. If there is no overcurrent, a temporary fault will be detected. At this time, the inverter will be blocked after 40 ms, and BRK3 will be reclosed. After that, the conventional control mechanism will be restarted, and the power supply will be progressively restored. Figure 5-4 illustrates the specific time sequence diagram for the proposed scheme. In this diagram, the term "Re" stands for reclosing the associated circuit breaker, and t_j stands for the detection time. Only a short detection time of 40 ms is added compared to the conventional time sequence diagram, thus t_{ARD} for BRK3 is extended by the same 40 ms.

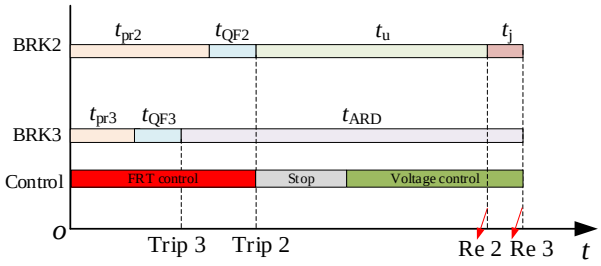

Figure 5-4 The time sequence of the suggested scheme. Source: J5.

5.4. SIMULATION VERIFICATION

The suggested approach will be tested considering diverse fault conditions. The nominal capacity of the wind farm is 100 MW with a unit capacity of 1.5 MW. The length of the transmission line is 80 km with a voltage level of 110 kV. The fault time is 0.6 s, the voltage regulation mode will work at 1.1 s, and the persisting period is 40

ms. In addition, with reference to the line capacitance parameter, I_{set} is settled to 0.0178 kA.

5.4.1. PSCAD SIMULATION

A. Minimum unlocked number

First, in order to guarantee that the fault currents at the inverter terminal do not exceed the current restraint value of the inverter, the applied voltage is estimated as 0.2245 kV in accordance with (5.17). The minimum unlocked number is thus determined to be 4 in accordance with (5.25) to lessen damage to wind turbines under permanent faults and guarantee that the faulty phases can be reliably recognized. Figure 5-5 shows the fault current at the inverter terminal during various permanent metallic faults at K1.

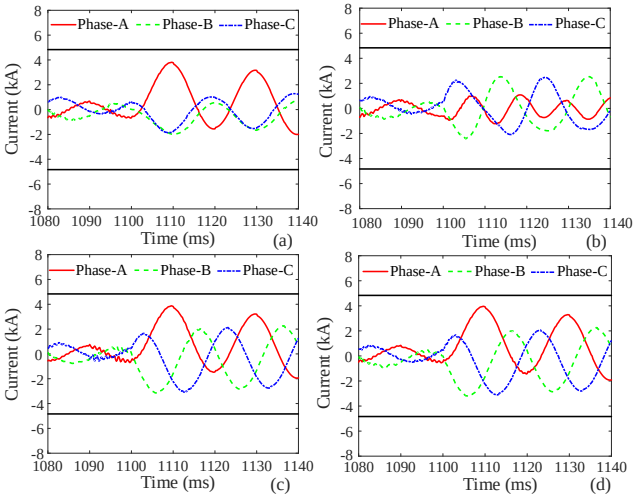

Figure 5-5 The fault current at the inverter outport for various fault types. (a) AG, (b) BC, (c) BCG, (d) ABCG. Source: J5.

The highest permitted fault current peak value is 4.835 kA when the current limiting value of the inverter is set to 1.5 p.u. for 1.5 MW of single unit capacity. Under this circumstance, the inverter will not be damaged by overcurrent since three-phase fault currents at the inverter outport in Figure 5-5 are always lower than the current restraint value for various fault types. The fault loop's positive- and negative-sequence impedances are far greater than its zero-sequence impedance, which results in a relatively tiny negative-sequence current for BCG faults. Additionally, since the inverter terminal is on the low-voltage side of the step-up transformer, there is no zero-sequence component, and three-phase currents detected at the inverter terminal are very similar for BCG and ABCG faults.

B. Remote faults with high resistance

Four of the worst fault scenarios are simulated to evaluate the operation of the suggested technique for remote faults with high resistance. When these permanent faults arise, the current amplitudes measured at BRK2 can be seen in Figure 5-6.

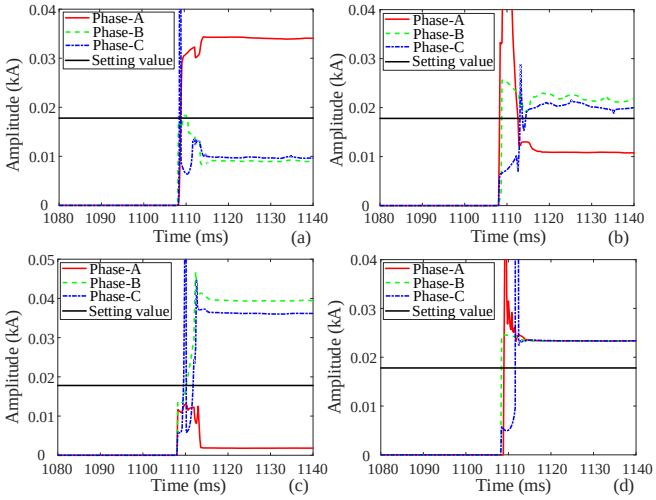

Figure 5-6 The fault current for remote permanent faults with high resistance. (a) AG, (b) BC, (c) BCG, (d) ABCG. Source: J5.

The suggested detection approach can reliably determine the fault nature and fault kinds, as can be shown in Figure 5-6, the currents on the faulty phases are higher than the threshold value and the currents on the non-faulty phases are lower than the threshold value. Three-phase fault currents for ABCG faults in Figure 5-6(d) are 0.0233 kA. For a BC fault with 20 Ω of fault resistance in Figure 5-6(b), the sensitivity is at the lowest. The phase-B current in this case is 0.0218 kA, and the phase-C current is 0.0200 kA.

C. Different unlocked numbers

In this part, the effectiveness of the suggested scheme will be assessed under various unlocked numbers of wind turbines. The fault conditions are identical to those displayed in the last section. In this case, Table 5-1 shows the measured fault current, with all values measured at 1140 ms.

When more wind turbines are unlocked at the same applied voltage, the fault current in Table 5-1 will be increased since this is equal to a reduction in the impedance of the fault circuit. As a result, the sensitivity of the suggested criterion is effectively enhanced by the more unlocked number.

TABLE 5-1 AMPLITUDE UNDER DIFFERENT WIND TURBINE NUMBERS. Source: J5.

Unlocked number	Fault types	Resistance (Ω)	Phase-A (kA)	Phase-B (kA)	Phase-C (kA)
4	AG	100	**0.0341**	0.0090	0.0096
	BC	20	0.0108	**0.0218**	**0.0200**
	BCG	100	0.0018	**0.0394**	**0.0362**
	ABCG	100	**0.0233**	**0.0233**	**0.0233**
20	AG	100	**0.1376**	0.0076	0.0010
	BC	20	0.0099	**0.0955**	**0.0940**
	BCG	100	0.0058	**0.1508**	**0.1154**
	ABCG	100	**0.1040**	**0.1041**	**0.1040**
40	AG	100	**0.2116**	0.0076	0.0103
	BC	20	0.0099	**0.1742**	**0.1726**
	BCG	100	0.0076	**0.2257**	**0.1723**
	ABCG	100	**0.1769**	**0.1769**	**0.1770**
50	AG	100	**0.2350**	0.0077	0.0104
	BC	20	0.0098	**0.2095**	**0.2079**
	BCG	100	0.0080	**0.2492**	**0.1942**
	ABCG	100	**0.2050**	**0.2044**	**0.2040**
66	AG	100	**0.2629**	0.0080	0.0104
	BC	20	0.0096	**0.2597**	**0.2577**
	BCG	100	0.0085	**0.2760**	**0.2254**
	ABCG	100	**0.2388**	**0.2389**	**0.2391**

D. Comparison with the FFT algorithm

The FMPE method is employed in place of the conventional FFT approach to extract fundamental frequency phasors, and a comparison is made to show off its benefits. When the unlocked wind turbine number is set to 4 and an AG failure with a 100 Ω fault resistance and a BC failure with a 20 Ω fault resistance arise at K5, three-phase currents, and the extracted fundamental-frequency phasors are illustrated in Figure 5-7.

Figures 5-7(a) and (b) show that the current on the non-faulty phase will include inter-harmonic, and the current on the faulty phase will have a decayed DC component, so the fault current amplitude obtained by the FFT approach is currently unstable. When using FFT, phase B and phase C, particularly in Figure 5-7(c), may be mistaken for the defective phases. The FMPE approach is therefore superior for the scenario under study since it can precisely extract fundamental frequency phasors from complex low-frequency harmonics.

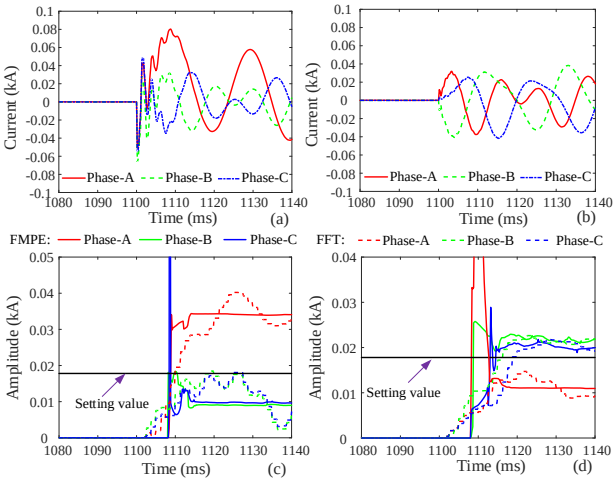

Figure 5-7 The current waveforms and the extracted phasors under FFT and FMPE. (a) current for AG, (b) current for BC, (c) amplitude for AG, (d) amplitude for BC. Source: J5.

5.4.2. RTDS VERIFICATION

The suggested approach is also validated by the RTDS experiment platform. The fault currents measured at BRK2 are displayed in Figure 5-8 when various remote high-resistance faults developed at K5.

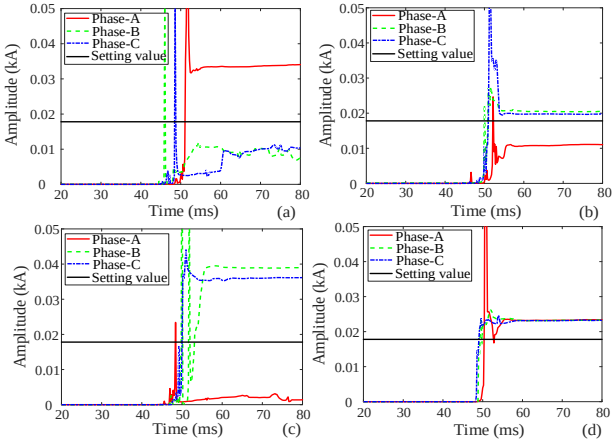

Figure 5-8 The overcurrent for remote high-resistance faults based on the RTDS platform. (a) AG, (b) BC, (c) BCG, (d) ABCG. Source: J5.

The currents on the faulty phases will be greater than the setting value under various remote high-resistance faults, as displayed in Figure 5-8. The fault current in Figure

5-8(d) for ABCG faults is 0.0233 kA, which is identical to the PSCAD simulation result. For other faults, comparable circumstances can be also observed. Figure 5-9 further displays the effectiveness of the suggested scheme for temporary faults.

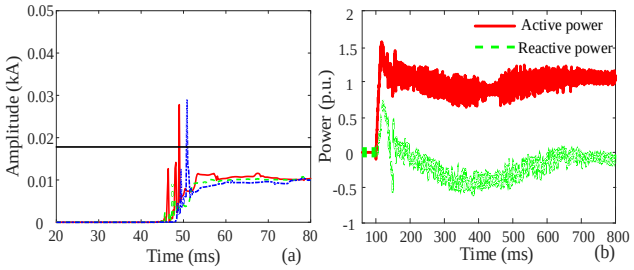

Figure 5-9 The detected fault current and the restored power based on RTDS. (a) The fault current, (b) the restored power. Source: J5.

The data after 60 ms are convinced since the fault detection starting time is assumed to be 40 ms. A temporary fault can be detected since the observed currents in Figure 5-9 (a) are always lower than the threshold value after 60 ms. The output power from the wind farm in Figure 5-9 (b) will then be restored after a period of fluctuation when BRK3 is then reclosed. These results from PSCAD and RTDS support the proposed method once more.

5.5. SUMMARY

By adjusting the voltage modulation wave, the inverter is regulated as a controllable three-phase voltage source. Based on this, it is feasible to reveal the fault property by detecting the overcurrent at the relay point.

To increase the accuracy of the extraction in a complicated harmonic environment, power frequency phasors are extracted using an FMPE method. The fault current flowing through the inverter cannot exceed its current limiting value, this point is considered to determine the magnitude of the applied voltage. Additionally, the minimum unlocked number of PMSGs is computed to make sure that this suggested technique still works for remote faults with high fault resistance. Even though the circuit breaker recloses on permanent faults, the secondary impact is relatively minimal because the fault current generated by wind turbines is much lower than that from the grid. The suggested criterion can be applied for various fault types and fault locations without the second injection, and these features are verified by both PSCAD simulation and RTDS experiment.

Related Publications

J5. Z. Yang, W. Liao, C. L. Bak, and Z. Chen, "Active control Based Three-phase Reclosing Scheme for Single Transmission Line with PMSGs," in *IEEE Trans. Ind. Electron.*, submitted.

CHAPTER 6. CONCLUSIONS

6.1. SUMMARY

This Ph.D. thesis was focused on the advanced control strategies of CIRESs to enhance the operations of the protection system on the outgoing transmission line including directional elements, distance relays, differential protection, and auto-reclosing. In addition, two new protection algorithms are also introduced briefly to enhance the performance of the differential relay. In this thesis, the challenges caused by the RES integration are clarified, and the corresponding solutions are given, and they can be summarized as follows:

In Chapter 1, the impact of the CIRESs on the protection system and the existing solutions have been reviewed. The advantages and limitations of these methods are also clarified. Though these methods are effective to improve the operations of protective relays, their applications on an actual power system need a lot of investment since all the protection devices near the CIRES power plant are necessary to be updated. Therefore, more protection methods should be proposed, especially methods based on active control.

In Chapter 2, the fault current expressions during the transient process and steady state are derived, and the study shows that the fault current of CIRESs will be controlled by current command values during the steady state. After that, a new control strategy is developed to make directional elements operate correctly based on the derived fault current and the basic protection principle. Meanwhile, the fault current can reach the maximum allowable value of the inverter, so the short capacity of CIRESs is fully utilized. Therefore, the impact of the CIRES integration on directional elements can be avoided.

In Chapter 3, two control methods are designed to enhance the performance of distance relays. In the first method, a novel fault control scheme is suggested to adjust the power frequency current to make the angle of the additional impedance equal to 0°. In this way, the apparent reactance measured at the relay point is equal to the line replica reactance, so the fault distance could be measured correctly. Meanwhile, the reactive current injection in the grid code can be satisfied in most cases. For some occasions where the fault current from CIRESs overtakes the current restraint value, the injected reactive current needs to be scaled down to meet the current limiting condition. In addition, the apparent impedance still includes a large resistive part, so the quadrilateral protection zone with a big resistive reach needs to be applied. In order to overcome this shortcoming, another method is proposed based on harmonic injection. A 2^{nd} harmonic current is provided from the inverter by adding a 3^{rd} order signal on the D-axis. As the PI controller cannot follow the AC reference signal accurately, the actual response is derived by the transfer function method. After that,

the measured harmonic impedance can work properly for internal faults since the remote infeed is disappeared. Meanwhile, the current restraint and the reactive current injection requirements in the grid code are also satisfied.

As for Chapter 4, it is proved that the control method in the first method of Chapter 3 is effective to reduce the phase angle difference of the faulty phase to be less than 60° when a line-to-line fault arises at the transmission line. Therefore, the sensitivity of differential protection can be improved a lot. In addition, two novel pilot protection approaches are suggested to replace traditional proportional restraint differential protection. For the first method, the current amplitude difference is utilized to establish a new protection scheme since the fault current of CIRESs is far lower than that from the power grid. This method is easily applied in the power system since only a small revision needs to be done for traditional differential protection. For the second method, the improved Euclidean distance is applied to detect the time-domain current waveform disparity, so it is not necessary to extract the power frequency phasors, which avoids the impact of frequency offset. In this way, this method is applicable to DFIGs and CIRESs.

In Chapter 5, a new three-phase reclosing method is proposed based on active control to reduce the strong secondary impact after the circuit breaker recloses on a permanent failure. The inverter of CIRESs is regulated as a voltage source, and a low overcurrent can be detected for permanent faults. Reversely, a temporary fault can be identified if there is no overcurrent. Since the produced overcurrent for permanent faults is much smaller compared with the inrush current from the grid, it is effective to reduce the severe secondary impact. In addition, all the faulty phases can also be identified reliably. Moreover, the suggested reclosing method can work properly for remote faults with high fault resistance.

6.2. MAIN CONTRIBUTIONS

The main findings of this Ph.D. thesis could be concluded below:

- **Control strategy for the correct operation of directional elements**

  A fault control strategy is designed to ensure the compatibility of CIRESs with line directional elements on the transmission line. Meanwhile, the short-circuit capacity of CIRESs is fully utilized by an iterative algorithm. The developed control technique can behave properly for various fault types, fault locations, and high-resistance faults.

- **New methods to enhance the operation of distance relays**

In order to improve the performance of distance relays, two new methods based on active control are proposed, and their advantages could be summarized:

1) The fault control strategy is designed to enhance the operation of distance relays while FRT conditions including reactive current injection and fault current restraint are satisfied.

2) The method based on the harmonic injection can reduce the big resistive part contained in the apparent impedance compared with the first method.

3) Two methods can function as intended for diverse fault locations, fault types, and high resistance faults.

- **New methods to enhance the operations of differential protection**

Three novel methods are proposed to enhance the operation of conventional differential protection, and the main advantages are as follows:

1) For the first method, a new control strategy is developed to reduce the current angle disparity between both terminals for line-to-line faults, so the impact of the CIRES integration on traditional differential protection can be avoided.

2) A comprehensive current magnitude ratio-based pilot protection is suggested as the second method. The suggested approach could be easily applied in the real power system since only small revisions are done for traditional differential protection.

3) Finally, an improved Euclidean distance-based pilot protection method is suggested. This approach takes advantage of the transient current characteristics, so it could be applied to diverse power sources and FRT strategies.

- **Active control-based three-phase reclosing scheme**

A new three-phase reclosing scheme is developed to reduce the secondary impact caused by reclosing on permanent faults. After the inverter is regulated as a three-phase voltage source, the fault property could be identified by detecting the overcurrent. The injected overcurrent is very small compared with the situation where the grid-side circuit breaker recloses on a permanent fault. Meanwhile, the suggested method is effective for remote high-resistance faults.

6.3. RESEARCH PERSPECTIVES

Fault control strategies have been developed for the correct operation of protective relays including directional elements, distance relays, differential relays, and the reclosing scheme. In addition, two new pilot protection schemes are also suggested. However, some problems still need to be resolved, as illustrated in the following:

- Since the controller can only achieve the limited control objectives, some traditional FRT requirements are difficult to be satisfied when the correct operation of protective relays works as the control goal.

- The typical controller needs tens of milliseconds to correctly track the new current references after the fault inception, and then protective relays can operate, so the operating speed of protective relays will be slower than the common value of about 20 to 30 ms. Therefore, accelerating the response speed of the controller is an important topic.

- The performance of the suggested methods should be evaluated under more complicated fault scenarios, such as double-circuit lines, multiple faults, and series compensation lines.

- The stability of the controller is a prerequisite for the proper operation of the proposed method. However, the controller can lose stability in a weak grid and some complex transient processes. Therefore, the stability range should be analyzed, and a controller with robust performance should be developed.

- Offshore wind farms are also an important way to utilize wind energy. These wind farms can be integrated with the main grid by the modular multilevel converter. Therefore, for the AC tie line between wind farms and MMC, both terminals are power-electronics-based devices. At this time, flexible control methods on both sides can produce new fault behaviors, so new protection methods should be proposed.

- In future experimental work, the commercial protective relays should be connected to the RTDS system by the power amplifier. It is more effective to validate the effectiveness and protection speed of the suggested fault control methods.

LITERATURE LIST

[1] W. Cui, Y. Jiang, and B. Zhang, “Reinforcement Learning for Optimal Primary Frequency Control: A Lyapunov Approach,” *IEEE Trans. Power Syst.*, p. 1, 2022.

[2] R. H. Lasseter, “Smart Distribution: Coupled Microgrids,” *Proc. IEEE*, vol. 99, no. 6, pp. 1074–1082, 2011.

[3] J. Jia, G. Yang, and A. H. Nielsen, “A Review on Grid-Connected Converter Control for Short-Circuit Power Provision Under Grid Unbalanced Faults,” *IEEE Trans. Power Deliv.*, vol. 33, no. 2, pp. 649–661, 2018.

[4] J. Liu, Q. Tang, Y. Su, T. Li, Y. Wang, and M. Zhu, “Economic Analysis of Solid Oxide Fuel Cell and Its Role in Carbon Peak, Carbon Neutralization Process,” in *2021 4th International Conference on Energy, Electrical and Power Engineering (CEEPE)*, 2021, pp. 115–119.

[5] M. F. M. Arani and Y. A.-R. I. Mohamed, “Assessment and Enhancement of a Full-Scale PMSG-Based Wind Power Generator Performance Under Faults,” *IEEE Trans. Energy Convers.*, vol. 31, no. 2, pp. 728–739, 2016.

[6] C.-Y. Liao, W.-S. Lin, Y.-M. Chen, and C.-Y. Chou, “A PV Micro-inverter With PV Current Decoupling Strategy,” *IEEE Trans. Power Electron.*, vol. 32, no. 8, pp. 6544–6557, 2017.

[7] Y. Liang, W. Li, and Z. Lu, “Effect of Inverter-Interfaced Renewable Energy Power Plants on Negative-Sequence Directional Relays and a Solution,” *IEEE Trans. Power Deliv.*, vol. 36, no. 2, pp. 554–565, 2021.

[8] K. A. Saleh, M. S. El Moursi, and H. H. Zeineldin, “A New Protection Scheme Considering Fault Ride Through Requirements for Transmission Level Interconnected Wind Parks,” *IEEE Trans. Ind. Informatics*, vol. 11, no. 6, pp. 1324–1333, 2015.

[9] D. Shin, K.-J. Lee, J.-P. Lee, D.-W. Yoo, and H.-J. Kim, “Implementation of Fault Ride-Through Techniques of Grid-Connected Inverter for Distributed Energy Resources With Adaptive Low-Pass Notch PLL,” *IEEE Trans. Power Electron.*, vol. 30, no. 5, pp. 2859–2871, 2015.

[10] K. Ma, H. K. Høidalen, Z. Chen, and C. L. Bak, “Improved zone 1 top-line tilting scheme for the polygonal distance protection in the outgoing line,” *CSEE J. Power Energy Syst.*, pp. 1–12, 2022.

[11] C. Wang, G. Song, and J. Zhang, “A novel principle of directional relay for wind power integration based on model recognition in time-domain,” in *2016 IEEE PES Asia-Pacific Power and Energy Engineering Conference (APPEEC)*, 2016, pp. 1851–1855.

[12] Y. Fang, K. Jia, Z. Yang, Y. Li, and T. Bi, “Impact of Inverter-Interfaced Renewable Energy Generators on Distance Protection and an Improved Scheme,” *IEEE Trans.*

Ind. Electron., vol. 66, no. 9, pp. 7078–7088, 2019.

[13] V. Telukunta, J. Pradhan, A. Agrawal, M. Singh, and S. G. Srivani, "Protection challenges under bulk penetration of renewable energy resources in power systems: A review," *CSEE J. Power Energy Syst.*, vol. 3, no. 4, pp. 365–379, 2017.

[14] J. Suonan, W. Shao, G. Song, and Z. Jiao, "A Novel Single-Phase Adaptive Reclosure Scheme for Transmission Lines With Shunt Reactors," *IEEE Trans. Power Deliv.*, vol. 24, no. 2, pp. 545–551, 2009.

[15] J. Tang, G. Song, and C. Wang, "Adaptability analysis of directional relays in power systems with wind farms," in *13th International Conference on Development in Power System Protection 2016 (DPSP)*, 2016, pp. 1–6.

[16] Z. Yang, K. Jia, Z. Li, H. Zhao, Y. Fang, T. Feng, and B. Liu, "Adaptability Analysis of the Directional Relay for the System with Inverter-interfaced Renewable Energy Generators," in *2019 IEEE 8th International Conference on Advanced Power System Automation and Protection (APAP)*, 2019, pp. 1611–1616.

[17] Y. Chen, M. Wen, L. Hu, X. Qi, J. Zheng, and Z. Wang, "Fault direction identification for wind power integration system," *J. Eng.*, vol. 2019, no. 16, pp. 2520–2524, Mar. 2019.

[18] A. Hooshyar and R. Iravani, "A new directional element for microgrid protection," *IEEE Trans. Smart Grid*, vol. 9, no. 6, pp. 6862–6876, Nov. 2018.

[19] K. Jia, Z. Yang, Y. Fang, T. Bi, and M. Sumner, "Influence of Inverter-Interfaced Renewable Energy Generators on Directional Relay and an Improved Scheme," *IEEE Trans. Power Electron.*, vol. 34, no. 12, pp. 11843–11855, 2019.

[20] A. Haddadi, M. Zhao, I. Kocar, U. Karaagac, K. W. Chan, and E. Farantatos, "Impact of Inverter-Based Resources on Negative Sequence Quantities-Based Protection Elements," *IEEE Trans. Power Deliv.*, vol. 36, no. 1, pp. 289–298, 2021.

[21] A. Banaiemoqadam, A. Hooshyar, and M. A. Azzouz, "A Comprehensive Dual Current Control Scheme for Inverter-Based Resources to Enable Correct Operation of Protective Relays," *IEEE Trans. Power Deliv.*, vol. 36, no. 5, pp. 2715–2729, 2021.

[22] R. Chowdhury and N. Fischer, "Transmission Line Protection for Systems With Inverter-Based Resources – Part I: Problems," *IEEE Trans. Power Deliv.*, vol. 36, no. 4, pp. 2416–2425, 2021.

[23] D. Kang and R. Gokaraju, "A New Method for Blocking Third-Zone Distance Relays During Stable Power Swings," *IEEE Trans. Power Deliv.*, vol. 31, no. 4, pp. 1836–1843, 2016.

[24] C. Wang, G. Song, and J. Tang, "Protection performance of traditional distance relays under wind power integration," in *13th International Conference on Development in Power System Protection 2016 (DPSP)*, 2016, pp. 1–5.

[25] S. Azizi, M. Sanaye-Pasand, and M. Paolone, "A Modified Formula for Distance

Relaying of Tapped Transmission Lines With Grounded Neutrals," *IEEE Trans. Power Deliv.*, vol. 34, no. 2, pp. 690–699, 2019.

[26] A. Hooshyar, M. A. Azzouz, and E. F. El-Saadany, "Distance Protection of Lines Emanating From Full-Scale Converter-Interfaced Renewable Energy Power Plants—Part I: Problem Statement," *IEEE Trans. Power Deliv.*, vol. 30, no. 4, pp. 1770–1780, 2015.

[27] Y. Fang, K. Jia, Z. Zhu, T. Feng, Z. Yang, and B. Liu, "Adaptability analysis of distance protection on the transmission lines emanating from renewable power generators," in *2019 IEEE Innovative Smart Grid Technologies - Asia (ISGT Asia)*, 2019, pp. 275–279.

[28] Z. Yang, K. Jia, Y. Fang, Z. Zhu, B. Yang, and T. Bi, "High-Frequency Fault Component-Based Distance Protection for Large Renewable Power Plants," *IEEE Trans. Power Electron.*, vol. 35, no. 10, pp. 10352–10362, 2020.

[29] Y. Zhong, X. Kang, Z. Jiao, Z. Wang, and J. Suonan, "A Novel Distance Protection Algorithm for the Phase-Ground Fault," *IEEE Trans. Power Deliv.*, vol. 29, no. 4, pp. 1718–1725, 2014.

[30] X. Kang, S. Jiale, Z. Bo, J. Tang, and Q. Jun, "Parameter Identification Algorithm for Fault Location Based on Distributed Transmission Line Model," in *2008 IEEE Power and Energy Society General Meeting - Conversion and Delivery of Electrical Energy in the 21st Century*, 2008, pp. 1–7.

[31] S. Liu, L. L. Zhang, C. Fu, and L. Jiang, "A New Two-Port Network Model-Based Pilot Protection for AC Transmission Lines," *IEEE Trans. Power Deliv.*, vol. 35, no. 2, pp. 473–482, 2020.

[32] Z. Yang, W. Liao, H. Wang, C. L. Bak, and Z. Chen, "Improved Euclidean Distance Based Pilot Protection for Lines with Renewable Energy Sources," *IEEE Trans. Ind. Informatics*, p. 1, 2022.

[33] Y. Wang and B. Zhang, "A novel hybrid directional comparison pilot protection scheme for the LCC-VSC hybrid HVDC transmission lines," in *13th International Conference on Development in Power System Protection 2016 (DPSP)*, 2016, pp. 1–6.

[34] R. Louie and M. Etezadi-Amoli, "An analysis of a permissive overreaching transfer trip scheme at a 120kV substation," in *2008 40th North American Power Symposium*, 2008, pp. 1–6.

[35] A. Ashraf ian, M. Mirsalim, and M. A. S. Masoum, "Application of a Recursive Phasor Estimation Method for Adaptive Fault Component Based Differential Protection of Power Transformers," *IEEE Trans. Ind. Informatics*, vol. 13, no. 3, pp. 1381–1392, 2017.

[36] K. Jia, Y. Li, Y. Fang, L. Zheng, T. Bi, and Q. Yang, "Transient current similarity based protection for wind farm transmission lines," *Appl. Energy*, vol. 225, pp. 42–51,

2018.

[37] Y. Li, K. Jia, T. Bi, R. Yan, W. Li, and B. Liu, "Analysis of line current differential protection considering inverter-interfaced renewable energy power plants," in *2017 IEEE PES Innovative Smart Grid Technologies Conference Europe (ISGT-Europe)*, 2017, pp. 1–6.

[38] T. Wang, G. Song, and K. S. T. Hussain, "Three-Phase Adaptive Auto-Reclosing for Single Outgoing Line of Wind Farm Based on Active Detection From STATCOM," *IEEE Trans. Power Deliv.*, vol. 35, no. 4, pp. 1918–1927, 2020.

[39] S. H. Horowitz and A.G. Phadke, *Power system relaying*. USA: Wiley: Research Study Press, 2008.

[40] Y. M. Makwana and B. R. Bhalja, "Experimental Performance of an Islanding Detection Scheme Based on Modal Components," *IEEE Trans. Smart Grid*, vol. 10, no. 1, pp. 1025–1035, 2019.

[41] K. Jia, H. Wei, T. Bi, D. W. P. Thomas, and M. Sumner, "An Islanding Detection Method for Multi-DG Systems Based on High-Frequency Impedance Estimation," *IEEE Trans. Sustain. Energy*, vol. 8, no. 1, pp. 74–83, 2017.

[42] C. Xie and F. Li, "Online parameter determination based adaptive single-phase reclosing scheme for wind-powered outgoing lines with shunt reactors," *IET Renew. Power Gener.*, vol. 13, no. 8, pp. 1317–1328, Jun. 2019.

[43] A. Hooshyar and R. Iravani, "A New Directional Element for Microgrid Protection," *IEEE Trans. Smart Grid*, vol. 9, no. 6, pp. 6862–6876, 2018.

[44] Q. Lai, Z. Zhang, K. Xu, and X. Yin, "A New Method of Fault Direction Identification for Different Types of Renewable Energy Source Integrations," *IEEE Trans. Power Deliv.*, vol. 37, no. 4, pp. 2932–2941, 2022.

[45] A. Haddadi, I. Kocar, J. Mahseredjian, U. Karaagac, and E. Farantatos, "Negative sequence quantities-based protection under inverter-based resources Challenges and impact of the German grid code," *Electr. Power Syst. Res.*, vol. 188, p. 106573, 2020.

[46] M. A. Azzouz, A. Hooshyar, and E. F. El-Saadany, "Resilience Enhancement of Microgrids With Inverter-Interfaced DGs by Enabling Faulty Phase Selection," *IEEE Trans. Smart Grid*, vol. 9, no. 6, pp. 6578–6589, 2018.

[47] G. Suryanarayana, G. Kesava Rao, S. Sarangi, and P. Raja, "Directional relaying using parameter estimation approach," *Int. J. Electr. Power Energy Syst.*, vol. 107, pp. 597–604, 2019.

[48] X. Wang, M. Wen, J. Zheng, Y. Chen, Y. Qin, and Y. Ma, "A novel directional relay for AC lines close to the HVDC installation," *Int. J. Electr. Power Energy Syst.*, vol. 118, p. 105726, 2020.

[49] H. Jafarabadi Ashtiani, H. Samet, and T. Ghanbari, "Evaluation of directional relay algorithms in the presence of FCL," *IET Sci. Meas. Technol.*, vol. 11, no. 6, pp. 713–

722, Sep. 2017.

[50] L. Hao, D. Jiandong, L. Yang, and T. Lihao, “Ultra-high-speed transient-based directional relay for AC transmission lines connected to LCC-HVDC inverter station,” *Int. J. Electr. Power Energy Syst.*, vol. 123, p. 106235, 2020.

[51] C. Aguilera, E. Orduna, and G. Ratta, “Directional Traveling-Wave Protection Based on Slope Change Analysis,” *IEEE Trans. Power Deliv.*, vol. 22, no. 4, pp. 2025–2033, 2007.

[52] A. Hooshyar, M. A. Azzouz, and E. F. El-Saadany, “Distance Protection of Lines Emanating From Full-Scale Converter-Interfaced Renewable Energy Power Plants—Part II: Solution Description and Evaluation,” *IEEE Trans. Power Deliv.*, vol. 30, no. 4, pp. 1781–1791, 2015.

[53] P. Adhikari, S. M. Brahma, and P. H. Gadde, “Source-Agnostic Time-Domain Distance Relay,” *IEEE Trans. Power Deliv.*, p. 1, 2021.

[54] P. A. Crossley and P. G. McLaren, “Distance Protection Based on Traveling Waves,” *IEEE Power Eng. Rev.*, vol. PER-3, no. 9, pp. 30–31, 1983.

[55] R. L. d. S. França, F. C. d. S. Júnior, T. R. Honorato, J. P. G. Ribeiro, F. B. Costa, F. V Lopes, and K. Strunz, “Traveling Wave-Based Transmission Line Earth Fault Distance Protection,” *IEEE Trans. Power Deliv.*, vol. 36, no. 2, pp. 544–553, 2021.

[56] D. Pal, B. Mallikarjuna, R. J. Reddy, M. J. B. Reddy, and D. K. Mohanta, “Synchrophasor Assisted Adaptive Relaying Methodology to Prevent Zone-3 Mal-Operation During Load Encroachment,” *IEEE Sens. J.*, vol. 17, no. 23, pp. 7713–7722, 2017.

[57] Y. Q. Xia, K. K. Li, and A. K. David, “Adaptive relay setting for stand-alone digital distance protection,” *IEEE Trans. Power Deliv.*, vol. 9, no. 1, pp. 480–491, 1994.

[58] Z. Liu, H. K. Hoidalen, and M. M. Saha, “An intelligent coordinated protection and control strategy for distribution network with wind generation integration,” *CSEE J. Power Energy Syst.*, vol. 2, no. 4, pp. 23–30, 2016.

[59] A. Banaiemoqadam, A. Hooshyar, and M. A. Azzouz, “A Control-Based Solution for Distance Protection of Lines Connected to Converter-Interfaced Sources During Asymmetrical Faults,” *IEEE Trans. Power Deliv.*, vol. 35, no. 3, pp. 1455–1466, 2020.

[60] K. Ma, Z. Chen, Z. Liu, C. Leth Bak, and M. Castillo, “Protection collaborative fault control for power electronic-based power plants during unbalanced grid faults,” *Int. J. Electr. Power Energy Syst.*, vol. 130, p. 107009, 2021.

[61] K. A. Saleh and M. A. Allam, “Synthetic Harmonic Distance Relaying for Inverter-Based Islanded Microgrids,” *IEEE Open Access J. Power Energy*, vol. 8, pp. 258–267, 2021.

[62] T. G. Bolandi, H. Seyedi, S. M. Hashemi, and P. S. Nezhad, “Impedance-Differential Protection: A New Approach to Transmission-Line Pilot Protection,” *IEEE Trans.*

Power Deliv., vol. 30, no. 6, pp. 2510–2518, 2015.

[63] K. Jia, Z. Yang, Y. Fang, Z. Zhu, L. Zheng, T. Bi, and A. Hooshyar, "Amplitude comparison based pilot protection for renewable power teed line," *CSEE J. Power Energy Syst.*, pp. 1–9, 2020.

[64] W. Jin, Y. Lu, and T. Huang, "Improved Blocking Scheme for CPL Current Protection in Wind Farms Using the Amplitude Ratio and Phase Difference," *IEEE Access*, vol. 7, pp. 68060–68070, 2019.

[65] Z. Yang, W. Liao, C. L. Bak, and Z. Chen, "Comprehensive current amplitude ratio based pilot protection for line with converter-interfaced sources," *Energy Reports*, vol. 8, pp. 420–430, 2022.

[66] X. Kang, Z. Wu, J. Suonan, and H. You, "Research on pilot differential protection based on parameter identification and suitable frequency band of transmission line model," in *2011 International Conference on Advanced Power System Automation and Protection*, 2011, vol. 1, pp. 234–241.

[67] L. Zheng, K. Jia, T. Bi, Y. Fang, and Z. Yang, "Cosine Similarity Based Line Protection for Large-Scale Wind Farms," *IEEE Trans. Ind. Electron.*, vol. 68, no. 7, pp. 5990–5999, 2021.

[68] L. Zheng, K. Jia, W. Wu, Q. Liu, T. Bi, and Q. Yang, "Cosine Similarity Based Line Protection for Large Scale Wind Farms Part II—The Industrial Application," *IEEE Trans. Ind. Electron.*, vol. 69, no. 3, pp. 2599–2609, 2022.

[69] K. Jia, Z. Yang, L. Zheng, Z. Zhu, and T. Bi, "Spearman Correlation-Based Pilot Protection for Transmission Line Connected to PMSGs and DFIGs," *IEEE Trans. Ind. Informatics*, vol. 17, no. 7, pp. 4532–4544, 2021.

[70] S. Jamali and A. Ghaderi Baayeh, "Detection of secondary arc extinction for adaptive single phase auto-reclosing based on local voltage behaviour," *IET Gener. Transm. Distrib.*, vol. 11, no. 4, pp. 952–958, Mar. 2017.

[71] M. B. Djuric and V. V Terzija, "A new approach to the arcing faults detection for fast autoreclosure in transmission systems," *IEEE Trans. Power Deliv.*, vol. 10, no. 4, pp. 1793–1798, 1995.

[72] V. V Terzija and Z. M. Radojevic, "Numerical algorithm for adaptive autoreclosure and protection of medium-voltage overhead lines," *IEEE Trans. Power Deliv.*, vol. 19, no. 2, pp. 554–559, 2004.

[73] A. Parham, "New approach to adaptive single pole auto-reclosing of power transmission lines," *IET Gener. Transm. Distrib.*, vol. 4, no. 1, pp. 115-122(7), Jan. 2010.

[74] Z. M. Radojevic and J.-R. Shin, "New Digital Algorithm for Adaptive Reclosing Based on the Calculation of the Faulted Phase Voltage Total Harmonic Distortion Factor," *IEEE Trans. Power Deliv.*, vol. 22, no. 1, pp. 37–41, 2007.

[75] D. S. Fitton, R. W. Dunn, R. K. Aggarwal, A. T. Johns, and A. Bennett, “Design and implementation of an adapative single pole autoreclosure technique for transmission lines using artificial neural networks,” *IEEE Trans. Power Deliv.*, vol. 11, no. 2, pp. 748–756, 1996.

[76] F. D. Zahlay and K. S. R. Rao, “Neuro-Prony and Taguchi’s Methodology-Based Adaptive Autoreclosure Scheme for Electric Transmission Systems,” *IEEE Trans. Power Deliv.*, vol. 27, no. 2, pp. 575–582, 2012.

[77] Z. Radojevic, V. Terzija, G. Preston, S. Padmanabhan, and D. Novosel, “Smart Overhead Lines Autoreclosure Algorithm Based on Detailed Fault Analysis,” *IEEE Trans. Smart Grid*, vol. 4, no. 4, pp. 1829–1838, 2013.

[78] F. Zhalefar, M. R. D. Zadeh, and T. S. Sidhu, “A High-Speed Adaptive Single-Phase Reclosing Technique Based on Local Voltage Phasors,” *IEEE Trans. Power Deliv.*, vol. 32, no. 3, pp. 1203–1211, 2017.

[79] M. Khodadadi, M. R. Noori, and S. M. Shahrtash, “A Noncommunication Adaptive Single-Pole Autoreclosure Scheme Based on the ACUSUM Algorithm,” *IEEE Trans. Power Deliv.*, vol. 28, no. 4, pp. 2526–2533, 2013.

[80] Y. Ge, F. Sui, and Y. Xiao, “Prediction methods for preventing single-phase reclosing on permanent fault,” *IEEE Trans. Power Deliv.*, vol. 4, no. 1, pp. 114–121, 1989.

[81] M. R. D. Zadeh and R. Rubeena, “Communication-Aided High-Speed Adaptive Single-Phase Reclosing,” *IEEE Trans. Power Deliv.*, vol. 28, no. 1, pp. 499–506, 2013.

[82] D. Lin, H. Wang, D. Lin, and B. He, “An Adaptive Reclosure Scheme for Parallel Transmission Lines With Shunt Reactors,” *IEEE Trans. Power Deliv.*, vol. 30, no. 6, pp. 2581–2589, 2015.

[83] W. Zengping, L. Haofang, X. Yan, M. Jing, and L. Junling, “Prediction method for preventing reclosing on permanent fault of shunt compensated EHV/UHV transmission lines,” in *2006 IEEE Power Engineering Society General Meeting*, 2006, p. 6 pp.

[84] Y. Zhang and Q. Gong, “Single-Phase Adaptive Reclosure of EHV Transmission Lines Based on Shunt Reactor Current Identification,” in *2009 Asia-Pacific Power and Energy Engineering Conference*, 2009, pp. 1–4.

[85] X. Huang, G. Song, T. Wang, and Y. Gu, “Three-phase adaptive reclosure for transmission lines with shunt reactors using mode current oscillation frequencies,” *J. Eng.*, vol. 2018, no. 15, pp. 1012–1017, 2018.

[86] J. Suonan, Z. Liang, G. Song, and X. Kang, “Permanent faults identification for three-phase autoreclosure on transmission lines with shunt reactors,” in *2011 International Conference on Advanced Power System Automation and Protection*, 2011, vol. 1, pp. 166–172.

[87] J. L. Suonan, W. Q. Shao, and G. B. Song, “Study on Single-phase Adaptive Reclosure

Scheme Based on Parameter Identification," in *2008 Third International Conference on Electric Utility Deregulation and Restructuring and Power Technologies*, 2008, pp. 1797–1801.

[88] P. Liu, W. Shao, and G. Song, "Single-phase Adaptive Reclosure Scheme Using Impedance Property of Fault Loop in Shunt-reactored Transmission Lines," in *2019 IEEE 8th International Conference on Advanced Power System Automation and Protection (APAP)*, 2019, pp. 154–157.

[89] K. Zhu and R. Lv, "A Three-Phase Adaptive Reclosure Technology for Distribution Feeders Based on Parameter Identification," *IEEE Trans. Power Deliv.*, vol. 34, no. 6, pp. 2173–2181, 2019.

[90] Z. Yang, Q. Zhang, Z. Liu, and Z. Chen, "Fault Current Calculation for Inverter-interfaced Power Sources Considering Saturation Element," in *2021 IEEE 4th International Electrical and Energy Conference (CIEEC)*, 2021, pp. 1–5.

[91] L. Harnefors, M. Bongiorno, and S. Lundberg, "Input-Admittance Calculation and Shaping for Controlled Voltage-Source Converters," *IEEE Trans. Ind. Electron.*, vol. 54, no. 6, pp. 3323–3334, 2007.

[92] Z. Shuai, C. Shen, X. Yin, X. Liu, and Z. J. Shen, "Fault Analysis of Inverter-Interfaced Distributed Generators With Different Control Schemes," *IEEE Trans. Power Deliv.*, vol. 33, no. 3, pp. 1223–1235, 2018.

[93] Q. Zhang, D. Liu, Z. Liu, and Z. Chen, "Fault Modeling and Analysis of Grid-Connected Inverters With Decoupled Sequence Control," *IEEE Trans. Ind. Electron.*, vol. 69, no. 6, pp. 5782–5792, 2022.

[94] P. Wang, J. Song, F. Liang, F. Shi, X. Kong, G. Xie, X.-P. Zhang, and X. Gu, "Equivalent model of multi-type distributed generators under faults with fast-iterative calculation method based on improved PSO algorithm," *Prot. Control Mod. Power Syst.*, vol. 6, no. 1, p. 29, 2021.

[95] Z. Yang, Z. Liu, Q. Zhang, Z. Chen, J. d. J. Chavez, and M. Popov, "A Control Method for Converter-interfaced Sources to Improve Operation of Directional Protection Elements," *IEEE Trans. Power Deliv.*, pp. 1–11, 2022.

[96] A. Hooshyar, E. F. El-Saadany, and M. Sanaye-Pasand, "Fault Type Classification in Microgrids Including Photovoltaic DGs," *IEEE Trans. Smart Grid*, vol. 7, no. 5, pp. 2218–2229, 2016.

[97] P. Piya, M. Ebrahimi, M. Karimi-Ghartemani, and S. A. Khajehoddin, "Fault Ride-Through Capability of Voltage-Controlled Inverters," *IEEE Trans. Ind. Electron.*, vol. 65, no. 10, pp. 7933–7943, 2018.

[98] H. Guo, "Sequence-Impedance Modeling of Voltage Source Converter Interconnection Under Asymmetrical Grid Fault Conditions," *IEEE Trans. Ind. Electron.*, vol. 68, no. 2, pp. 1332–1341, 2021.

[99] Z. Yang, Q. Zhang, W. Liao, C. L. Bak, and Z. Chen, “Harmonic Injection Based Distance Protection for Line with Converter-interfaced Sources,” *IEEE Trans. Ind. Electron.*, p. 1, 2022.

[100] Z. Yang, W. Liao, Q. Zhang, C. L. Bak, and Z. Chen, “Fault Coordination Control for Converter-interfaced Sources Compatible with Distance Protection during Asymmetrical Faults,” *IEEE Trans. Ind. Electron.*, pp. 1–11, 2022.

[101] U. Karaagac, J. Mahseredjian, R. Gagnon, H. Gras, H. Saad, L. Cai, I. Kocar, A. Haddadi, E. Farantatos, S. Bu, K. W. Chan, and L. Wang, “A Generic EMT-Type Model for Wind Parks With Permanent Magnet Synchronous Generator Full Size Converter Wind Turbines,” *IEEE Power Energy Technol. Syst. J.*, vol. 6, no. 3, pp. 131–141, 2019.

[102] K. Jia, Z. Yang, Z. Zhu, Y. Fang, Q. Zhao, and B. Liu, “Current Amplitude Ratio Based Pilot Protection for the transmission Line Connected to Inverter-interfaced Renewable Energy Power Plants,” in *2019 IEEE Innovative Smart Grid Technologies - Asia (ISGT Asia)*, 2019, pp. 2090–2094.

[103] T. Shou, H. Wang, T. Zhu, L. Zhu, Q. Wang, X. Lou, J. Wang, and N. Zhou, “Harmonic current suppression for three phase PV generation system under unbalanced grid voltage,” in *2013 IEEE PES Asia-Pacific Power and Energy Engineering Conference (APPEEC)*, 2013, pp. 1–6.

[104] K. Saleh, M. A. Allam, and A. Mehrizi-Sani, “Protection of Inverter-Based Islanded Microgrids via Synthetic Harmonic Current Pattern Injection,” *IEEE Trans. Power Deliv.*, vol. 36, no. 4, pp. 2434–2445, 2021.

[105] T. Ledwaba, K. Senyane, and J. Van Coller, “Hardware-In-Loop Testing of a Differential Relay Used to Protect Single/Double Circuit Transmission Lines,” in *2019 Southern African Universities Power Engineering Conference/Robotics and Mechatronics/Pattern Recognition Association of South Africa (SAUPEC/RobMech/PRASA)*, 2019, pp. 347–352.

[106] J. Yuqi, Y. Yong, S. Xianjun, W. Shaoan, Z. Lin, and X. Ning, “On Site Test Research and Application of Flexible Short-circuit Current Suppression Technology Based on 220kV Fast Circuit Breaker,” in *2021 International Conference on Electrical Materials and Power Equipment (ICEMPE)*, 2021, pp. 1–4.

[107] Z. Yang, W. Liao, C. L. Bak, and Z. Chen, “Fault coordination control for converter-interfaced sources compatible with differential protection during asymmetrical faults,” *Energy Reports*, vol. 8, pp. 249–258, 2022.

[108] K. Deepa, P. A. Kumar, V. S. Krishna, P. N. K. Rao, A. Mounika, and D. Medhini, “A study of comparative analysis of different PWM techniques,” in *2017 International Conference On Smart Technologies For Smart Nation (SmartTechCon)*, 2017, pp. 1144–1149.

[109] S. H. Horowitz and A. G. Phadke, *Power system relaying*. USA: Wiley: Research

Study Press.

[110] X. Lil, H. Zhao, Z. Chen, and J. Hu, “A Comparison Between Fast Fourier Transform and Matrix Pencil Method for Spectral Integration Calculation,” in *2018 IEEE International Conference on Computational Electromagnetics (ICCEM)*, 2018, pp. 1–3.

[1] W. Cui, Y. Jiang, and B. Zhang, “Reinforcement Learning for Optimal Primary Frequency Control: A Lyapunov Approach,” *IEEE Trans. Power Syst.*, p. 1, 2022.

[2] R. H. Lasseter, “Smart Distribution: Coupled Microgrids,” *Proc. IEEE*, vol. 99, no. 6, pp. 1074–1082, 2011.

[3] J. Jia, G. Yang, and A. H. Nielsen, “A Review on Grid-Connected Converter Control for Short-Circuit Power Provision Under Grid Unbalanced Faults,” *IEEE Trans. Power Deliv.*, vol. 33, no. 2, pp. 649–661, 2018.

[4] J. Liu, Q. Tang, Y. Su, T. Li, Y. Wang, and M. Zhu, “Economic Analysis of Solid Oxide Fuel Cell and Its Role in Carbon Peak, Carbon Neutralization Process,” in *2021 4th International Conference on Energy, Electrical and Power Engineering (CEEPE)*, 2021, pp. 115–119.

[5] M. F. M. Arani and Y. A.-R. I. Mohamed, “Assessment and Enhancement of a Full-Scale PMSG-Based Wind Power Generator Performance Under Faults,” *IEEE Trans. Energy Convers.*, vol. 31, no. 2, pp. 728–739, 2016.

[6] C.-Y. Liao, W.-S. Lin, Y.-M. Chen, and C.-Y. Chou, “A PV Micro-inverter With PV Current Decoupling Strategy,” *IEEE Trans. Power Electron.*, vol. 32, no. 8, pp. 6544–6557, 2017.

[7] Y. Liang, W. Li, and Z. Lu, “Effect of Inverter-Interfaced Renewable Energy Power Plants on Negative-Sequence Directional Relays and a Solution,” *IEEE Trans. Power Deliv.*, vol. 36, no. 2, pp. 554–565, 2021.

[8] K. A. Saleh, M. S. El Moursi, and H. H. Zeineldin, “A New Protection Scheme Considering Fault Ride Through Requirements for Transmission Level Interconnected Wind Parks,” *IEEE Trans. Ind. Informatics*, vol. 11, no. 6, pp. 1324–1333, 2015.

[9] D. Shin, K.-J. Lee, J.-P. Lee, D.-W. Yoo, and H.-J. Kim, “Implementation of Fault Ride-Through Techniques of Grid-Connected Inverter for Distributed Energy Resources With Adaptive Low-Pass Notch PLL,” *IEEE Trans. Power Electron.*, vol. 30, no. 5, pp. 2859–2871, 2015.

[10] K. Ma, H. K. Høidalen, Z. Chen, and C. L. Bak, “Improved zone 1 top-line tilting scheme for the polygonal distance protection in the outgoing line,” *CSEE J. Power Energy Syst.*, pp. 1–12, 2022.

[11] C. Wang, G. Song, and J. Zhang, “A novel principle of directional relay for wind power integration based on model recognition in time-domain,” in *2016 IEEE PES Asia-Pacific Power and Energy Engineering Conference (APPEEC)*, 2016, pp. 1851–

1855.

[12] Y. Fang, K. Jia, Z. Yang, Y. Li, and T. Bi, “Impact of Inverter-Interfaced Renewable Energy Generators on Distance Protection and an Improved Scheme,” *IEEE Trans. Ind. Electron.*, vol. 66, no. 9, pp. 7078–7088, 2019.

[13] V. Telukunta, J. Pradhan, A. Agrawal, M. Singh, and S. G. Srivani, “Protection challenges under bulk penetration of renewable energy resources in power systems: A review,” *CSEE J. Power Energy Syst.*, vol. 3, no. 4, pp. 365–379, 2017.

[14] J. Suonan, W. Shao, G. Song, and Z. Jiao, “A Novel Single-Phase Adaptive Reclosure Scheme for Transmission Lines With Shunt Reactors,” *IEEE Trans. Power Deliv.*, vol. 24, no. 2, pp. 545–551, 2009.

[15] J. Tang, G. Song, and C. Wang, “Adaptability analysis of directional relays in power systems with wind farms,” in *13th International Conference on Development in Power System Protection 2016 (DPSP)*, 2016, pp. 1–6.

[16] Z. Yang, K. Jia, Z. Li, H. Zhao, Y. Fang, T. Feng, and B. Liu, “Adaptability Analysis of the Directional Relay for the System with Inverter-interfaced Renewable Energy Generators,” in *2019 IEEE 8th International Conference on Advanced Power System Automation and Protection (APAP)*, 2019, pp. 1611–1616.

[17] Y. Chen, M. Wen, L. Hu, X. Qi, J. Zheng, and Z. Wang, “Fault direction identification for wind power integration system,” *J. Eng.*, vol. 2019, no. 16, pp. 2520–2524, Mar. 2019.

[18] A. Hooshyar and R. Iravani, “A new directional element for microgrid protection,” *IEEE Trans. Smart Grid*, vol. 9, no. 6, pp. 6862–6876, Nov. 2018.

[19] K. Jia, Z. Yang, Y. Fang, T. Bi, and M. Sumner, “Influence of Inverter-Interfaced Renewable Energy Generators on Directional Relay and an Improved Scheme,” *IEEE Trans. Power Electron.*, vol. 34, no. 12, pp. 11843–11855, 2019.

[20] A. Haddadi, M. Zhao, I. Kocar, U. Karaagac, K. W. Chan, and E. Farantatos, “Impact of Inverter-Based Resources on Negative Sequence Quantities-Based Protection Elements,” *IEEE Trans. Power Deliv.*, vol. 36, no. 1, pp. 289–298, 2021.

[21] A. Banaiemoqadam, A. Hooshyar, and M. A. Azzouz, “A Comprehensive Dual Current Control Scheme for Inverter-Based Resources to Enable Correct Operation of Protective Relays,” *IEEE Trans. Power Deliv.*, vol. 36, no. 5, pp. 2715–2729, 2021.

[22] R. Chowdhury and N. Fischer, “Transmission Line Protection for Systems With Inverter-Based Resources – Part I: Problems,” *IEEE Trans. Power Deliv.*, vol. 36, no. 4, pp. 2416–2425, 2021.

[23] D. Kang and R. Gokaraju, “A New Method for Blocking Third-Zone Distance Relays During Stable Power Swings,” *IEEE Trans. Power Deliv.*, vol. 31, no. 4, pp. 1836–1843, 2016.

[24] C. Wang, G. Song, and J. Tang, “Protection performance of traditional distance relays

under wind power integration," in *13th International Conference on Development in Power System Protection 2016 (DPSP)*, 2016, pp. 1–5.

[25] S. Azizi, M. Sanaye-Pasand, and M. Paolone, "A Modified Formula for Distance Relaying of Tapped Transmission Lines With Grounded Neutrals," *IEEE Trans. Power Deliv.*, vol. 34, no. 2, pp. 690–699, 2019.

[26] A. Hooshyar, M. A. Azzouz, and E. F. El-Saadany, "Distance Protection of Lines Emanating From Full-Scale Converter-Interfaced Renewable Energy Power Plants—Part I: Problem Statement," *IEEE Trans. Power Deliv.*, vol. 30, no. 4, pp. 1770–1780, 2015.

[27] Y. Fang, K. Jia, Z. Zhu, T. Feng, Z. Yang, and B. Liu, "Adaptability analysis of distance protection on the transmission lines emanating from renewable power generators," in *2019 IEEE Innovative Smart Grid Technologies - Asia (ISGT Asia)*, 2019, pp. 275–279.

[28] Z. Yang, K. Jia, Y. Fang, Z. Zhu, B. Yang, and T. Bi, "High-Frequency Fault Component-Based Distance Protection for Large Renewable Power Plants," *IEEE Trans. Power Electron.*, vol. 35, no. 10, pp. 10352–10362, 2020.

[29] Y. Zhong, X. Kang, Z. Jiao, Z. Wang, and J. Suonan, "A Novel Distance Protection Algorithm for the Phase-Ground Fault," *IEEE Trans. Power Deliv.*, vol. 29, no. 4, pp. 1718–1725, 2014.

[30] X. Kang, S. Jiale, Z. Bo, J. Tang, and Q. Jun, "Parameter Identification Algorithm for Fault Location Based on Distributed Transmission Line Model," in *2008 IEEE Power and Energy Society General Meeting - Conversion and Delivery of Electrical Energy in the 21st Century*, 2008, pp. 1–7.

[31] S. Liu, L. L. Zhang, C. Fu, and L. Jiang, "A New Two-Port Network Model-Based Pilot Protection for AC Transmission Lines," *IEEE Trans. Power Deliv.*, vol. 35, no. 2, pp. 473–482, 2020.

[32] Z. Yang, W. Liao, H. Wang, C. L. Bak, and Z. Chen, "Improved Euclidean Distance Based Pilot Protection for Lines with Renewable Energy Sources," *IEEE Trans. Ind. Informatics*, p. 1, 2022.

[33] Y. Wang and B. Zhang, "A novel hybrid directional comparison pilot protection scheme for the LCC-VSC hybrid HVDC transmission lines," in *13th International Conference on Development in Power System Protection 2016 (DPSP)*, 2016, pp. 1–6.

[34] R. Louie and M. Etezadi-Amoli, "An analysis of a permissive overreaching transfer trip scheme at a 120kV substation," in *2008 40th North American Power Symposium*, 2008, pp. 1–6.

[35] A. Ashraf ian, M. Mirsalim, and M. A. S. Masoum, "Application of a Recursive Phasor Estimation Method for Adaptive Fault Component Based Differential Protection of Power Transformers," *IEEE Trans. Ind. Informatics*, vol. 13, no. 3, pp. 1381–1392,

2017.

[36] K. Jia, Y. Li, Y. Fang, L. Zheng, T. Bi, and Q. Yang, “Transient current similarity based protection for wind farm transmission lines,” *Appl. Energy*, vol. 225, pp. 42–51, 2018.

[37] Y. Li, K. Jia, T. Bi, R. Yan, W. Li, and B. Liu, “Analysis of line current differential protection considering inverter-interfaced renewable energy power plants,” in *2017 IEEE PES Innovative Smart Grid Technologies Conference Europe (ISGT-Europe)*, 2017, pp. 1–6.

[38] T. Wang, G. Song, and K. S. T. Hussain, “Three-Phase Adaptive Auto-Reclosing for Single Outgoing Line of Wind Farm Based on Active Detection From STATCOM,” *IEEE Trans. Power Deliv.*, vol. 35, no. 4, pp. 1918–1927, 2020.

[39] S. H. Horowitz and A.G. Phadke, *Power system relaying*. USA: Wiley: Research Study Press, 2008.

[40] Y. M. Makwana and B. R. Bhalja, “Experimental Performance of an Islanding Detection Scheme Based on Modal Components,” *IEEE Trans. Smart Grid*, vol. 10, no. 1, pp. 1025–1035, 2019.

[41] K. Jia, H. Wei, T. Bi, D. W. P. Thomas, and M. Sumner, “An Islanding Detection Method for Multi-DG Systems Based on High-Frequency Impedance Estimation,” *IEEE Trans. Sustain. Energy*, vol. 8, no. 1, pp. 74–83, 2017.

[42] C. Xie and F. Li, “Online parameter determination based adaptive single-phase reclosing scheme for wind-powered outgoing lines with shunt reactors,” *IET Renew. Power Gener.*, vol. 13, no. 8, pp. 1317–1328, Jun. 2019.

[43] A. Hooshyar and R. Iravani, “A New Directional Element for Microgrid Protection,” *IEEE Trans. Smart Grid*, vol. 9, no. 6, pp. 6862–6876, 2018.

[44] Q. Lai, Z. Zhang, K. Xu, and X. Yin, “A New Method of Fault Direction Identification for Different Types of Renewable Energy Source Integrations,” *IEEE Trans. Power Deliv.*, vol. 37, no. 4, pp. 2932–2941, 2022.

[45] A. Haddadi, I. Kocar, J. Mahseredjian, U. Karaagac, and E. Farantatos, “Negative sequence quantities-based protection under inverter-based resources Challenges and impact of the German grid code,” *Electr. Power Syst. Res.*, vol. 188, p. 106573, 2020.

[46] M. A. Azzouz, A. Hooshyar, and E. F. El-Saadany, “Resilience Enhancement of Microgrids With Inverter-Interfaced DGs by Enabling Faulty Phase Selection,” *IEEE Trans. Smart Grid*, vol. 9, no. 6, pp. 6578–6589, 2018.

[47] G. Suryanarayana, G. Kesava Rao, S. Sarangi, and P. Raja, “Directional relaying using parameter estimation approach,” *Int. J. Electr. Power Energy Syst.*, vol. 107, pp. 597–604, 2019.

[48] X. Wang, M. Wen, J. Zheng, Y. Chen, Y. Qin, and Y. Ma, “A novel directional relay for AC lines close to the HVDC installation,” *Int. J. Electr. Power Energy Syst.*, vol.

118, p. 105726, 2020.

[49] H. Jafarabadi Ashtiani, H. Samet, and T. Ghanbari, "Evaluation of directional relay algorithms in the presence of FCL," *IET Sci. Meas. Technol.*, vol. 11, no. 6, pp. 713–722, Sep. 2017.

[50] L. Hao, D. Jiandong, L. Yang, and T. Lihao, "Ultra-high-speed transient-based directional relay for AC transmission lines connected to LCC-HVDC inverter station," *Int. J. Electr. Power Energy Syst.*, vol. 123, p. 106235, 2020.

[51] C. Aguilera, E. Orduna, and G. Ratta, "Directional Traveling-Wave Protection Based on Slope Change Analysis," *IEEE Trans. Power Deliv.*, vol. 22, no. 4, pp. 2025–2033, 2007.

[52] A. Hooshyar, M. A. Azzouz, and E. F. El-Saadany, "Distance Protection of Lines Emanating From Full-Scale Converter-Interfaced Renewable Energy Power Plants—Part II: Solution Description and Evaluation," *IEEE Trans. Power Deliv.*, vol. 30, no. 4, pp. 1781–1791, 2015.

[53] P. Adhikari, S. M. Brahma, and P. H. Gadde, "Source-Agnostic Time-Domain Distance Relay," *IEEE Trans. Power Deliv.*, p. 1, 2021.

[54] P. A. Crossley and P. G. McLaren, "Distance Protection Based on Traveling Waves," *IEEE Power Eng. Rev.*, vol. PER-3, no. 9, pp. 30–31, 1983.

[55] R. L. d. S. França, F. C. d. S. Júnior, T. R. Honorato, J. P. G. Ribeiro, F. B. Costa, F. V Lopes, and K. Strunz, "Traveling Wave-Based Transmission Line Earth Fault Distance Protection," *IEEE Trans. Power Deliv.*, vol. 36, no. 2, pp. 544–553, 2021.

[56] D. Pal, B. Mallikarjuna, R. J. Reddy, M. J. B. Reddy, and D. K. Mohanta, "Synchrophasor Assisted Adaptive Relaying Methodology to Prevent Zone-3 Mal-Operation During Load Encroachment," *IEEE Sens. J.*, vol. 17, no. 23, pp. 7713–7722, 2017.

[57] Y. Q. Xia, K. K. Li, and A. K. David, "Adaptive relay setting for stand-alone digital distance protection," *IEEE Trans. Power Deliv.*, vol. 9, no. 1, pp. 480–491, 1994.

[58] Z. Liu, H. K. Hoidalen, and M. M. Saha, "An intelligent coordinated protection and control strategy for distribution network with wind generation integration," *CSEE J. Power Energy Syst.*, vol. 2, no. 4, pp. 23–30, 2016.

[59] A. Banaiemoqadam, A. Hooshyar, and M. A. Azzouz, "A Control-Based Solution for Distance Protection of Lines Connected to Converter-Interfaced Sources During Asymmetrical Faults," *IEEE Trans. Power Deliv.*, vol. 35, no. 3, pp. 1455–1466, 2020.

[60] K. Ma, Z. Chen, Z. Liu, C. Leth Bak, and M. Castillo, "Protection collaborative fault control for power electronic-based power plants during unbalanced grid faults," *Int. J. Electr. Power Energy Syst.*, vol. 130, p. 107009, 2021.

[61] K. A. Saleh and M. A. Allam, "Synthetic Harmonic Distance Relaying for Inverter-Based Islanded Microgrids," *IEEE Open Access J. Power Energy*, vol. 8, pp. 258–267,

2021.

[62] T. G. Bolandi, H. Seyedi, S. M. Hashemi, and P. S. Nezhad, “Impedance-Differential Protection: A New Approach to Transmission-Line Pilot Protection,” *IEEE Trans. Power Deliv.*, vol. 30, no. 6, pp. 2510–2518, 2015.

[63] K. Jia, Z. Yang, Y. Fang, Z. Zhu, L. Zheng, T. Bi, and A. Hooshyar, “Amplitude comparison based pilot protection for renewable power teed line,” *CSEE J. Power Energy Syst.*, pp. 1–9, 2020.

[64] W. Jin, Y. Lu, and T. Huang, “Improved Blocking Scheme for CPL Current Protection in Wind Farms Using the Amplitude Ratio and Phase Difference,” *IEEE Access*, vol. 7, pp. 68060–68070, 2019.

[65] Z. Yang, W. Liao, C. L. Bak, and Z. Chen, “Comprehensive current amplitude ratio based pilot protection for line with converter-interfaced sources,” *Energy Reports*, vol. 8, pp. 420–430, 2022.

[66] X. Kang, Z. Wu, J. Suonan, and H. You, “Research on pilot differential protection based on parameter identification and suitable frequency band of transmission line model,” in *2011 International Conference on Advanced Power System Automation and Protection*, 2011, vol. 1, pp. 234–241.

[67] L. Zheng, K. Jia, T. Bi, Y. Fang, and Z. Yang, “Cosine Similarity Based Line Protection for Large-Scale Wind Farms,” *IEEE Trans. Ind. Electron.*, vol. 68, no. 7, pp. 5990–5999, 2021.

[68] L. Zheng, K. Jia, W. Wu, Q. Liu, T. Bi, and Q. Yang, “Cosine Similarity Based Line Protection for Large Scale Wind Farms Part II—The Industrial Application,” *IEEE Trans. Ind. Electron.*, vol. 69, no. 3, pp. 2599–2609, 2022.

[69] K. Jia, Z. Yang, L. Zheng, Z. Zhu, and T. Bi, “Spearman Correlation-Based Pilot Protection for Transmission Line Connected to PMSGs and DFIGs,” *IEEE Trans. Ind. Informatics*, vol. 17, no. 7, pp. 4532–4544, 2021.

[70] S. Jamali and A. Ghaderi Baayeh, “Detection of secondary arc extinction for adaptive single phase auto-reclosing based on local voltage behaviour,” *IET Gener. Transm. Distrib.*, vol. 11, no. 4, pp. 952–958, Mar. 2017.

[71] M. B. Djuric and V. V Terzija, “A new approach to the arcing faults detection for fast autoreclosure in transmission systems,” *IEEE Trans. Power Deliv.*, vol. 10, no. 4, pp. 1793–1798, 1995.

[72] V. V Terzija and Z. M. Radojevic, “Numerical algorithm for adaptive autoreclosure and protection of medium-voltage overhead lines,” *IEEE Trans. Power Deliv.*, vol. 19, no. 2, pp. 554–559, 2004.

[73] A. Parham, “New approach to adaptive single pole auto-reclosing of power transmission lines,” *IET Gener. Transm. Distrib.*, vol. 4, no. 1, pp. 115-122(7), Jan. 2010.

[74] Z. M. Radojevic and J.-R. Shin, "New Digital Algorithm for Adaptive Reclosing Based on the Calculation of the Faulted Phase Voltage Total Harmonic Distortion Factor," *IEEE Trans. Power Deliv.*, vol. 22, no. 1, pp. 37–41, 2007.

[75] D. S. Fitton, R. W. Dunn, R. K. Aggarwal, A. T. Johns, and A. Bennett, "Design and implementation of an adapative single pole autoreclosure technique for transmission lines using artificial neural networks," *IEEE Trans. Power Deliv.*, vol. 11, no. 2, pp. 748–756, 1996.

[76] F. D. Zahlay and K. S. R. Rao, "Neuro-Prony and Taguchi's Methodology-Based Adaptive Autoreclosure Scheme for Electric Transmission Systems," *IEEE Trans. Power Deliv.*, vol. 27, no. 2, pp. 575–582, 2012.

[77] Z. Radojevic, V. Terzija, G. Preston, S. Padmanabhan, and D. Novosel, "Smart Overhead Lines Autoreclosure Algorithm Based on Detailed Fault Analysis," *IEEE Trans. Smart Grid*, vol. 4, no. 4, pp. 1829–1838, 2013.

[78] F. Zhalefar, M. R. D. Zadeh, and T. S. Sidhu, "A High-Speed Adaptive Single-Phase Reclosing Technique Based on Local Voltage Phasors," *IEEE Trans. Power Deliv.*, vol. 32, no. 3, pp. 1203–1211, 2017.

[79] M. Khodadadi, M. R. Noori, and S. M. Shahrtash, "A Noncommunication Adaptive Single-Pole Autoreclosure Scheme Based on the ACUSUM Algorithm," *IEEE Trans. Power Deliv.*, vol. 28, no. 4, pp. 2526–2533, 2013.

[80] Y. Ge, F. Sui, and Y. Xiao, "Prediction methods for preventing single-phase reclosing on permanent fault," *IEEE Trans. Power Deliv.*, vol. 4, no. 1, pp. 114–121, 1989.

[81] M. R. D. Zadeh and R. Rubeena, "Communication-Aided High-Speed Adaptive Single-Phase Reclosing," *IEEE Trans. Power Deliv.*, vol. 28, no. 1, pp. 499–506, 2013.

[82] D. Lin, H. Wang, D. Lin, and B. He, "An Adaptive Reclosure Scheme for Parallel Transmission Lines With Shunt Reactors," *IEEE Trans. Power Deliv.*, vol. 30, no. 6, pp. 2581–2589, 2015.

[83] W. Zengping, L. Haofang, X. Yan, M. Jing, and L. Junling, "Prediction method for preventing reclosing on permanent fault of shunt compensated EHV/UHV transmission lines," in *2006 IEEE Power Engineering Society General Meeting*, 2006, p. 6 pp.

[84] Y. Zhang and Q. Gong, "Single-Phase Adaptive Reclosure of EHV Transmission Lines Based on Shunt Reactor Current Identification," in *2009 Asia-Pacific Power and Energy Engineering Conference*, 2009, pp. 1–4.

[85] X. Huang, G. Song, T. Wang, and Y. Gu, "Three-phase adaptive reclosure for transmission lines with shunt reactors using mode current oscillation frequencies," *J. Eng.*, vol. 2018, no. 15, pp. 1012–1017, 2018.

[86] J. Suonan, Z. Liang, G. Song, and X. Kang, "Permanent faults identification for three-phase autoreclosure on transmission lines with shunt reactors," in *2011 International*

Conference on Advanced Power System Automation and Protection, 2011, vol. 1, pp. 166–172.

[87] J. L. Suonan, W. Q. Shao, and G. B. Song, "Study on Single-phase Adaptive Reclosure Scheme Based on Parameter Identification," in *2008 Third International Conference on Electric Utility Deregulation and Restructuring and Power Technologies*, 2008, pp. 1797–1801.

[88] P. Liu, W. Shao, and G. Song, "Single-phase Adaptive Reclosure Scheme Using Impedance Property of Fault Loop in Shunt-reactored Transmission Lines," in *2019 IEEE 8th International Conference on Advanced Power System Automation and Protection (APAP)*, 2019, pp. 154–157.

[89] K. Zhu and R. Lv, "A Three-Phase Adaptive Reclosure Technology for Distribution Feeders Based on Parameter Identification," *IEEE Trans. Power Deliv.*, vol. 34, no. 6, pp. 2173–2181, 2019.

[90] Z. Yang, Q. Zhang, Z. Liu, and Z. Chen, "Fault Current Calculation for Inverter-interfaced Power Sources Considering Saturation Element," in *2021 IEEE 4th International Electrical and Energy Conference (CIEEC)*, 2021, pp. 1–5.

[91] L. Harnefors, M. Bongiorno, and S. Lundberg, "Input-Admittance Calculation and Shaping for Controlled Voltage-Source Converters," *IEEE Trans. Ind. Electron.*, vol. 54, no. 6, pp. 3323–3334, 2007.

[92] Z. Shuai, C. Shen, X. Yin, X. Liu, and Z. J. Shen, "Fault Analysis of Inverter-Interfaced Distributed Generators With Different Control Schemes," *IEEE Trans. Power Deliv.*, vol. 33, no. 3, pp. 1223–1235, 2018.

[93] Q. Zhang, D. Liu, Z. Liu, and Z. Chen, "Fault Modeling and Analysis of Grid-Connected Inverters With Decoupled Sequence Control," *IEEE Trans. Ind. Electron.*, vol. 69, no. 6, pp. 5782–5792, 2022.

[94] P. Wang, J. Song, F. Liang, F. Shi, X. Kong, G. Xie, X.-P. Zhang, and X. Gu, "Equivalent model of multi-type distributed generators under faults with fast-iterative calculation method based on improved PSO algorithm," *Prot. Control Mod. Power Syst.*, vol. 6, no. 1, p. 29, 2021.

[95] Z. Yang, Z. Liu, Q. Zhang, Z. Chen, J. d. J. Chavez, and M. Popov, "A Control Method for Converter-interfaced Sources to Improve Operation of Directional Protection Elements," *IEEE Trans. Power Deliv.*, pp. 1–11, 2022.

[96] A. Hooshyar, E. F. El-Saadany, and M. Sanaye-Pasand, "Fault Type Classification in Microgrids Including Photovoltaic DGs," *IEEE Trans. Smart Grid*, vol. 7, no. 5, pp. 2218–2229, 2016.

[97] P. Piya, M. Ebrahimi, M. Karimi-Ghartemani, and S. A. Khajehoddin, "Fault Ride-Through Capability of Voltage-Controlled Inverters," *IEEE Trans. Ind. Electron.*, vol. 65, no. 10, pp. 7933–7943, 2018.

[98] H. Guo, "Sequence-Impedance Modeling of Voltage Source Converter Interconnection Under Asymmetrical Grid Fault Conditions," *IEEE Trans. Ind. Electron.*, vol. 68, no. 2, pp. 1332–1341, 2021.

[99] Z. Yang, Q. Zhang, W. Liao, C. L. Bak, and Z. Chen, "Harmonic Injection Based Distance Protection for Line with Converter-interfaced Sources," *IEEE Trans. Ind. Electron.*, p. 1, 2022.

[100] Z. Yang, W. Liao, Q. Zhang, C. L. Bak, and Z. Chen, "Fault Coordination Control for Converter-interfaced Sources Compatible with Distance Protection during Asymmetrical Faults," *IEEE Trans. Ind. Electron.*, pp. 1–11, 2022.

[101] U. Karaagac, J. Mahseredjian, R. Gagnon, H. Gras, H. Saad, L. Cai, I. Kocar, A. Haddadi, E. Farantatos, S. Bu, K. W. Chan, and L. Wang, "A Generic EMT-Type Model for Wind Parks With Permanent Magnet Synchronous Generator Full Size Converter Wind Turbines," *IEEE Power Energy Technol. Syst. J.*, vol. 6, no. 3, pp. 131–141, 2019.

[102] K. Jia, Z. Yang, Z. Zhu, Y. Fang, Q. Zhao, and B. Liu, "Current Amplitude Ratio Based Pilot Protection for the transmission Line Connected to Inverter-interfaced Renewable Energy Power Plants," in *2019 IEEE Innovative Smart Grid Technologies - Asia (ISGT Asia)*, 2019, pp. 2090–2094.

[103] T. Shou, H. Wang, T. Zhu, L. Zhu, Q. Wang, X. Lou, J. Wang, and N. Zhou, "Harmonic current suppression for three phase PV generation system under unbalanced grid voltage," in *2013 IEEE PES Asia-Pacific Power and Energy Engineering Conference (APPEEC)*, 2013, pp. 1–6.

[104] K. Saleh, M. A. Allam, and A. Mehrizi-Sani, "Protection of Inverter-Based Islanded Microgrids via Synthetic Harmonic Current Pattern Injection," *IEEE Trans. Power Deliv.*, vol. 36, no. 4, pp. 2434–2445, 2021.

[105] T. Ledwaba, K. Senyane, and J. Van Coller, "Hardware-In-Loop Testing of a Differential Relay Used to Protect Single/Double Circuit Transmission Lines," in *2019 Southern African Universities Power Engineering Conference/Robotics and Mechatronics/Pattern Recognition Association of South Africa (SAUPEC/RobMech/PRASA)*, 2019, pp. 347–352.

[106] J. Yuqi, Y. Yong, S. Xianjun, W. Shaoan, Z. Lin, and X. Ning, "On Site Test Research and Application of Flexible Short-circuit Current Suppression Technology Based on 220kV Fast Circuit Breaker," in *2021 International Conference on Electrical Materials and Power Equipment (ICEMPE)*, 2021, pp. 1–4.

[107] Z. Yang, W. Liao, C. L. Bak, and Z. Chen, "Fault coordination control for converter-interfaced sources compatible with differential protection during asymmetrical faults," *Energy Reports*, vol. 8, pp. 249–258, 2022.

[108] K. Deepa, P. A. Kumar, V. S. Krishna, P. N. K. Rao, A. Mounika, and D. Medhini, "A study of comparative analysis of different PWM techniques," in *2017 International*

Conference On Smart Technologies For Smart Nation (SmartTechCon), 2017, pp. 1144–1149.

[109] S. H. Horowitz and A. G. Phadke, *Power system relaying*. USA: Wiley: Research Study Press.

[110] X. Lil, H. Zhao, Z. Chen, and J. Hu, "A Comparison Between Fast Fourier Transform and Matrix Pencil Method for Spectral Integration Calculation," in *2018 IEEE International Conference on Computational Electromagnetics (ICCEM)*, 2018, pp. 1–3.

ISSN (online): 2446-1636
ISBN (online): 978-87-7573-721-5

AALBORG UNIVERSITY PRESS